Impact of Pollutant Ozone on the Biophysical Properties of Tear Film Lipid Layer Model Membranes

Mahshid Keramatnejad

A Thesis

in

The Department

of

Chemistry and Biochemistry

Presented in Partial Fulfillment of the Requirements

for the Degree of Master Science (Chemistry) at

Concordia University

Montréal, Québec, Canada

August 2022

CONCORDIA UNIVERSITY

School of Graduate Studies

This is to certify that the thesis prepared

By: Mahshid Keramatnejad

Entitled: Impact of Pollutant Ozone on the Biophysical Properties of Tear Film

Lipid Layer Model Membranes

and submitted in partial fulfillment of the requirements for the degree of

Master of Science (Chemistry)

complies with the regulations of the University and meets the accepted standards with respect to originality and quality.

Signed by the final examining committee:

_____ Chair

Dr. Xavier Ottenwaelder

_____ Examiner

Dr. Yves Gélinas

_____ Examiner

Dr. Dajana Vuckovic

_____ Supervisor

Dr. Christine DeWolf

Approved by   _____

Dr. Paul Joyce Chair of Department or Graduate Program Director

_____ 2022   _____

Dr. Pascale Sicotte Dean of Faculty of Arts and Science

ABSTRACT

Impact of Pollutant Ozone on the Biophysical Properties of Tear Film Lipid Layer Model Membranes

Mahshid Keramatnejad

The human tear film lipid layer (TFLL) is a duplex lipid layer film comprising the outermost layer of the tear film, responsible for surface tension reduction of the tear film in the blinking function. Exposure of the tear film lipid layer to increased ground-level concentrations of air pollutants, for example tropospheric ozone, can impact the chemical composition, structure and the function of the tear film lipid layer by impacting its surface activity, stability, respreadability and viscoelasticity, important TFLL characteristics in the blinking function. This compromise in these characteristics, leads to the emergence of dry eye disease (DED). In this research, Langmuir films spread at the air-water interface are used as TFLL mimicking model membranes. In addition to the study of the functional role of each component in the TFLL, the impact of ozone exposure on their biophysical properties is also investigated using Langmuir balance, Brewster angle microscopy, a profile analysis tensiometer, and mass spectrometry. Moreover, the crystallinity, lateral ordering, and vertical structure of the cholesteryl oleate film, as an important cholesteryl ester used in TFLL model membrane studies is investigated using Grazing Incidence X-Ray Diffraction (GIXD), X-ray reflectivity (XR) and Grazing Incidence Off-Specular Scattering (GIXOS), respectively. Crystallinity of the cholesteryl oleate film was attributed to the cholesterol ring packing and a flat, monolayer film was observed at lower surface pressures. Oxidation impacts the phase transition behaviour of the model membranes as well as their multilayer formation. It also leads to expansion of the films to higher molecular areas, fluidization of the films, significant morphological changes, reduction of their respreadability and a composition-driven impact on their viscoelasticity. These findings can help better understand the roles of TFLL components in its function as well as the impact of prolonged ozone exposure on the mechanical and biophysical properties of human TFLL.

ACKNOWLEDGEMENTS

First, I would like to thank my supervisor Dr. Christine DeWolf for introducing me to this challenging and interesting project that went hand in hand with my passion. I am very grateful to her for always being available to discuss my results, doubts, and progress. More than anything, I would like to thank her for creating a positive lab environment and lastly, all her support and guidance throughout my M.Sc.

I thank the members of my committee Dr. Yves Gélinas and Dr. Dajana Vuckovic for their wisdom and guidance throughout my work.

Additionally, I would like to thank all the professors at the department of Chemistry and Biochemistry, for the highly enlightening and diverse graduate courses I took during my M.Sc. which contributed a great deal to making this an exceptional learning experience, Dr. Dajana Vuckovic, Dr. Cameron Skinner, Dr. Gregor Kos, Dr. Xavier Ottenwaelder and Dr. Gilles Peslherbe. Thanks also, to Dr. Cerrie Rogers, Dr. Jennifer Romero and Kai Lee for a rewarding teaching assistantship experience. Thanks to Dr. Heng Jiang in the CBAMS center for his guidance and to all the staff and students at the Department of Chemistry and Biochemistry who helped create a positive and friendly environment.

Thanks to my amazing labmates, Dr. Renaud Miclette Lamarche, Dr. Hala Youssef for their support and help during my experimental and data analysis training, thanks to Janet Gaba for my computational training, Dalia Ali, Javier Porro Suardiaz, Kailen Kroeger, Zahra Alinia and Patricia Taktikakis and all past and current undergraduate students at Dr. DeWolf's research group for a memorable and rewarding M.Sc. experience.

I would especially like to thank my wonderful husband, Sohrab for his constant support and positivity, my hardworking parents, Maryam and Parviz for fighting to give us a quality education and my amazing brother, Dr. Kamran Keramatnejad for his constant love and understanding and all my friends all over the world whose support I relied on throughout this journey.

This would not have been possible without any of you.

Mahshid

Contribution of Authors

All manuscripts and experiments have been carried out and written by Mahshid Keramatnejad under the supervision of Dr. Christine DeWolf.

Table of Contents

Abbreviations

AFM: Atomic Force Microscopy

APS: Advanced Photon Source

ASDA: Axisymmetric Drop Shape Analysis

BA: Behenyl alcohol

BO: Behenyl oleate

BAM: Brewster Angle Microscopy

CE: Cholesteryl ester

CE-13:   Cholesteryl tridecanoate

CE-16:   Cholesteryl palmitate

CE-18:   Cholesteryl stearate

CFSS: Corneal fluorescein staining score

CN: Cholesteryl nervonate

CO: Cholesteryl oleate

DED: Dry Eye Disease

DPOG: 1,3-dipalmitoyl-2-oleoylglycerol

DPPC: Dipalmitoylphosphotidylcholine

Egg PC: L-α-phosphatidylcholine

ESI: Electrospray ionization

FFA: Free fatty acids

FWHM: Full width at half maximum

GIXD: Grazing Incidence X-Ray Diffraction

GIXOS: Grazing Incidence Off-Specular Scattering

GT: Glyceryl trioleate

HHP: Hydroxyhydroperoxides

KNHANES: Korea National Health and Nutrition Examination Survey

MGD: Meibomian Gland Dysfunction

MGS: Meibomian Gland Secretions

MS: Mass Spectrometry

NO: Nitric oxide

NO_2: Nitrogen dioxide

NO_x: Nitrogen oxides

OAHFA: (O-Acyl)-ω-hydroxy fatty acids

OEA: Oleic acid ethyl ester

OH: Hydroxyl radical

HO_2: Hydroperoxyl radicals

OSDI: Ocular surface discomfort index

PA: Palmitic acid

PAT: Profile Analysis Tensiometer

PBS: Phosphate-buffered saline

PE: Phosphatidylethanolamines

PM_{10}:   Particulate matter (diameter of 10 μm or less)

$PM_{2.5}$:   Particulate matter (diameter of 2.5 μm or less)

POPC: Palmitoyl-oleoyl-phosphatidylcholine

POPG: 1-palmitoyl-2-oleyl-phosphotidylglycerol

Q_{xy}:   In-plane diffraction peaks

Q_z: Out-of-plane diffraction peaks

R_F: Fresnel reflectivity

SA: Stearic acid

SM: Sphingomyelin

STR: Step Through Program

TBUT: Tear Film Break-Up Time

TFLL: Tear Film Lipid Layer

TFOS DEWS II: Tear Film & Ocular Surface Society Dry Eye Workshop II

USA: United States of America

UV: Ultraviolet

VOC: Volatile Organic Compounds

WE: Wax ester

XR: X-Ray Reflectivity

List of figures

List of tables

List of equations

Chapter 1. Introduction & Literature Review

1.1. Tear Film Lipid Layer Composition, Structure & Function

The human tear film covering the surface of the cornea can be divided into three separate layers [1–3]. Firstly is a mucin layer directly at the surface of the cornea, composed of sugar-rich glycosylated proteins that have been suggested to assist in the lubrication of the eye surface in blinking [1]. The second layer, the aqueous layer, is the thickest layer of the tear film [1,4] and consists of a solution of electrolytes, proteins, peptides as well as metabolites [1,5]. This fluid is secreted continuously by the lacrimal glands [1]. The outermost layer of the tear film which is predominantly composed of lipids is the tear film lipid layer (TFLL) [1].

The human tear film lipid layer (TFLL) is an important interface in the body that covers the aqueous tear film, creating the eye-air interface. This important barrier plays a number of crucial roles, namely, the reduction of the surface tension due to its unique surface properties [1,6], aiding in the respreading of the tear film after each blink and maintaining the overall tear film stability at the air-tear interface [1,7,8], resistance to water evaporation, though this function of TFLL has been subject of debate in recent years [1,7–11], providing a smooth refractive surface [1,9,11] and providing defense against microbial infections [8] as well as a environmental agents [12,13]. The thickness of the TFLL has been estimated to be about 15-160 nm, most probably close to 30 nm and 5 to 20 molecules thick [1,12,14,15]. TFLL is considered to have a multilayered structure at the air-tear interface [16–18].

Meibomian gland secretions (MGS) are the main constituents of the TFLL, secreted by the meibomian glands situated within the eyelids [8,19] Therefore, they are the most researched in studies interested in understanding the composition, structure, and function of TFLL[8]. The exact composition of TFLL is still a major subject of debate in the literature due to the many limitations that exist in working with extracted meibum lipids, not the least of which are the use of various different sample collection techniques, i.e., glass microcapillary tube, Dacron swab, spatula or cytology microbrush, which lead to disparities between results of different research labs due to inter- and intra- individual biological variabilities [20], the typically small amounts of lipids collected from sample donors, lack of chemical standards, the samples being easily contaminated, the sheer number of lipid families to be analyzed within each sample and the need

to analyze them with different techniques. The difference in non-human meibum in comparison with human meibum [21] as well as occasional reports of contaminations throughout the analyses, leading to wrong assumptions on the composition of meibum [8,11,19,22–27] have also been cause for these disparities. Thus, it is difficult to report the exact composition and molar percentage of each lipid family in the TFLL, and different reports can be found.

However, it has been mostly found in such studies that the composition of human TFLL which for the most part is quite well represented by MGS, is composed of > 90% non-polar lipids [1,8,11,28]. 30-45 mol% of the human meibum is comprised of long acyl chain cholesteryl esters (CEs) (C22:1-C34:1) and 30-50 mol% are wax esters, with mostly C18:1 fatty acid chains with C18-C30 alcohols chains [1,8,11,19,22,28,29]. Furthermore, 2 to 4 mol% of human meibum is comprised of triglycerides [8,11,28,30], 2.5 mol% or less of free fatty acids [3,28,31,32], 0.5-5.6 mol% of free cholesterol [3,8,11,28,30–32], 2 mol% of diesters [3,28,31,32] and 3-7 mol% of hydrocarbons [3,28,31,32].

As for the polar lipids of TFLL, there are two classes of lipids that are reportedly constituents of the polar part of TFLL and as they are different in their origins, their exact roles in TFLL remain to be a point of controversy in the literature [1,7,8,11,25,33]. These two classes of lipids are (O-Acyl)-ω-hydroxy fatty acids (OAHFA) which are reported to make up 3-5 mol% of TFLL [19,25,33] and are MGS endogenous, as well as ~13 mol% phospholipids [1,8,34] which are of non-MGS origin, found generally in whole tear extracts and are composed of phosphatidylcholines (PCs > 60%), phosphatidylethanolamines (PEs, ~15%), ceramides and sphingomyelins (SM) (< 5%) [1,8,34]. It is important to note that TFLL also has some proteins in its composition as well. Non-lipid components such as proteins, salt and polysaccharides have been found in MGS [1,8,35–38]. It is suggested that these proteins may impact TFLL characteristics by intercalating between the lipid molecules of TFLL [1,8,38–40].

Despite the controversies in the exact key components of the of the polar lipids of TFLL, they are considered to be quite crucial in the TFLL functions. The most widely accepted view of the structure of TFLL assumes a multilayered structure, wherein at the interface of aqueous tear film and TFLL, there is a sub-layer the amphiphilic polar lipids of TFLL, on top of which a bulky layer comprised predominantly of non-polar highly hydrophobic lipids reside which create the eye-air interface [1,3,8,41]. As the non-polar hydrophobic lipids do not readily interact and spread on

top of the underlying aqueous layer, this sub-layer of polar amphiphilic lipids, able to interact with both layers, is crucial in stabilizing the TFLL as well as the aqueous tear film underneath [1,3,7,8,24,34].

This multilayered structure has been confirmed previously using grazing incidence X-ray diffraction (GIXD) in studying both tear lipid extracts as well as mixed films of lipids or model membranes [1,42]. Moreover, Georgiev et al. 2017, [8] used data from previous work [19,43–48] to calculate the area per MGS molecule (59 $Å^2$-9.7 $Å^2$) which implies that during the compression of the meibum film, it can reach areas corresponding with multilayering. One of the notable biophysical characteristics observed from meibum extract films in studies using a Langmuir balance is the formation of compressible films that do not display collapse. This is quite relevant to the impact of the stability of TFLL while blinking and after multiple blinks. These two important characteristics have been attributed to either the formation of multilayers or reversible folding [1,49].

1.2. Tear Film Lipid Layer Model Membrane Studies

A number of studies have been dedicated to the study of TFLL model membrane films. Due to the discrepancies in the literature as to the exact composition of TFLL, as well as the complicated and multicomponent nature of physiological TFLL and the apparent difficulty in creating a physiologically relevant model from scratch, model membrane studies of TFLL have been challenging and rife with inconsistencies, comprising a wide range of both experimental and simulation-based surface characterization techniques, perspectives and components.

In 1974, Holly reported using a partially oxidized indicator oil prepared from a petroleum lubricating oil to represent the TFLL which easily formed a duplex film while being compressed using a Langmuir balance [50,51]. Several studies have used multicomponent mixtures of representative TFLL lipid families in order to study the effect of composition on the structure and function of TFLL. These studies have used a wide variety of lipids and more importantly proportions that generally differ from the physiological non-polar to polar ratio. One example of this is a study by Petrov et al. 2007, where a two-dimensional order was reported for using an 8-component synthetic film, with oleic acid ethyl ester (OEA) being the major component (70.2%) [42].

3

Experimental surface characterization techniques were used in conjunction with simulation models in two studies by Kulovesi et al. 2010 and 2012, respectively. In one study, they used an artificial TFLL composed of egg phosphatidylcholine (egg PC) as the polar lipid component, cholesteryl oleate (CO) as cholesteryl ester and a triglyceride mixture with PC comprising 60% of the film [17] which differs from the reported proportions of polar lipids in physiological TFLL, represented by MGS, being > 90% non-polar lipids [1,8,11,28]. In another study and using similar experimental techniques and with a focus on the impact of composition on the stability of the tear film, several model membranes were investigated with varying proportions of egg PC, CO, egg phosphatidylethanolamine (PE), a mixture of various triglycerides as well as a free fatty acid mixture (FFAs) made from 50: 50 stearic acid (SA): palmitic acid (PA) [16]. Aimed at understanding the impact of composition on the organization, stability and the dynamics of the TFLL, these two studies have provided valuable information on the topic such as the importance of the polar lipids in the stability of the TFLL and they used both experimental and simulation techniques [16,17]. However, the polar lipid proportion in these mixtures were higher than reported in MGS, ranging form 60% to 90% compared with the 4% to 13% reported in physiological MGS [1,8,11,28].

TFLL model membranes with more physiologically relevant proportions were used in TFLL model membranes studied by Rantamäki et al. 2012 and Kulovesi et al. 2014, using egg PC, CO, wax ester behenyl oleate (WE) and behenyl alcohol (BA) and egg PC, CO, GT and a wax ester mixture, respectively [52,53]. These studies were mainly focused on the evaporation retardation role of TFLL and the impact of wax esters. Both reported that wax ester films alone are in fact capable of evaporation retardation, but the evidence of such an impact was lacking in mixed films of wax esters and other lipids [52,53]. A model using the same lipids (excluding the wax esters and wax alcohol) was used recently by Xu et al. 2022, wherein an OAHFA was used as well as PC for the polar lipid components and a predominant impact of PC was reported on the surface activity of the recombinant film [54].

Millar et al. 2012, used films of cholesteryl esters (namely cholesteryl nervonate (CN), and cholesteryl palmitate (CP)) along with extracted meibomian lipid films and their mixtures to study their structure where a duplex film containing liquid crystals was reported [55]. An investigation on the effect of ectoine on the phase behaviour of TFLL model membranes by

4

Dwivedi et al. 2014, used binary and ternary films composed of 1,2-dipalmitoyl-sn-glycero-3-phosphocholine (DPPC), cholesteryl-3-palmitate (CP) and 1,3-dipalmitoyl-2-oleoylglycerol (DPOG) where, similar to previous work, the polar lipids comprise a large proportion of the model membranes [56] contrary to their MGS proportions [1,8,11,28].

In simulation studies of TFLL model membranes, palmitoyl-oleoyl-phosphatidylcholine (POPC) was used as the polar lipid along with CO, GT and free fatty acids where the neutral TFLL lipids was reported to increase the stability of TFLL [57,58]. Patterson et al. 2016 and 2017, focused on the polar TFLL model membranes using strictly phospholipids, reporting the possible role of the polar TFLL on the stability of the tear film upon blinking [59,60].

Recently, a minimalistic approach has been chosen for model membrane studies aiming at simplifying the study of the composition, structure and function relationship of TFLL where two component mixtures of non-polar and polar lipids were used [12,61]. For example, binary mixtures of POPC and GT were used by Olyńskaż et al. 2020, [12] and mixtures of (O-oleyl)-ω-hydroxy arachidic acid (20-OAHFA) and cholesteryl nervonate (CN) were used by Paananen et al [61] 2020, both studies providing valuable information on the multilayer formation behaviour of TFLL model membranes. While various models have been used to study holistically one or more functions of TFLL, relatively less attention has been paid to the contributions of individual lipid classes to these functions.

1.3. Dry Eye Disease (DED)

This review will focus on the definition, epidemiology of dry eye disease (DED) as well as correlations of DED in the literature with respect to the TFLL composition, structure, and function relationship.

1.3.1. The Definition and Classification of Dry Eye Disease

According to the Tear Film & Ocular Surface Society (TFOS), Dry Eye Workshop II (TFOS DEWS II), the updated and internationally accepted definition of DED is as follows:

"Dry eye is a multifactorial disease of the ocular surface characterized by a loss of homeostasis of the tear film, and accompanied by ocular symptoms, in which tear film instability and

hyperosmolarity, ocular surface inflammation and damage, and neurosensory abnormalities play etiological roles." [62]

There are two main categories of DED that are not mutually exclusive: aqueous deficient dry eye and evaporative dry eye. Evidence has shown that a larger number of DED cases are in fact evaporative dry eye rather than aqueous deficient dry eye, or they are mixed [62]. As was described previously, the fluid of the aqueous part of the tear film is secreted by the lacrimal glands, thus aqueous deficient dry eye is related to any conditions that affect the lacrimal glands [62]. As for the major number of DED cases which are caused by evaporative dry eye, it describes conditions affecting the lids or the ocular surface. Prominent among the lid-related problems is meibomian gland dysfunction (MGD) which has been reported in 86% of DED cases with only a small percentage of the cases displaying symptoms of aqueous deficient dry eye [62,63].

1.3.2. The Epidemiology & Risk Factors of Dry Eye Disease

DED is the predominant ophthalmic related disease of the modern age and a growing ocular health concern [8,62], impacting the quality of life in 10%-30% of the global population [64]. DED is characterized with an unstable tear film, hyperosmolarity and ocular inflammation [8,62]. In severe cases, DED is associated with chronic eye pain, visual disturbances, poor quality of day to day life and depression [8,62].

DED is characterized by a number of consistent risk factors associated with DED, prominent among which are MGD [8,65], age [64,66–68], race [62], sex [62,64,66,68,69], connective tissue disease [62], long term use of computer screens [8,62], environmental conditions most importantly pollution [64,68,70–72] and low humidity [64,70] and the use of certain medications such as antihistamines [62,66] and antidepressants [62]. The prevalence of DED has been reported to be 21.3% in Canada, corresponding to ~6.3 million people [73], 7% in US women and 4% in US men [64,69], 7.4% in Australia [64,74], 27.5% in Indonesia [64,75], 33.7% in elderly Taiwan population [64,67] and 33% in Japan [64,76]. The cost of DED in terms of treatment and negative impact on work productivity and income in USA alone has been calculated to be $55.4 billion [8,77] with similar global reports [8,78].

1.3.3. Dry Eye Disease Correlation with a Compromised TFLL Composition, Structure & Function

As mentioned before, MGD, which is associated with changes in the secreted lipids of meibomian glands both in quality as well as quantity, is observed in most of the DED cases [79,80]. It is still uncertain the extent to which compositional changes to MGS negatively impact the lipid structure as well as surface characteristics of lipids of TFLL; however, increased protein content [8,36,37,81] and decrease in polar lipid content [26,27,82] have been previously as potential contributors.

As for the impact on structural properties, Georgiev et al. 2014, showed that there are significant morphological differences between MGS of healthy subjects and patients with MGD [8,48], wherein a continuous and thick film was observed in healthy subjects and a patchy and discontinuous with thinner areas was observed in MGD patients [8,48]. The continuous and thick film in healthy subjects has been associated with a tear film non- invasive break up time of > 15 s implicating high stability for the film, whereas a non- invasive break up time of <5 s in MGD patients, indicates reduced stability [8,83–86]. It has also been shown in the case of MGD that the important spreading characteristic of the TFLL may be impacted [87–89].

It has been reported that delipidation of the tears results in a higher surface tension 53~55.5 mNm^{-1}, compared with the surface tension of the tears of healthy subjects (43.6 ± 2.7 mNm^{-1}) [6,8,90] and is quite close to values measured from samples of DED patients (49.6 ± 2.2 mNm^{-1}) [8,91]. Moreover, Georgiev reported that healthy MGS films predominantly display elastic behaviour, while films formed by meibum secretions collected from MGD patients, show higher viscosity, implying that the film shows less resistance to deformations [48]. To add to the evidence that there is significant correlation between the compromised composition, structure and function of TFLL and DED emergence, recently similar results were observed wherein mutations in genes related to the synthesis of meibomian lipids, led to a compromised TFLL composition and eventually acute DED [92–94].

1.4. Tropospheric Ozone & DED

This review will focus on processes involved in the production of tropospheric ozone, its impact on the unsaturated acyl chains of TFLL components as well as the correlation of tropospheric ozone with the prevalence of DED in the populations recently highlighted in the literature.

1.4.1. Tropospheric Ozone

While the scientific community believed for a long time (until 1970s) that the source of tropospheric ozone was stratosphere and that it was chemically inert, extensive scientific evidence has shown that this is not case [95–98]. The production of tropospheric ozone is mainly due to the existence of NO and hydrocarbons in the troposphere. Some examples of the origin of NO_x and hydrocarbons in the troposphere are fossil fuel burning, biomass burning, vegetation and landfills [98]. A simplified schematic of the series of reactions leading to the production of tropospheric ozone is provided in Figure 1.1 [96]. As observed, initially, hydroxyl radicals react with hydrocarbons, producing carbon dioxide, water and more importantly hydroperoxyl radicals (HO_2) which in turn react with NO forming NO_2 and even more hydroxyl radicals. Then, the photolysis of NO_2 leads to the production of ground-state oxygen atoms O (^{3}P) which in turn, react with oxygen to form tropospheric ozone [95–98]. There is also a less notable source of tropospheric ozone which is via the stratosphere-troposphere ozone exchange [99].

OH radicals are paramount in the chemical composition of the atmosphere, since many of the gases in the atmosphere, whether from natural or anthropogenic origins, have resident times that are greatly impacted by their reactivity with OH radicals [97,98]. Thus, looking at this reaction pathway, it is important to note that tropospheric ozone also plays an important role in producing OH radicals through absorbing UV radiation [98]. The surface concentrations of ozone have increased significantly due to anthropogenic activities from 10 to 15 ppb in the pre-industrial era to 30 to 40 ppb now [97,100]. Ozone concentration as high as 300 ppb is reported in highly polluted areas and environmental smog [101] . This increase can be directly linked to the increase in fossil fuel and biomass burning, leading to an increase in surface levels of NO_x radicals [95,97,100]. Moreover, it is noteworthy that ozone is a greenhouse gas as it is an infrared absorber, as well as being capable of absorbing UV emissions in the wavelength of 290 nm to 320 nm (potentially harmful to Terran life), so the increase in its average ground-levels has implications for climate change as well as our UV exposure levels [97,98,102].
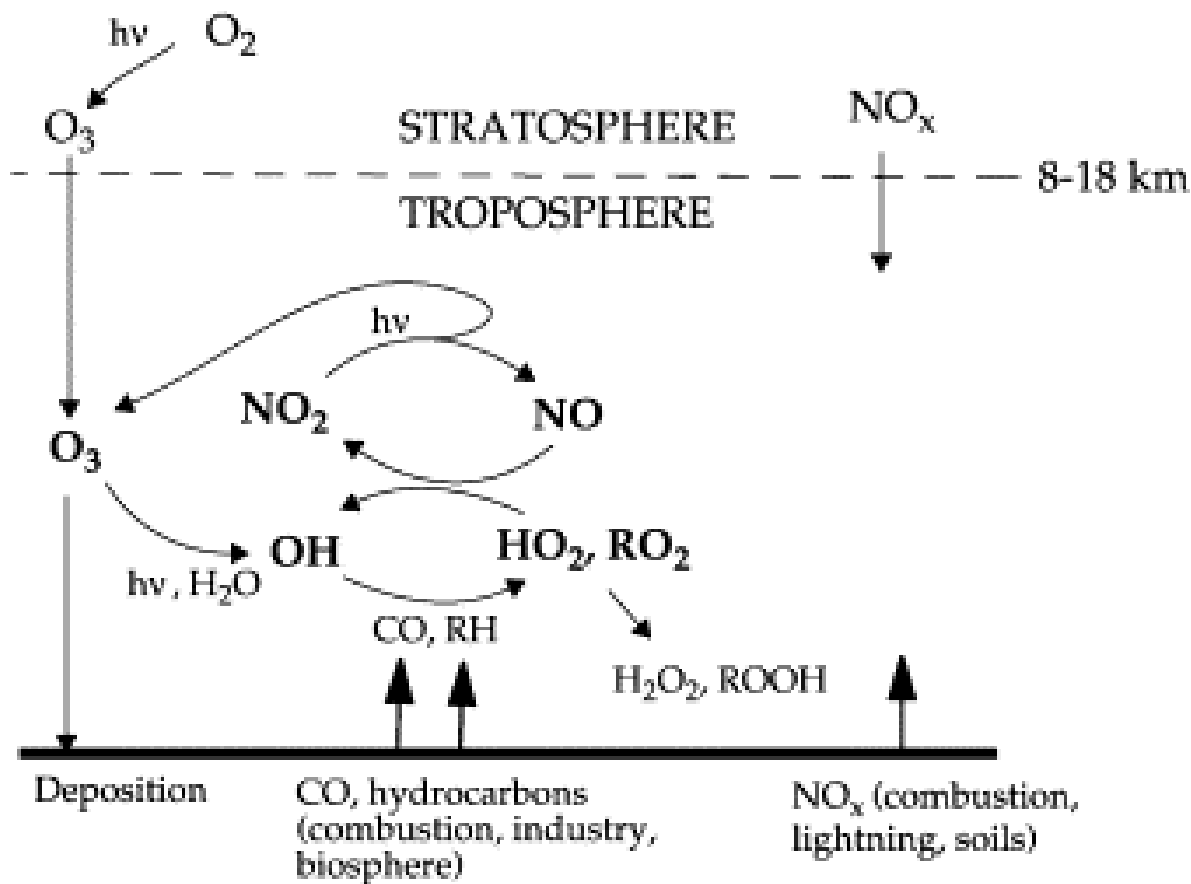
Figure 1.1. Schematic of tropospheric ozone production (Figure reproduced from reference)[96].

1.4.2. Correlation of DED Prevalence with Tropospheric Ozone

Although there is significant scientific evidence as to the impact of increased ground-levels of tropospheric ozone on climate change, it may also have adverse impacts on human health. Instances of photochemical smog with high ozone concentrations (200 ppb in Los Angeles [103] and 154 ppb in Beijing [104] for example) have been previously reported. There is extensive evidence on the adverse effects of being exposed to high ozone concentrations on the pulmonary health [95]. For example, a negative impact was found when correlating lifelong ozone exposure to lung function [95,105,106]. Moreover, higher ozone concentrations were associated with a higher risk of death from pulmonary diseases [107].

In recent years, there have been a number of studies focused on the correlation between ocular surface related diseases and exposure to air pollutants. A large-scale study focused on the ocular health of USA veterans was able to identify (with a confidence interval of 95%) air pollution as

well as atmospheric pressure as the most influential risk factors for the emergence or exacerbation of DED in the USA veteran population [108,109]. In a follow up study on the same population, the seasonal pattern of DED prevalence was also acknowledged i.e. more prevalent in the winter and spring and less so in the summer [110]. In another time-stratified case crossover study in the province of Zhejiang in China, the outpatient conjunctivitis visits were strongly associated (confidence interval of 95%) with increased concentrations of air pollutants [111]. A similar approach was used in Hangzhou, China for outpatient DED visits and a similar strong association was found with increased levels of air pollutants [70]. Evidence of correlation between higher concentrations of pollutants and DED prevalence was also provided in a smaller size study by the National Eye Institute in USA [112].

Figures 1.2 and 1.3 were created from the results of the 2016 smog event analysis of Lahore for easier demonstration of the reported data [71]. This comparative cross-sectional study was performed in the form of comparison of both number of ocular surface disease patients from target hospitals as well as the comparison of the concentrations of air pollutants $PM_{2.5}$, PM_{10}, O_3, VOC (volatile organic compounds), CO, SO_2, NO_x, NO_2, and NO on the same days in the November of 2016 in the smog event of Lahore and 2015 as the baseline. The increase of the air pollutant concentrations consisted of a seventeen-fold increase in NO_x, six-fold increase in PM_{10}, four-fold increase in O_3 and SO_2 and a two-fold increase in CO, VOC as well as $PM_{2.5}$. Along with these increases, an overall 60% increase was reported in the number of patients with ocular surface diseases, with dry eye, irritation and lid erosion contributing the most to this increase [71].

A population-based epidemiologic study by The Korea National Health and Nutrition Examination Survey (KNHANES) conducted between 2010-2012 revealed strong associations (with a confidence interval of 95%) between the prevalence of DED and higher ozone concentrations as well as lower humidity [72]. With the aim of providing a more complete study, this work was improved in 2016-2018 by studying the changes in the clinical parameters of DED according to pollutants' concentrations rather than relying on the questionnaire [113]. These parameters included Ocular surface discomfort index (OSDI) score, tear film break-up time (TBUT), corneal fluorescein staining score (CFSS), as well as measured tear secretion levels. An increased Ocular surface discomfort index (OSDI) score as well as reduced tear secretion was

associated with higher ground-levels of ozone [113]. Moreover, exposure to ozone led to the exacerbation of allergic conjunctivitis and the deterioration of the ocular surface in mice [114].

In a large-scale DED prevalence study from 32 cities in China aiming at identifying and updating the risk factors of DED, prevalence of 61.57% was reported for DED and air pollutants O_3, $PM_{2.5}$, and SO_2 were reported as DED risk factors [68]. A recent and similar report was provided signifying the correlation between DED patients younger than 60 years [115] and O_3 concentrations. Moreover, long term exposure to ozone has been linked with increasing inflammation via the increase in inflammatory cytokines, oxidative damage, as well as diminishing production of tears and reducing conjunctival goblet cell density [116,117].

Thus, there is quite a lot of evidence corroborating that ozone has adverse effects on the ocular surface health. However, very little research has focused on the impact of ozone exposure on biophyscal and mechanical properties of the TFLL. Exposure to ozone will lead to the oxidation of the unsaturated bonds in the acyl chains of TFLL components. According to a quantification study on the lipid species of meibum and their resulting molecular lipid speciation of the major classes of TFLL lipids, 43 mol% of the cholesteryl esters of meibum contain monounsaturated or di-unsaturated species [30]. 85.9 mol % of the wax esters also contain unsaturation in their acyl chains [30]. This proportion is 74 mol% for triglycerides, 100 mol% for OAHFAs and 93 mol% for PCs [30]. In a study by Georgiev et al. 2019, aiming at understanding the effect of saturation on the tear film stability and rheological properties, it was explained that there must be an important balance between the saturation and unsaturation of the tear film [118]. This is due to the clear need for a lipid ordering in the tear film in order to resist the imposed force of blinking coexisting with the fact that too much lipid ordering will lead to lipid aggregates and impact spreading ability of the tear film [118].
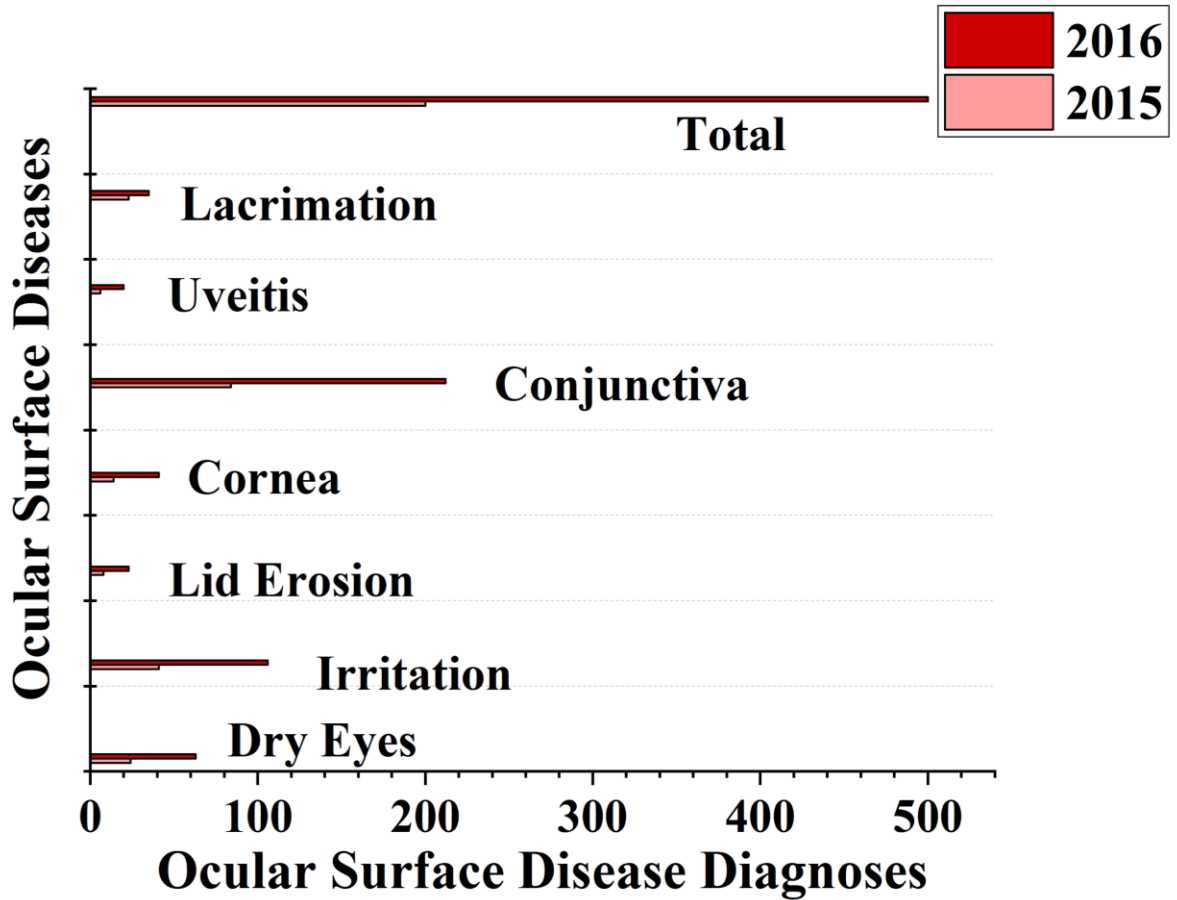
Figure 1.2.Comparison of the number of patients with ocular surface diseases (Lacrimation, Uveitis, Conjunctiva, Cornea disease, Lid Erosion, Irritation and Dry Eyes) on the same days in the 2016 smog event of Lahore vs. 2015 (Data taken from reference[71])
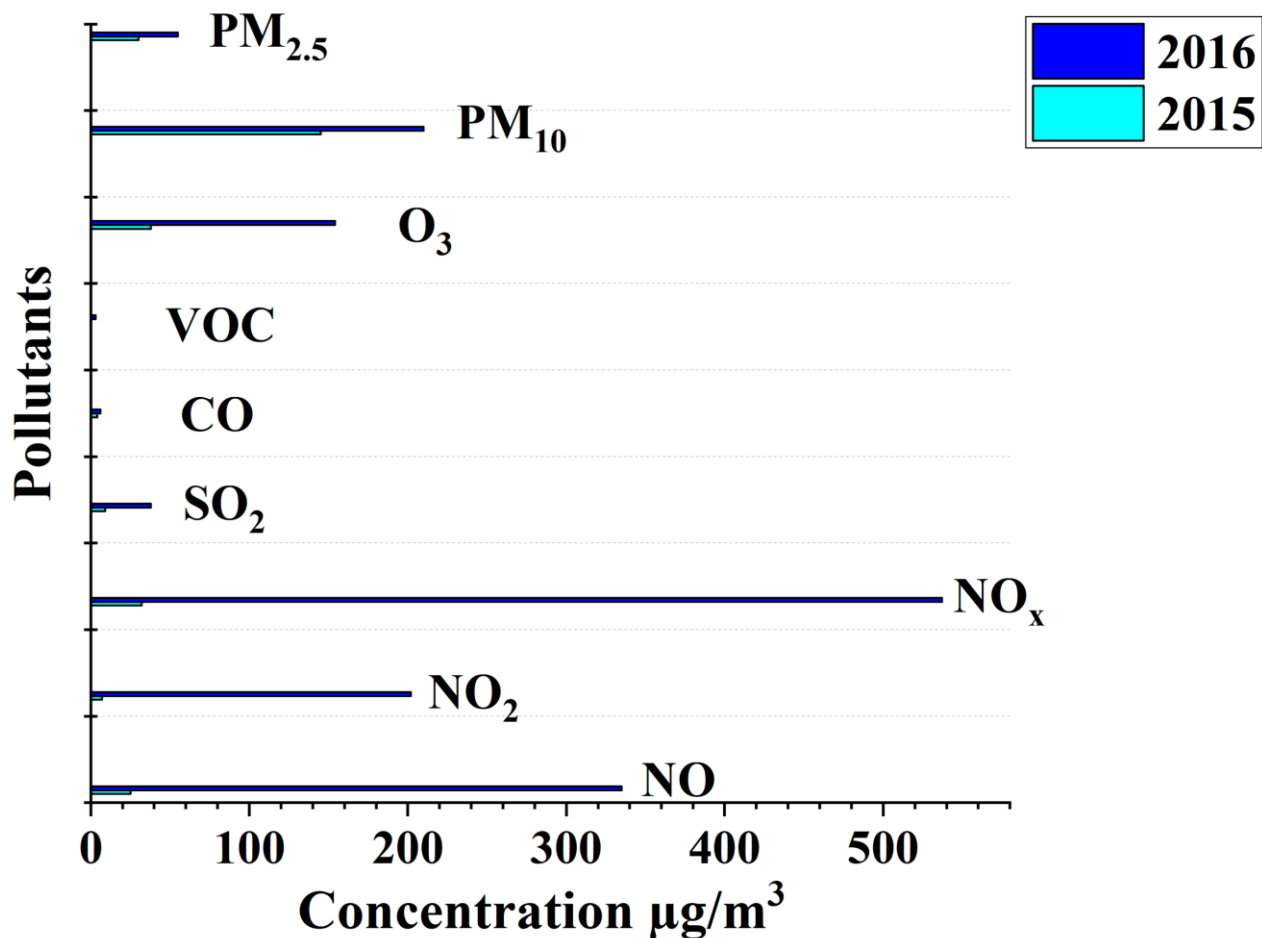
Figure 1.3.Comparison of the concentrations of air pollutants (PM₂.₅,PM₁₀, O₃, VOC, CO, SO₂, NOₓ, NO₂,and NO) on the same days in the 2016 smog event of Lahore vs. 2015 (Data taken from reference [71])

The unsaturated bond of the acyl chain of the TFLL species undergoes oxidation by ozone via the Criegee mechanism of ozonolysis and produces aldehydes, carboxylic acids, peroxides and occasionally a more stable ozonide [119–123]. Figure 1.4 presents a schematic of this reaction and the products of the ozonolysis of cholesteryl oleate via the Criegee mechanism. A more detailed description of this mechanism is provided in Appendix A (Figure A1).
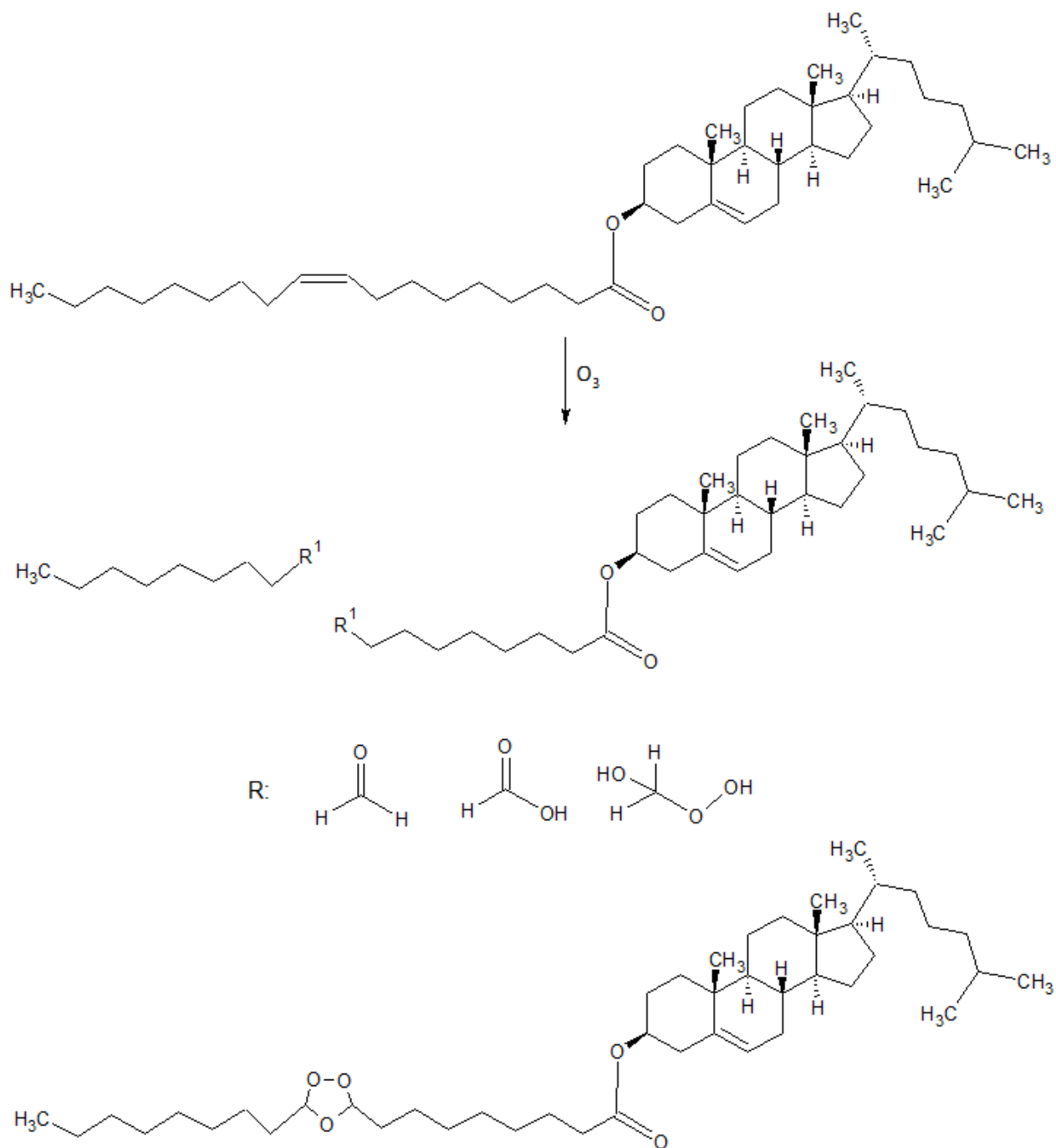
Figure 1.4. Ozonolysis of cholesteryl oleate (CO) via the Criegee mechanism.

1.5. Research Objectives

The focus of this work is the investigation of the impact of oxidation by ozone on the surface activity, morphology, re-spreadability as well as rheological properties of TFLL model membranes as a function of their composition. In recent years, a minimalistic approach has been

adopted for model membrane studies with the aim of simplifying the study of the role of the TFLL lipid families in its structure and function [12,61]. In this work, a systematic approach has been coupled with this minimalistic direction in the study of the TFLL model membranes. A more detailed study of the biophysical characteristics of cholesteryl oleate (CO) films and their liquid crystalline structure was performed as non-polar and hydrophobic cholesteryl esters are major components of physiological TFLL of which CO is one of the major constituents.
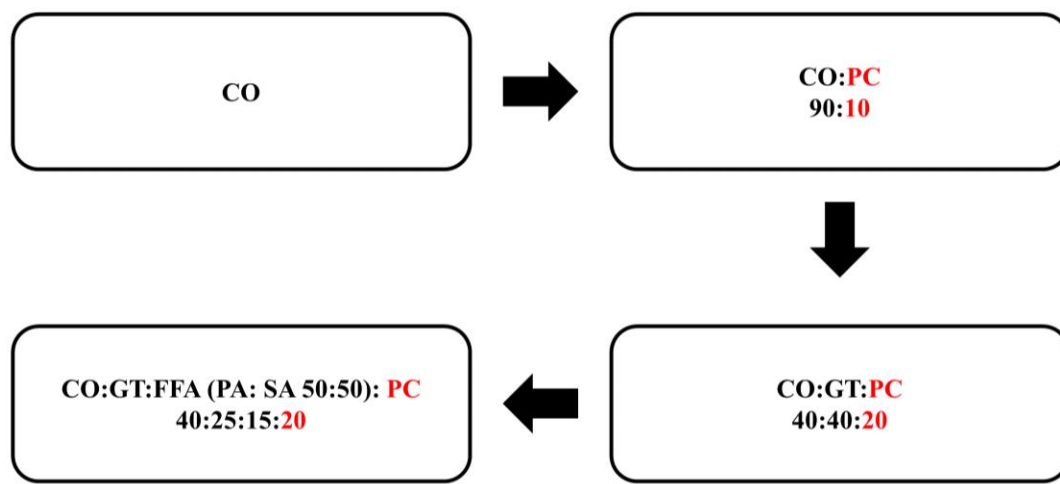
Figure 1.5. Schematic of the systematic approach to the study of TFLL model membrane systems.

A TFLL mimicking binary mixture was then chosen with 90 mol% of CO representing cholesteryl esters and 10 mol% L-α-phosphatidylcholine (egg PC) to represent the polar interface of TFLL between the aqueous layer of the tear film and TFLL. The next TFLL model membrane was produced by adding glyceryl trioleate (GT) as another non-polar lipid component, representing triglycerides with the ternary mixture composition being CO: GT: PC 40:40:20. The next and the most complex of the TFLL mimicking model membranes in this work was created by adding a mixture of palmitic acid and stearic acid as free fatty acid representatives (FFAs), making the quaternary mixture composition to CO:GT:FFA:PC 40:25:15:20. This systematic approach is effective in the study of the impact of each lipid family on the structure and function of TFLL model membranes. Once these roles have been established, the impact of ozone exposure on the biophysical properties of the TFLL model membranes can be evaluated following the same systematic approach; this aids in better understanding the impact of ozone

exposure on the biophysical properties of the TFLL model membranes as a function of composition.
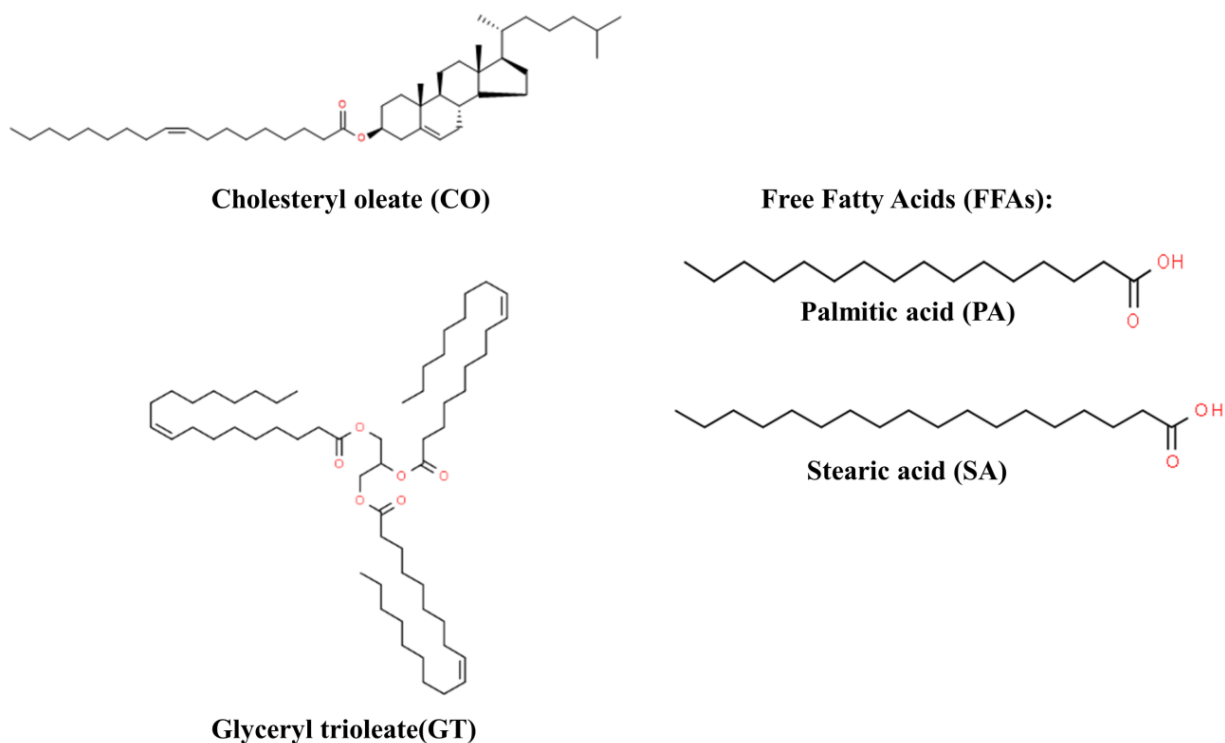
Figure 1.6. Representative non-polar lipids of TFLL model membranes.
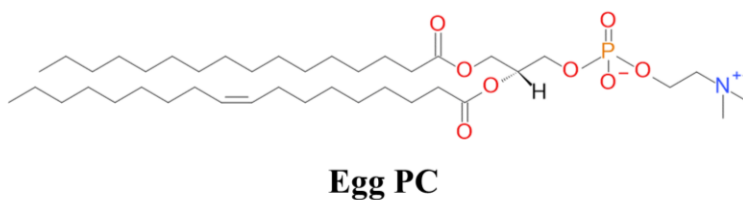
Figure 1.7. Representative polar lipids of TFLL model membranes.

For all systems, the techniques used for the study of surface activity, morphology, re-spreadability and rheology of the model membranes were employed i.e. Langmuir balance, Brewster Angle Microscopy (BAM) and Profile Analysis Tensiometer. Additionally, highly sensitive synchrotron-based X-ray surface characterization techniques were used to study the CO liquid crystalline structure i.e. Grazing Incidence X-Ray Diffraction (GIXD), X-Ray Reflectivity

(XR) as well as Grazing Incidence X-ray Off-specular Scattering (GIXOS). These techniques are summarized in the next part of the introduction.

1.6. Experimental Techniques for Studying Model Membranes

This review will focus on a summary of the techniques used in the study of model membranes' biophysical characteristics.

1.6.1. Langmuir Film Balance, Surface Activity

Figure 1.8 depicts a schematic of a Langmuir balance. The fundamental basis for the study of the air-water interface was initially developed by Pockels [124] and Langmuir [125] and they are used to this day very much the same way. The Langmuir balance (made from Teflon) is filled with water or the subphase of choice and it is equipped with either one or two controlled Teflon barriers that slide over the surface, creating an enclosed area whose parameters are increased or decreased using the barriers, depending on the experimental need. A filter paper or wire connected to a pressure sensor is used as a Wilhemy plate [126]. Immersed in the water, it measures the surface tension while the plate in being pulled down due to the surface tension [126]. Using a syringe, appropriate quantities of a surfactant solution are spread on the water/subphase surface, thus creating a monolayer film whose surface tension is measured leading to a measurement of its surface pressure π defined as the difference between the surface tension of pure water γ_0 and the surface tension in the presence of a film γ. The compression of the film is achieved as the barriers close and reduce the area available to the molecules of the film. Thus, the film undergoes structural changes which affect its surface pressure, leading to a surface pressure vs. molecular area isotherm.
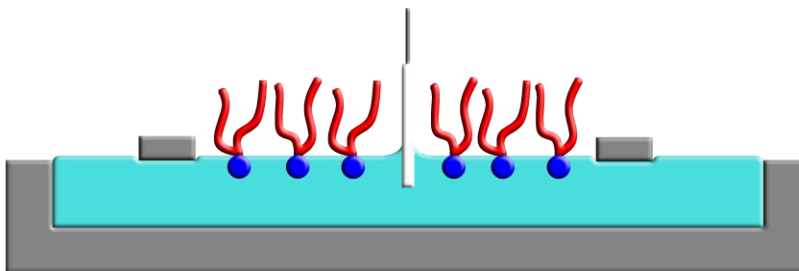
Figure 1.8. Schematic of Langmuir balance.

17

Figure 1.9 shows a schematic of a generic surface pressure vs. molecular area compression isotherm of a lipid monolayer at the air-liquid interface. At high molecular area, the lipids are in the gaseous phase where there is little to no interaction between the lipid molecules and the surface pressure remains at zero mNm[-1]. As the monolayer film is compressed, the molecular area is reduced and the lipid molecules interact to form a fluid, liquid expanded (LE) phase where the film has high fluidity and compressibility. This coherent film reduces the surface tension and so the surface pressure rises as the film is compressed. As the film is compressed even further, some lipids can pack together to form a condensed phase in which the alkyl chains are in their all-trans, fully extended conformation and are closely packed with liquid-crystalline order. Thus the fluidity and compressibility are lowered. The monolayer collapses when there is no more molecular area available to the lipids. The interactions of the molecules of the film lead to the formation of these two-dimensional phases which have been confirmed using several techniques, including diffraction [127].
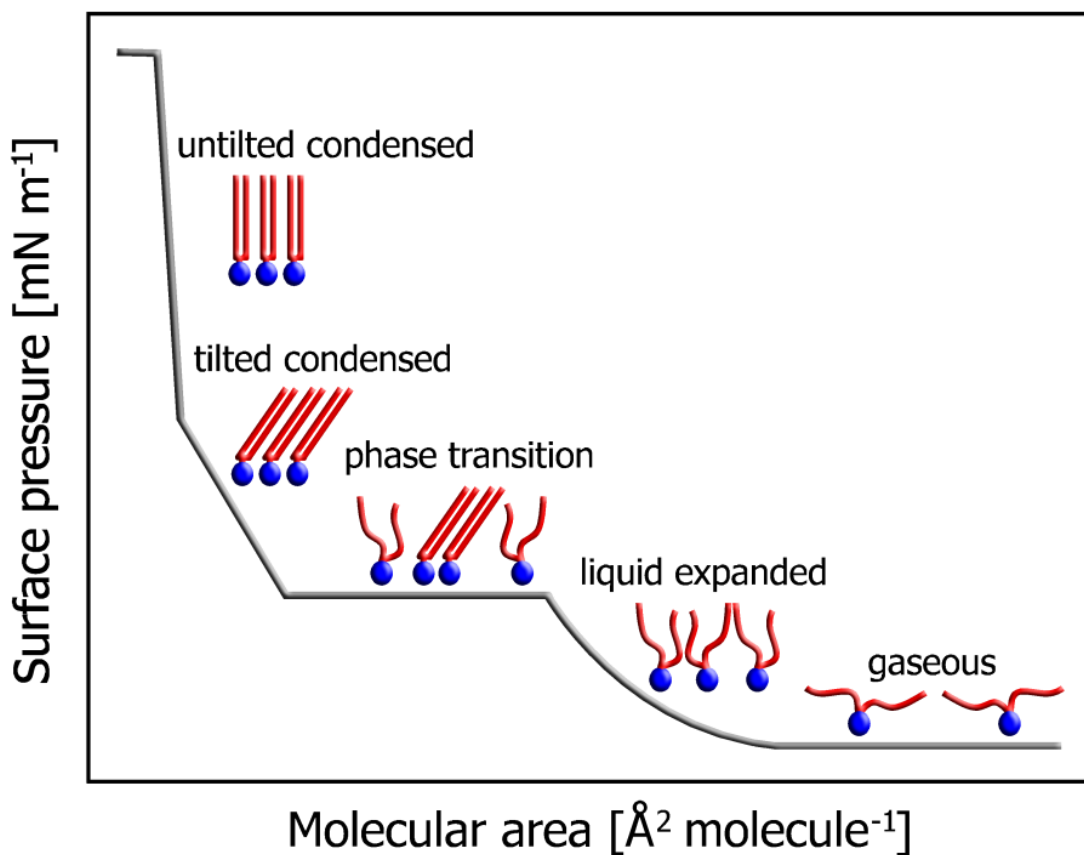
Figure 1.9. Schematic of surface-pressure vs. area isotherm.

18

1.6.2. Profile Analysis Tensiometer, Rheology

Rheology or viscoelasticity is explained in terms of elasticity as well as viscosity, the first describing a material's recovering capacity following the elimination of a force applied to it, and the latter elucidated as the resistance capacity of a material to flow and deformations after a force is imposed on it [95]. The rheology of surfactant films dictates their stability and performance [95,128]. The TFLL has to undergo a number of dynamic processes and deformations such as the spreading of the film and then its compression while blinking, tear flow and evaporation as well as lipid secretion from the meibomian glands, thus, the rheology of TFLL is quite an important characteristic to study [12]. Specifically for the TFLL and the blinking function, dilational rheology is paramount as it directly relates the oscillations caused by the change in surface area and therefore surface tension to the viscoelastic properties of the film [95,129].

Dilational rheology measurements are performed using Profile Analysis Tensiometer (PAT). In order to perform rheological measurements, appropriate quantities of a surfactant solution are spread on a pendant drop composed of water or subphase of choice (Figure 1.10). After the equilibration time of the film passes, a program specific to the film is employed. As the volume and therefore the surface area of the drop is controllable, the film is compressed to a target surface pressure, equilibrates, then oscillated at a target frequency with a specific amplitude chosen based on the experimental conditions [130,131], equilibrates again, and thus this cycle continues until a drop surface area of 15 mm^2 is reached which is the smallest stable area reachable by the drop. Each program is created based on the surface pressure vs. molecular area isotherm of each specific film in order to ensure that with each compression stage in the program, a change of 1 mNm^{-1} in the surface pressure is achieved.

The axisymmetric drop shape analysis (ASDA) [130,132,133] is employed as well as the visual profile of the drop to calculate the surface pressure. The Young-Laplace equation is used to relate the arc of the drop to surface pressure [130,134]. In rheology measurements, the result is a complex elastic modulus which can relate the drop surface area oscillations to the surface tension [133]. This complex modulus is separated into dilational elasticity and dilational viscosity of the film [130]. Therefore, it is important that the drop maintains a Laplacian shape throughout the measurements [135]. The oscillation frequency and the amplitude can affect the rheology measurements, and so

They dictate the experimental parameters so that the film is not disturbed both in terms of hormonic distortions as well as drop loss during the measurements [130–132,136,137].
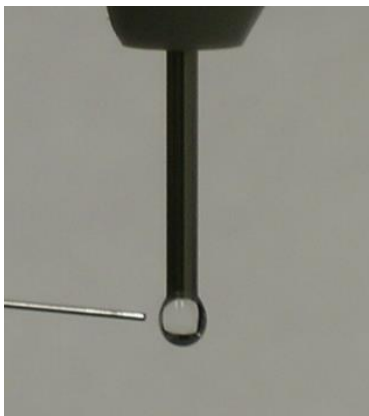
Figure 1.10. Spreading a film on a pendant drop.

Figure 1.11 shows the schematic of the experimental setup starting from ozone generation to film exposure on a pendant drop. Ozone was generated by first passing compressed air through a drying tube filled with the drying agent Drierite™ (anhydrous calcium sulfate) in order to remove water. Then, to generate hydrocarbon-free air, the dry air was passed through a VOC scrubber and a ChromGas zero air generator (Parker), after which a UVP ozone generator equipped with a Pen-Ray lamp (wavelength 185 nm, power 2 to 20 watts) was used to generate ozone. A 2B Technology ozone monitor was used to measure and monitor the ozone concentration based the absorption level of UV light at 254 nm. Using an Aalborg digital mass flow controller, the flow rate of the generated ozone gas was controlled before entering the reaction chamber. Figure 1.12 shows the schematic of the ozone exposure of a representative oleic acid film spread on a pendant drop.
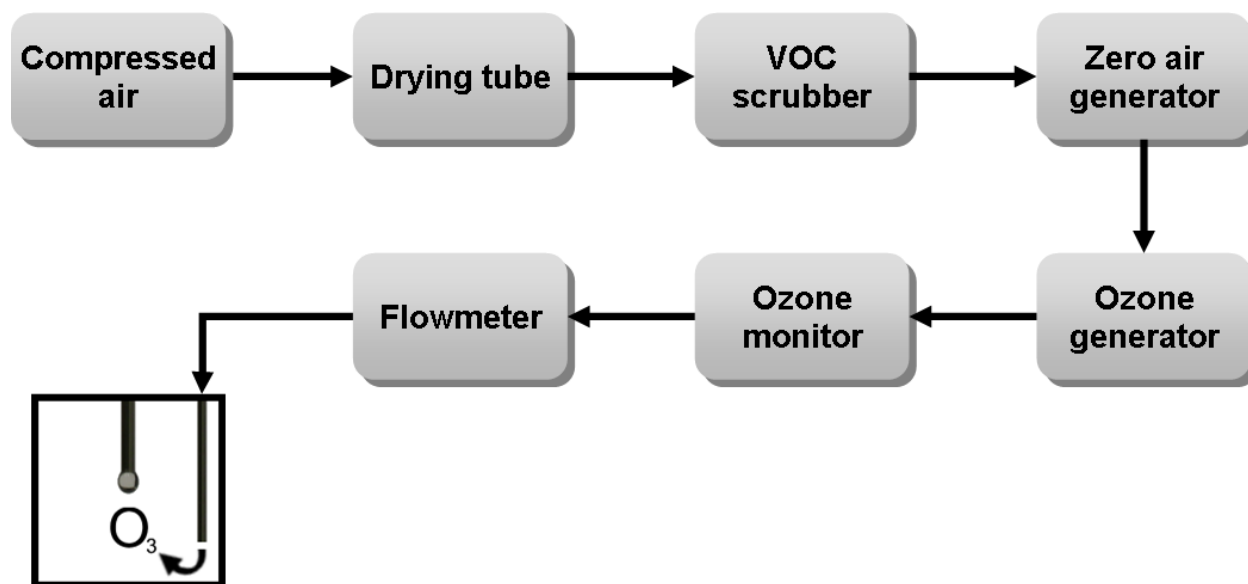
Figure 1.11. Schematic of the experimental setup used for ozone exposure of a film spread on a pendant drop.
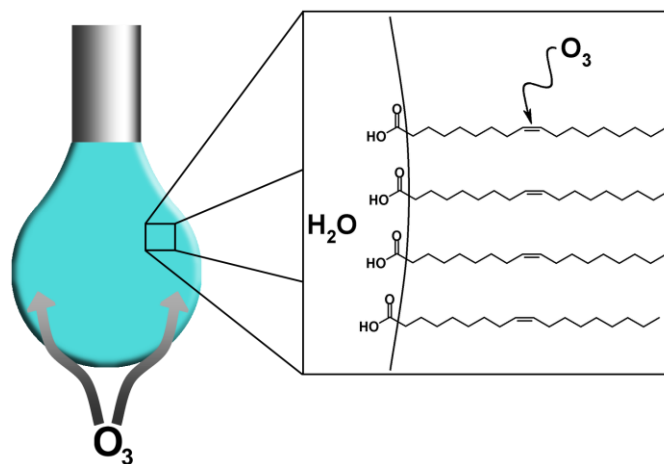
Figure 1.12. Schematic of the ozone exposure of an oleic acid film spread on a pendant drop.

1.6.3. Brewster Angle Microscopy, Morphology

Brewster Angle Microscopy (BAM) is a visualization technique used to study the morphology of the surfactant films spread at the air-water interface. It works on the basis of light reflection between the perfect interface of two non-absorbing media with different refractive indices and Brewster angle [138]. As a result of Fresnel's formula [138] p-polarized light directed at this interface at Brewster angle α is not reflected. However, should a film of surfactant molecules be spread at

this interface, α will no longer correspond to Brewster angle and therefore light is reflected which can in turn be detected with a microscope located at Brewster angle. Thus, this method allows the visualization of the morphology of amphiphilic films, spread at the air-water interface [138]. Figure 1.13 shows the schematic of the physical basis of Brewster Angle Microscopy.
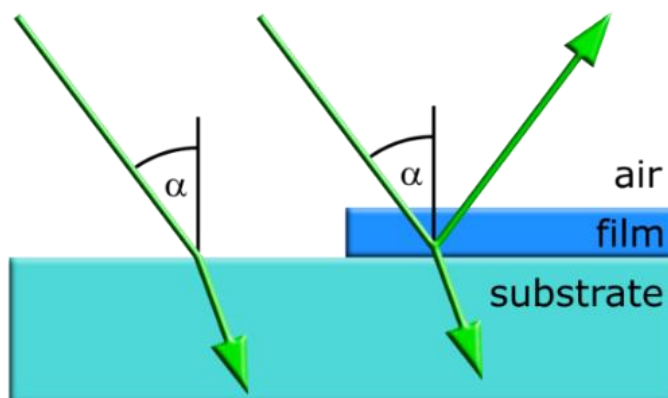
Figure 1.13. Schematic of the physical principle of Brewster Angle Microscopy.

Figure 1.14 shows the experimental setup of ozone exposure experiments, performed on the Langmuir trough for surface activity, compression-expansion cycles, and BAM experiments by enclosing the trough with a Plexiglass cover with and inlet and outlet at opposite ends. The same ozone generator setup was used in this experiment as that for pendant drop experiments (1.6.2).
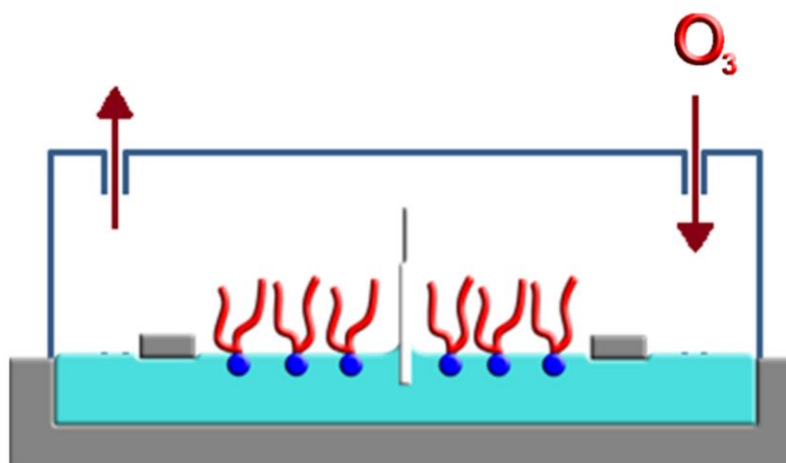
Figure 1.14. Schematic of ozone exposure setup on a Langmuir balance.

1.6.4. X-Ray Techniques

Synchrotron based X-ray surface characterization techniques are quite important in monolayer studies. This part of the introduction is dedicated to a brief summary of these techniques.
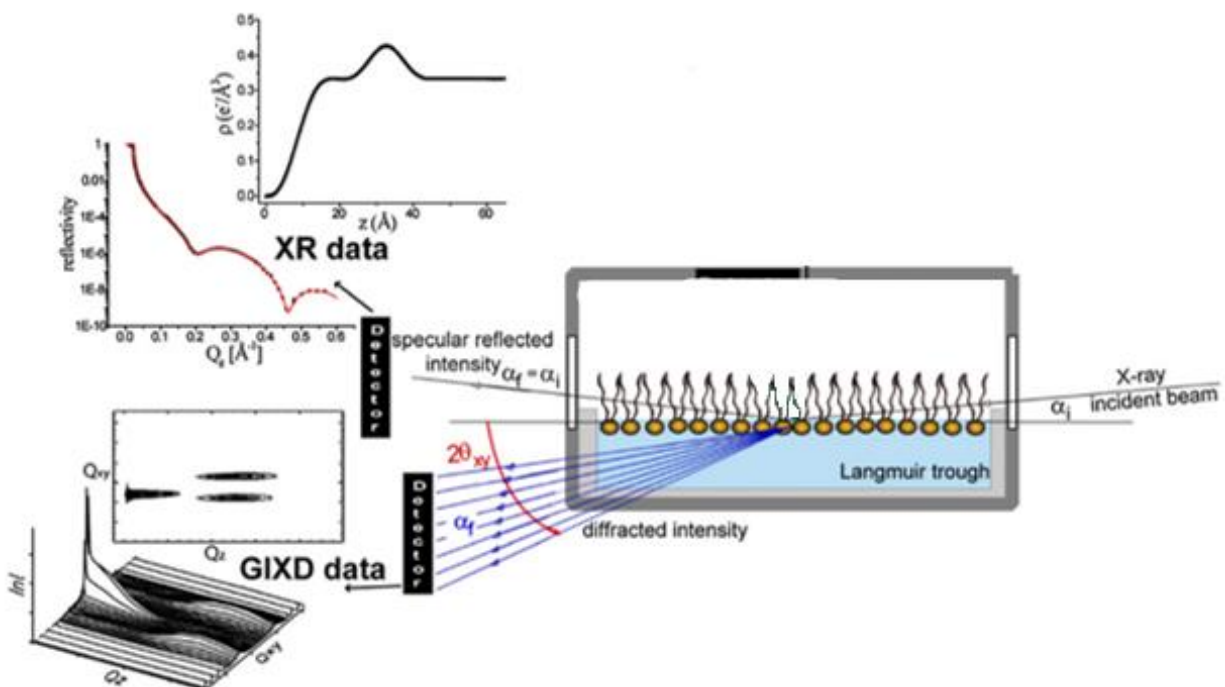
Figure 1.15. Basic principles of X-ray surface characterisation techniques Grazing Incidence X-Ray Diffraction (GIXD) and X-Ray Reflectivity (XR)-(Image modified from [139]).

1.6.4.1. Grazing Incidence X-Ray Diffraction (GIXD)

Grazing Incidence X-Ray Diffraction (GIXD) is one of the most important techniques in the study of lateral organization of films formed at the air-water interface. A monochromatic X-ray beam is directed at an angle marginally smaller than the critical angle for total reflection between the interface of two media with different refractive indices. Thus, the wave moves nearly parallel to the surface, leading to the illumination of only the upper 8 nm of the surface, making this technique highly surface sensitive and optimal for the study of the two-dimensional crystalline powder structures formed by films at the air-water interface [139]. The periodicity in this crystalline structure results in a diffraction that is determined by horizontal and vertical scattering vector components Q_{xy} and Q_z (in-plane and out of plane) respectively [139]. By the analysis of the diffraction pattern, valuable structural information can be obtained.

Bragg peaks are acquired by integrating the intensity over a Q_z window and model Lorentzian peaks are used to fit the Bragg peaks and obtain their full width at half maximum (fwhm) as well as their Q_{xy} position which in turn, are used to calculate the lattice d spacing (equation 1.1) as well as in-plane correlation length using the Scherrer formula (equation 1.3) [139–141]. The peak positions and patterns correspond to specific unit cells as previously described [127].

$$d = 2\pi/Q_{xy}$$ Equation 1.1. Lattice d spacing.

The full width at half maximum (fwhm) of the Bragg peaks is corrected for the instrumental resolution (0.0084 Å-1) (equation 1.2) [139–141].

$$fwhm_{intrinsic}(q_{xy}) = [fwhm_{intrinsic}(q_{xy})^2 - fwhm_{resolution}(q_{xy})^2]^{1/2}$$ Equation 1.2. Correction for instrumental resolution of the full width at half maximum (fwhm) of the Bragg peaks [139–141]

$$x_{xy} \sim 0.9 \times 2\,\pi/fwhm_{intrinsic}(q_{xy})$$ Equation 1.3. The Scherrer formula for the calculation of in-plane correlation length [139–141]

Bragg rods are obtained by integrating the intensity over a Q_{xy} and model Gaussian peaks are used to fit the Bragg rods and acquire their full width at half maximum (fwhm) and their Q_z position. The out-of-plane position is used to determine the tilt angle of the molecule with respect to the normal (higher Qz values correspond to higher tilt angles). The fwhm of the Bragg rod is used to calculate the vertical correlation length (corresponding to the thickness of the crystalline region) using the Scherrer formula (equation 1.4) [139–142].

$$L \sim 0.9 \times 2\,\pi/fwhm(q_z)$$ Equation 1.4. The Scherrer formula for the calculation of the vertical correlation length [139–142].

1.6.4.2. X-Ray Reflectivity (XR)

As opposed to GIXD which can only give information on the crystalline structure of the film (condensed phase), X-ray reflectivity (XR) gives information about the vertical structure of the film regardless of its phase [139]. In this technique, the incident beam is angled at the angle of specular reflection (Figure 1.15) [139]. The measurement of X-ray reflectivity is performed in terms of the vertical scattering vector component (Q_z), leading to the measurement of the electron

density $\rho(z)$ variation of the vertical structure of layers formed at the air-water interface. The measured XR R (Q_z) is normalized by the Fresnel reflectivity R_F (Q_z) which is calculated for a perfectly sharp air-water interface [139,141]. The Parratt method is used for the calculation of the X-ray reflectivity [141,143–146]. A slab model is used to find the most appropriate presentation of the film as a stack of slabs through the best matching of the scattering profiles. Each slab has specific structural characteristics with a constant thickness and electron density. The average of the electron density profile ρ (z) is calculated over both the ordered and disordered parts of the film under the X-ray beam footprint by a sum of error functions (Equation 1.5) [141,147,148].

$$\rho(z) = \frac{1}{2}\sum_{i-0}^{N-1} erf\left(\frac{z-z_i}{\sqrt{2}\sigma}\right)(\rho_{i+1} - \rho_i) + \frac{\rho_0 + \rho_N}{2}$$ Equation   1.5.   The   electron   density profile[141,147,148].

The erf(z) in equation 5 is calculated as $erf(z) = (2/\sqrt{\pi})\int_0^z e^{-t^2} dt$ and N is the number of internal interfaces. σ is the surface roughness calculated from capillary wave theory, z_i is the position of the ith interface, ρ_i is the electron density of the ith interface, and ρ_0 is the electron density of the aqueous subphase [141,147,148].

1.6.4.3. Grazing Incidence X-Ray Off-Specular Scattering (GIXOS)

Grazing Incidence X-Ray Off-Specular Scattering (GIXOS) provides similar structural information on the film to XR and it is used as a more rapid alternative [146]. GIXOS is especially useful for the study of new and unknown systems and in particular ones that form multilayers as that formation can be very dynamic. The sensitivity of GIXOS stems from the grazing incidence geometry with a depth of x-ray penetration of normally 3 nm [146]. Although GIXOS is an inherently lower resolution technique, it is a far less complex method as, unlike XR, no movement in the steering crystal, sample or detector is needed and it has a fixed geometry which reduces the typical damaging of the sample by X-ray [146]. Thus, it is a faster and intriguing alternative to XR when time is of essence, the system is unknown and there is a possibility of a change in the structure of the film during the time required for XR measurements (15 minutes as opposed to 75 minutes). The GIXOS data is normalized to the intensity of the first minimum I_n which is quite a reproducible region and it leads to more reliable GIXOS data analysis [146]. In GIXOS data analysis, the scattering from the background is subtracted. A similar slab model

technique to XR is used to map the electron density variation $\rho(z)$ of the film's vertical structure as a stack of slabs with characteristic thickness and electron density.

1.7. Outline of Manuscripts

Three manuscripts are included in this research (Chapters 2, 3 &4):

The first manuscript (Chapter 2) focuses on the study of the surface activity, morphology, re-spreadability and rheology of the binary, ternary, and quaternary mixtures in order to determine the roles of each representative lipid family in TFLL structure and function.

The second manuscript (Chapter 3) focuses on a detailed study of the liquid crystalline structure of CO as the major non-polar lipid of the TFLL model membranes.

The third manuscript (Chapter 4) studies the impact of ozone exposure on the biophysical properties of TFLL model membranes which are correlated with ESI-MS analysis of all the products of the surface ozone reaction.

Chapter 2. A Biophysical Study of Tear Film Lipid Layer Model Membranes

2.1. Abstract

Tear film lipid layer (TFLL), the final layer of the human tear film is one of the most important interfaces in the body, responsible for surface tension reduction while blinking, water evaporation retardation and maintaining the stability of the tear film. The study of the composition-structure-function relationship of TFLL is paramount, as a compromised structure of TFLL leads to the emergence of dry eye disease (DED) which is one the most prevalent ophthalmic surface diseases of the modern world, associated with chronic pain and reduced visual capability. In this model membrane study, a systematic approach is used to study the biophysical properties of TFLL model membranes as a function of composition. Three model membranes are studied along with their individual components. Comprised of cholesteryl oleate (CO), glyceryl trioleate (GT), L-α-phosphatidylcholine (egg PC) and a free fatty acid mixture, the models become progressively more complex from binary to quaternary mixtures, allowing the role of each individual lipid to be derived. Langmuir balance, Brewster Angle Microscopy (BAM) and Profile Analysis tensiometer (PAT) are used to study the surface activity and compression-expansion cycles, morphology, and rheological behaviour of the model membranes, respectively. Evidence of multilayering is observed with inclusion of CO and a reversible collapse is associated with the GT phase transition. An initially more coherent film is observed due to the addition of polar PC. Notably, these individual behaviours are retained in the mixed films and suggest a possible role for each physiological component of TFLL.

2.2. Introduction

The human tear film lipid layer (TFLL) is the outermost layer of the tear film which covers the aqueous tear film and is an important interface in the body [1]. This interface is crucial in helping with the respreading of the tear film after each blink using its surface properties, as well as maintaining the tear film stability [6–8] and prevention of water evaporation from the eyes [1,7–11]. The thickness of the human TFLL is an estimated 15-160 nm, possibly close to 30 nm and 5 to 20 molecules thick [1,12,14,15]. There are many discrepancies in the literature as to the exact

27

composition of the tear film lipid layer due to many limitations in working with extracted meibomian gland secretions (MGS) which comprise >93% of the TFLL composition [8,11,19,22–28], therefore the exact composition of TFLL is still under debate.

The overall consensus in the literature is that the TFLL is composed of > 90% non-polar lipids [1,8,11,28]. The most abundant non-polar lipid species of TFLL are long acyl chain cholesteryl esters (CEs) (30-45 mol%) and wax esters (30-50 mol%) [1,8,11,19,22,28,29], followed by 2 to 4 mol% triglycerides [8,11,28,30], 2.5 mol% or less free fatty acids [3,28,31,32], 0.5-5.6 mol% free cholesterol [3,8,11,28,30–32], 2 mol% diesters [3,28,31,32] and 3-7 mol% hydrocarbons [3,28,31,32]. There are reportedly two classes of polar lipids that are constituents of the polar sub-layer of TFLL, creating the interface between the aqueous tear film and TFLL [1,3,8,41] : (O-Acyl)-ω-hydroxy fatty acids (OAHFA) (3-5 mol%) [19,25,33] and Phospholipids (~13 mol%) [1,8,34] .

A multilayered structure is assumed for TFLL, wherein on top of the sub-layer of amphiphilic polar lipids at aqueous tear film/TFLL, a bulky layer of non-polar hydrophobic lipids resides creating the eye-air interface [1,3,8,41]. It is suggested that as these hydrophobic lipids do not easily spread on top of the underlying aqueous layer, this sub-layer of polar amphiphilic lipids, acts in stabilizing the TFLL as well as the aqueous tear film underneath [1,3,7,8,18,24]. Notably, it has been observed previously that meibum extracts form compressible and non-collapsible films. It has been suggested that these two important characteristics can either be due to formation of multilayers or reversible folding [1,49].

Compromise in the TFLL composition, and therefore its structure can lead to dry eye disease (DED) which is one the most common ocular health diseases of today. DED impacts the quality of life in 10%-30% of the global population [64]. Characterized with an unstable tear film, DED is associated with chronic eye pain, visual disturbances, poor quality of day-to-day life and depression [8,62]. In Canada, the prevalence of DED is 21.3%, corresponding to ~6.3 million people [73]. There are many risk factors associated with DED, among which are MGD [8,65], age [64,66–68], race [62], sex [62,64,66,68,69], pollution [64,68,70–72], low humidity [64,70], use of certain medications such as antihistamines [62,66] and antidepressants [62].

According to the Tear Film & Ocular Surface Society , Dry Eye Workshop II, meibomian gland dysfunction (MGD) is reported in 86% of DED cases [62,63], associated with changes in the

secreted lipids of meibomian glands both in quality as well as quantity [79,80], likely leading to a compromise in the TFLL composition and disrupting its structure and function. Evidence of this has been previously reported in terms of reduced polar lipid content [26,27,82], significant morphological changes in the MGS film of patients with MGD [8,48] compared with that of healthy subjects, a tear film non- invasive break up time of <5 s, as opposed to > 15 s for healthy patients, indicating an impact on the stability of the tear film [8,83–86], impaired spreading ability of the TFLL film in MGD cases [87–89], as well as increased tear surface tension [6,8,90,149] and a film displaying lower elasticity and higher viscosity [48].

With all the evidence of correlations of an impaired TFLL composition and structure leading to MGD and eventually DED, it is important to understand the composition, structure, and function relationship of TFLL. Due to the highly complex and dynamic structure of TFLL, much regarding the roles of lipid families of TFLL in its structure and function remains speculative. Georgiev et al. 2017, provided a contemporary perspective on this relationship in their review [8] and a TFLL molecular level view with an emphasis on TFLL models and molecular simulations was reviewed by Cwiklik, 2016 [1].

 In recent years, a minimalistic approach has been adopted in order to simplify the understanding of the roles of the TFLL lipid families [12,61]. In the current work, a systematic approach has been chosen for creating the TFLL model membranes. A TFLL mimicking binary mixture of cholesteryl oleate (CO) representing the non-polar components of TFLL and L-α-phosphatidylcholine (egg PC) representing the polar lipids of TFLL was initially used. A more complex ternary mixture was generated by adding glyceryl trioleate (GT) as another non-polar lipid component, after which a mixture of palmitic acid and stearic acid was added as free fatty acid representatives (FFAs), creating the quaternary mixture model membrane. Such a systematic addition of lipid family representatives, aids in gleaning the possible impacts of each lipid family on the model membrane characteristics. A Langmuir balance is used to study the surface activity of the model membranes as well as enabling cycle experiments to study the respreadablity of the films. The morphology of the films was investigated using Brewster Angle Microscopy (BAM) and dilational rheology experiments were performed through pendant drop experiments using Profile Analysis Tensiometer (PAT). The findings of these experimental

techniques begin to describe the possible roles of the TFLL lipid families investigated in the TFLL functions.
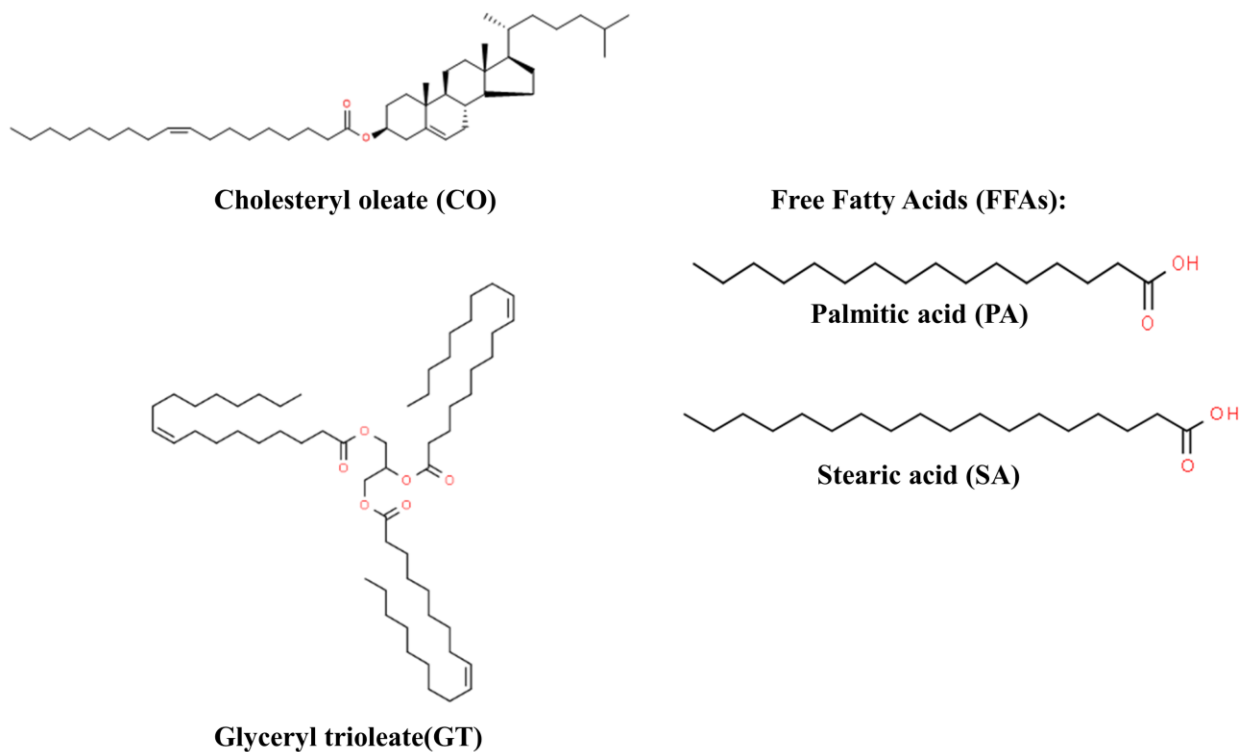
Figure 2.1. Representative non-polar lipids of TFLL model membranes.
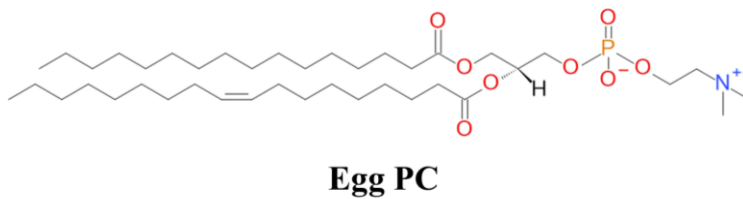
Figure 2.2. Representative polar lipid of TFLL model membranes.

2.3. Materials & Methods

Materials. L-α-phosphatidylcholine (egg PC, > 99%) was purchased from Avanti Polar Lipids. Cholesteryl oleate (CO, > 98%), glyceryl trioleate (GT, ≥99%), palmitic acid (PA, >99%), stearic acid (SA, >99%) and phosphate-buffered saline tablets (PBS, pH 7.4, 10 mM phosphate, 137 mM NaCl, 2.7 mM KCl) were all purchased from Sigma-Aldrich. In all the experiments, the spreading solvent was HPLC grade chloroform purchased from Fisher Scientific.

Preparation of Mixtures, Solutions & Subphases. The CO:PC (binary mixture) and CO:GT:PC (ternary mixture) mixtures were prepared using stock solutions of CO, Egg PC and GT to achieve molar ratio of 90:10 for the binary mixture and 40:40:20 for the ternary mixture. The FFA (free fatty acids) mixture was prepared using stock solutions of PA and SA to achieve a molar ratio of 50:50 respectively. The CO:GT:FFA:PC (Quaternary mixture) mixture was then prepared using solutions of CO, GT, FFA and Egg PC to achieve molar ratios of 40:25:15:20 respectively. Water subphases were comprised of ultrapure water with resistivity of 18.2 MΩ cm^{-1} from a Milli-Q® HX 7080 water purification system (HC). The PBS buffer was prepared by dissolving one phosphate-buffered saline tablet in 200 mL of ultrapure water.

Langmuir Film Balance, Surface Activity. Surface pressure-area isotherms were obtained using Langmuir film balance connected to a thermostated water bath. Using monolayer solutions with concentrations of up to 1.0 mg mL^{-1}, monolayers were spread at the air-buffer interface on a Langmuir trough (NIMA Technologies). A period of 10 minutes was allowed for the films to equilibrate and the chloroform solvent to evaporate, after which, the barriers of the Langmuir balance closed at a speed of 5 cm^2 min^{-1} in order to generate the surface pressure-molecular area isotherms. The surface pressure (π) was obtained using a Wilhelmy plate. For each system at least 3 reproducible measurements were obtained, within 1-2 Å^2 Molecule^{-1}.

Brewster Angle Microscopy, Morphology. Brewster Angle Microscopy (BAM) was performed through coupling the Langmuir film balance with an I-Elli2000 imaging ellipsometer (I-Elli2000, Nanofilm Technologies). This ellipsometer has a 50 mW Nd:YAG laser ($\lambda = 532$ nm). The images were obtained as the films were compressed at a speed of 5 cm^2 min^{-1} with a 20X magnification lens, a resolution of 1 μm, and an incident angle of 53.15˚.

Compression-Expansion Cycles The compression-expansion cycles were obtained by spreading the monolayer solutions at the air-buffer interface with the same experimental details as for the surface pressure-area isotherms. After the 10-minute equilibration and solvent evaporation period, the film was compressed and expanded for 6 consecutive cycles at the speed of (196 cm^2 min^{-1}) which is the highest achievable speed with the Langmuir trough. Each measurement was repeated at least 3 times.

Profile Analysis Tensiometer, Rheology. Rheological measurements were performed using a SINTERFACE profile analysis tensiometer (PAT). A detailed description of this technique can be found in the literature [150–152]. The tear film lipid layer model membrane films were spread (spreading solution concentration approximately 0.1 mg mL^{-1}) on a pendant drop with a volume of 13 µL at the area of 32 mm^2. The drop was allowed to equilibrate for 3 minutes, after which, the area was increased to 40 mm^2 and allowed to equilibrate for an additional 3 minutes. After the equilibration time, the drop area was adjusted to 40 mm^2. A pre-programmed set of molecular area steps (described below) was used to perform rheological measurements on the films at different surface pressures along the isotherm.

The PAT employs axisymmetric drop shape analysis (ASDA) [130,132,133] and the profile of the drop to calculate surface pressure, using the Young-Laplace equation to relate the arc of the drop to surface pressure[130,134]. Thus, the drop must keep its Laplacian shape throughout the measurements. It has been previously reported that the oscillation frequency as well as the amplitude can impact the rheological measurements and they must be selected such that that there is little disturbance to the films in terms of hormonic distortions and drop loss during the measurements [130–132,136,137]. The amplitude of 2.50 % (of the drop area) was chosen in order to minimize such effects [130] and the frequency of 0.16 Hz calculated from the frequency of blinking i.e. 10 blinks per minute in normal subjects as reported previously in the literature [153] to be physiologically relevant.

For each film, a unique, stepwise program was designed to account for the changes in the slope of the surface pressure-area isotherms of each model membrane film. This ensures that sufficient measurement points are taken to ensure maximum surface pressure coverage (each 1 mN min $^{-1}$ change in the surface pressure). For the CO:PC 90:10 (binary mixture), there was an initial

compression from 40 mm^2 to 37 mm^2, after which the drop was allowed to equilibrate for 300 seconds. The drop then underwent 25 oscillations for 156.25 s with an amplitude of 2.50 % (of the drop area) and a frequency of 0.16 Hz [153]. After the oscillations, the drop was equilibrated for 180 s, and compressed to 34 mm^2, equilibrated (300 s), and underwent oscillations of the same parameters explained above. This cycle was repeated 4 times in total until the next part of the program, where due to the slope change in the isotherm of the binary mixture, the change in the drop area was reduced so that the 1 mN min $^{-1}$ change was still maintained. After the 5th oscillations cycle and the equilibration time (180 s), the drop area was reduced from 25 mm^2 to 24.2 mm$^{2.}$ From this point on, the same cycle was repeated until at last the drop reached an area of 15.1 mm^2 and the rheology measurements were complete providing the measurements of viscosity and elasticity of the film along the entire isotherm[130,132,134].

For the CO:GT:PC 40:40:20 (ternary mixture) the initial compression was from 40 mm^2 to 38.66 mm^2, after which the drop was equilibrated (300 s) and oscillated with the same parameters as explained before. After the second set of oscillations and the following equilibration time (180 s), a change in the drop area reduction was needed for a 1 mN min $^{-1}$ increase to occur in the surface pressure. Thus, the third compression comprised of the reduction of the drop area from 37.33 mm^2 to 35.69 mm^2, followed by equilibration (300 s), oscillations with the same parameters as before, equilibration (180 s) and the next compression. This cycle was repeated until the 12$^{th.}$ set of oscillations had been completed, after whose equilibration (180 s), the next compression comprised of drop area reducing from 20.95 mm^2 to 19.8 mm^2 in order to ensure a 1 mN min $^{-1}$ in the surface pressure. The same cycle was repeated for a total of 5 times until a drop area of 15.23 mm^2 was achieved.

For the CO:GT:FFA:PC 40:25:15:20 (quaternary mixture), the initial compression changed the area of the drop from 40 mm^2 to 38 mm^2, followed by an equilibration time of 300 s, oscillations with the same parameters as previous programs and an equilibration time of 180 s. Next, the program entered its second stage where a change in the slope of the isotherm necessitated a change in the drop area reduction size, thus the drop area was reduced from 38 mm^2 to 36.1 mm^2, followed by equilibration time (300 s), oscillations of the same parameters and equilibration time (180 s). This cycle was repeated for a total of 12 times, until at last the area of the drop reached 15.2 mm^2 and the rheology measurements were complete, providing the dilational surface

elasticity and viscosity of the film. For each system at least 4 separate measurements were obtained.

2.4. Results & Discussion

2.4.1. Preliminary Analysis of Individual Components of TFLL Model Membranes: Surface Activity & Morphology

The surface activity and morphology of the films of individual components of the TFLL model membranes were studied on PBS as the subphase at 22 °C. Figure 2.1. depicts the compression isotherms of these individual components. The cholesteryl oleate, glyceryl trioleate and the free fatty acid mixture or FFA (palmitic acid:stearic acid 50:50) serve as representatives of the non-polar components of TFLL and Egg PC represents amphiphilic components which reside at the interface between the aqueous layer and the non-polar TFLL. As shown in Figure 2.1., the egg PC film s starts to exhibit an increase in its surface pressure at an area of ~ 98 $Å^2$molecule^{-1}, after which a continuous surface pressure increase is observed, indicative of the film remaining in a liquid expanded (LE) phase, until at last it reaches the area of ~25 $Å^2$ molecule^{-1} where it collapses at a surface pressure of ~ 38 mNm^{-1}. After the collapse, the film shows no discernible surface pressure increase. This behaviour of the egg PC film is in agreement with the fluidity of lipid films with unsaturated acyl chains studied previously as egg PC is a mixture of phospholipids with a fatty acid distribution that contains > 53% unsaturated acyl chains [54,154,155].

The FFA mixture isotherm shows the highest surface activity of all the individual components with a phase transition from tilted to untilted condensed phase at the pressure of ~20 mNm^{-1}, and the film showing collapse at 53 mNm^{-1}. The observed behaviour of FFAs film is corroborated by previous work [156,157]. From the individual components, cholesteryl oleate and glyceryl trioleate show the lowest surface activity as far as their isotherms are concerned. However, both display unique film morphology and surface behaviour shown in Figures 2.2 and 2.3 respectively.

The cholesteryl oleate isotherm shows a phase transition at ~6 mNm^{-1}. BAM images of cholesteryl oleate are shown in Figure 2.2. Interestingly, for a molecule that has a unit of unsaturation in its acyl chain and might be considered to form a fairly fluid film [155], evidence of condensed phase is observed quite early on in the progression of the isotherm at surface

pressures as low as 0.5 mNm^{-1} (image not shown). This condensed phase coexists with darker holes which are presumed to be either liquid expanded or gaseous phase. GIXD results corroborate the existence of condensed phase even at low surface pressures, as diffraction peaks were observed on the CO film at 3 mNm^{-1}, results of which will be discussed in more detail in Chapter 3 of this thesis. The holes vary in size as the pressure increases. As the film enters the phase transition at an approximate pressure of 6 mNm^{-1}, two key morphological changes emerge: The first is the appearance of small, bright islands emerging within the larger holes, the second is that upon enhancement of the images, another phase with intermediate grey level is evident (Appendix A, Figure A2, red arrow).

Multilayered structures have been proposed for both saturated and unsaturated chain cholesteryl esters [61,158,159]. Thus the areas showing different, but regular levels of brightness (i.e. thickness) may be attributable to multilayering of the film on top of an underlying monolayer as the film compresses. The multilayering is especially noticeable at higher pressures with the emergence of much thicker multilayers on top of the initial condensed phase, which increase in size and surface coverage. Eventually after the pressure of 12 mNm^{-1} (molecular areas < 10 Å^2 molecule^{-1}), the circular domains become much larger and at least three distinct brightness levels and very few residual holes are observed. Similarly, cholesteryl nervonate films exhibited additional multilayers forming on top of the previous ones, wherein the surface homogeneity of the film reduces and thicker multilayers are formed locally [61]. The increase in the proportion of crystalline structures with pressure is corroborated with GIXD data (data not shown) as an increase in peak intensity was observed with increasing pressure. This multilayering behaviour is in agreement with the most widely suggested structure of the non-polar, outermost layer of TFLL [1,7,8,42,49].
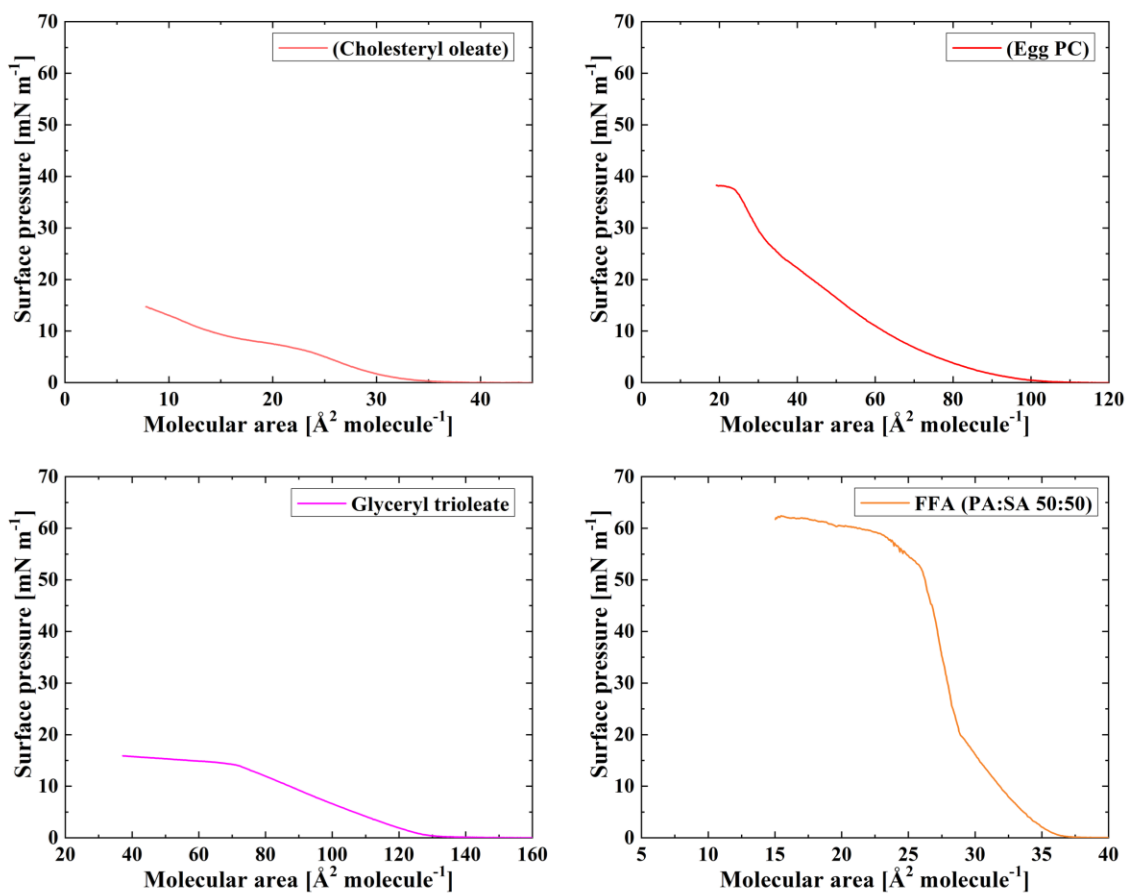
Figure 2.3. Isotherms of cholesteryl oleate (top, left), egg PC (top, right), glyceryl trioleate (bottom, left), and free fatty acid mixture (palmitic acid:stearic acid 50:50) (bottom, right) on PBS at 22 °C.
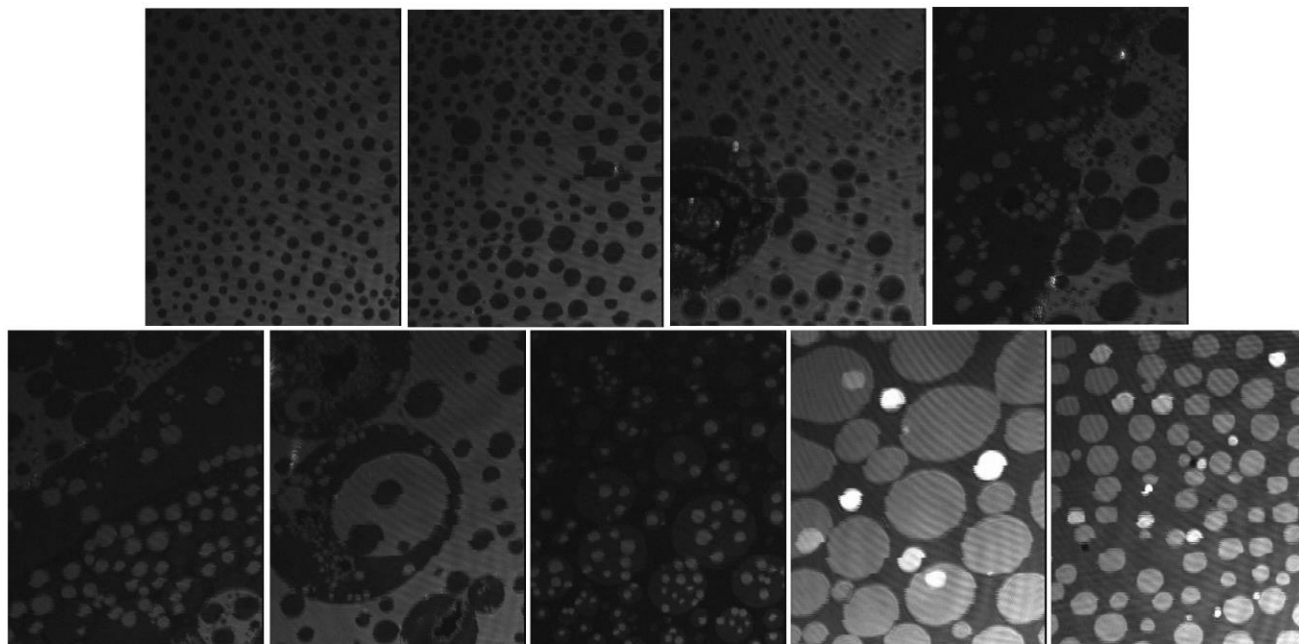
Figure 2.4. BAM images (220 µm wide) of cholesteryl oleate film at surface pressures (top, left to right): 2 mNm⁻¹, 5 mNm⁻¹, 7 mNm⁻¹, 9 mNm⁻¹, (bottom, left to right): 10 mNm⁻¹, 11 mNm⁻¹, 12 mNm⁻¹, 13 mNm⁻¹ and 14 mNm⁻¹ on PBS at 22 °C.

The glyceryl trioleate film isotherm shows an increase in the surface pressure at ~ 128 Å^2 molecule^{-1}. The film remains in a continuous LE phase until 70 Å^2 molecule^{-1} (15 mNm^{-1}), after which the surface pressure remains essentially stable. This has been attributed to an expulsion of glyceryl trioleate (termed an envelope transition) from the monolayer to form a bulk phase [160]. The morphology of the film shown in BAM images of Figure 2.3 shows that the film remains homogeneous until the envelope point with no discernible GT aggregates. After the envelope point, this bulk phase is visible in the form of bright domains that are consistent in their diameter. These domains were previously attributed by Olyńskaż et al. 2020 [12] to three dimensional aggregates of GT instead of forming a homogenous multilayered structure. Olyńskaż et al. 2020 [12] also observed a similar morphology using florescence imaging where evidence of the three-dimensional aggregates of glyceryl trioleate bulk phase was found by analysing the signal intensity. However, unlike the morphology observed by Olyńskaż et al., 2020 [12], the results in this work show a consistent size in these aggregates.
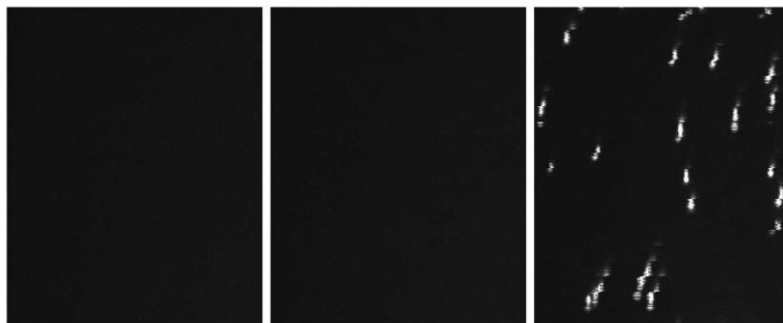
Figure 2.5. BAM images (220 μm wide) of glyceryl trioleate film at surface pressures 7 mNm^{-1}, 13 mNm^{-1} and 15 mNm^{-1} on PBS at 22 °C.

2.4.2. Surface Activity & Morphology of TFLL Model Membranes

Figure 2.6 shows the isotherms of the TFLL model membranes studied in this work along with the isotherms of the individual components comprising each mixture. The binary mixture CO: PC 90:10 is the simplest physiologically representative TFLL mixture in this work with CO representing the non-polar cholesteryl esters and PC representing the polar lipid interface between the aqueous and non-polar part of TFLL. The CO:PC 90:10 mixture isotherm shows a slight expansion to larger molecular areas compared with that observed for the CO isotherm (Figure 2.1) which can be expected given that only 10% PC is present in this mixture. A previous report by Xu et al., 2022 [54] of a film with a similar composition i.e. similar total non-polar to polar lipid ratio where both CO and PC were also used, showed significantly higher surface activity for the mixed film, i.e. reaching surface pressures as high as 45 mNm^{-1} which they attributed to PC driving the surface activity of the film. This is unusual given the low proportion of the amphiphilic components and their isotherms indicating a high deviation from ideality which will be discussed later. In the current system, the film shows only a slight increase in its surface activity compared with CO film, commensurate with its dominant component i.e. CO at 90%.

The binary mixture shows a similar morphology including a coexistence of condensed phase with what appears to be gaseous phase at very low pressures as observed for CO film (Figure2.5). Yoshida et al. 2019 [161] reported a spontaneous formation of thicker regions comprising cholesteryl esters and wax esters at ultra low pressures coexisting with a polar monolayer phase on extracted rabbit meibum films. The binary mixture also shows a similar

38

morphological progression as CO with a few notable differences. We observe the formation of domains within the holes at lower surface pressures well below the phase transition plateau (Figure 2.5, 2 mNm^{-1}). Similar holes were observed with a mixture of cholesteryl nervonate (CN):POPC 90:10 wherein it was suggested that the ester groups of the cholesteryl ester molecules are facing the buffer interface [61]. As the pressure increases and the phase transition occurs (at ~7 mNm^{-1}) it is evident that at a comparable pressure (9 mNm^{-1}), the binary mixture is more continuous with fewer holes compared with the pure CO film. This indicates that the polar PC molecules initially contribute to the formation of a more coherent underlying film.

The emergence of multilayers in the form of thicker circular domains also occurs at a lower surface pressure (10 mNm^{-1}) compared with CO (12 mNm^{-1}). At higher surface pressures (11 mNm^{-1} and onwards) we can observe the coexistence of multilayer domains with at least two different brightness levels parallel with the multilayering observed with CO. It appears that the addition of the polar lipids induces earlier phase transitions at all stages. Additionally, from 11 mNm^{-1} onwards, dark areas of the monolayer underneath the CO multilayers begin to reappear and increase in surface coverage and number with pressure. This indicates that as the pressure increases and as the PC acyl chains in the underlying monolayer become more close-packed, the PC-PC and CO-CO interactions dominate over the interdigitation interactions between PC and CO which Paananen et al., 2020 [61] have suggested as the cause of the less homogeneous multilayering. So, the overlying CO multilayer domains begin to get further expelled from the film and form additional levels of multilayers, resulting in local, circular multilayer domains which lack their initial surface homogeneity observed at lower pressures.
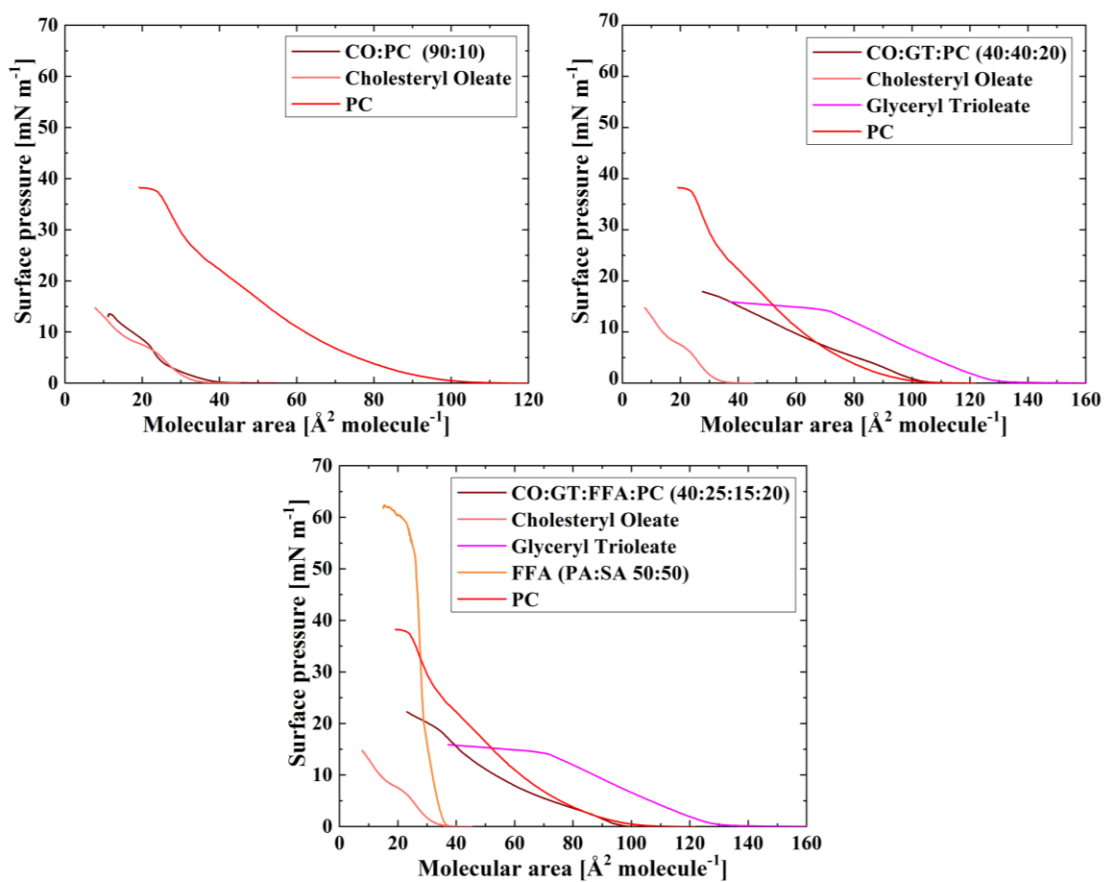
Figure 2.6. Isotherms of CO:PC (binary mixture) (top, left), CO:GT:PC (ternary mixture) (top, right) and CO:GT:FFA:PC (quaternary mixture) (bottom) on PBS at 22 °C.
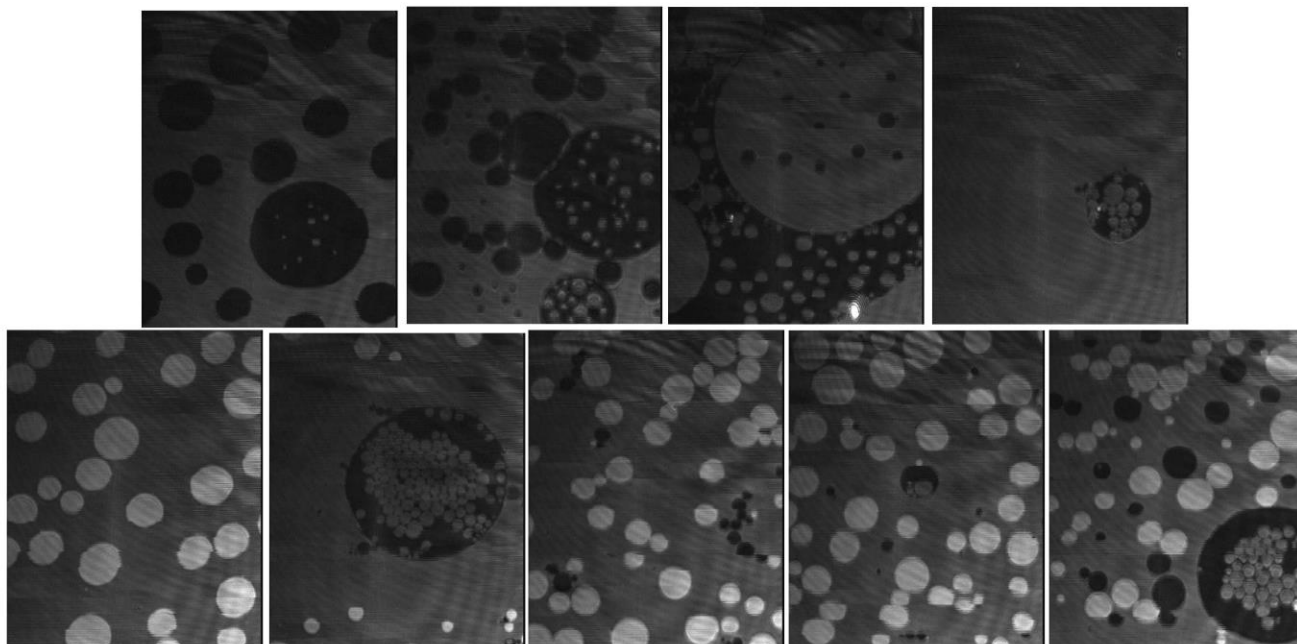
Figure 2.7. BAM images (220 μm wide) of CO:PC 90:10 (binary mixture) film at surface pressures (top, left to right): 2 mNm⁻¹, 5 mNm⁻¹, 7 mNm⁻¹, 9 mNm⁻¹, (bottom, left to right): 10 mNm⁻¹, 11 mNm⁻¹, 12 mNm⁻¹, 13 mNm⁻¹ and 14 mNm⁻¹ on PBS at 22 °C.

The CO:GT:PC 40:40:20 (ternary) mixture isotherm shows an expansion to higher molecular areas due to higher proportions of GT and PC, the latter also leading to a higher surface activity of the film. Two phase transitions are also observed, one at 6 mNm⁻¹ and another at 16 mNm⁻¹. Comparison of the isotherm (Figure 2.4) and BAM images (Figure 2.6) with those of the individual components (Figures 2.2 and 2.3) indicates that the first phase transition is commensurate with the initial transition in the CO isotherm while, the second phase transition is commensurate with the envelope transition point observed in the GT isotherm, the latter similar to results reported for GT films [12,160].

In the pressures below the first phase transition, the film is homogenous. At the surface pressure of 6 mNm⁻¹ the CO domains appear and are smaller in size compared to both the pure CO and the binary mixture films. Moreover, the circular domains do not exhibit the same growth pattern, that is, they do not coalesce, nor are domains of differing brightness levels i.e. thickness observed. This may be due to the smaller percentage of CO in the ternary mixture. However as the surface pressure of the film increases, the condensed phase domains of CO increase in both number and size (up to approximately 15-20 μm) indicating the increase of the overall CO

condensed phase surface coverage. Notably upon further compression of the film, only one distinct grey-level is observed for the CO domains, suggesting that the surface pressure at which CO multilayering occurs has been shifted in the ternary mixture, increasing to a point unreachable by the Langmuir trough used in this work. This is likely due to the added fluidity of the film by increase in PC and GT contents. Overall, the addition of GT to the film and the reduction of CO percentage in the film, appears to have added to the fluidity of the film as the dark LE phase covers a large surface area throughout the compression. Moreover, the lack of CO multilayered domains is indicative that the interaction with the lipids hinders the formation of interdigitated CO multilayers as described for the binary mixture. After the second transition of the film, commensurate with the envelope transition of GT at the pressure of 16 mNm^{-1} the BAM images show an emergence of the bright isolated three-dimensional aggregates of GT bulk phase with the same consistent size, coexisting with the already growing CO condensed phase domains [160].
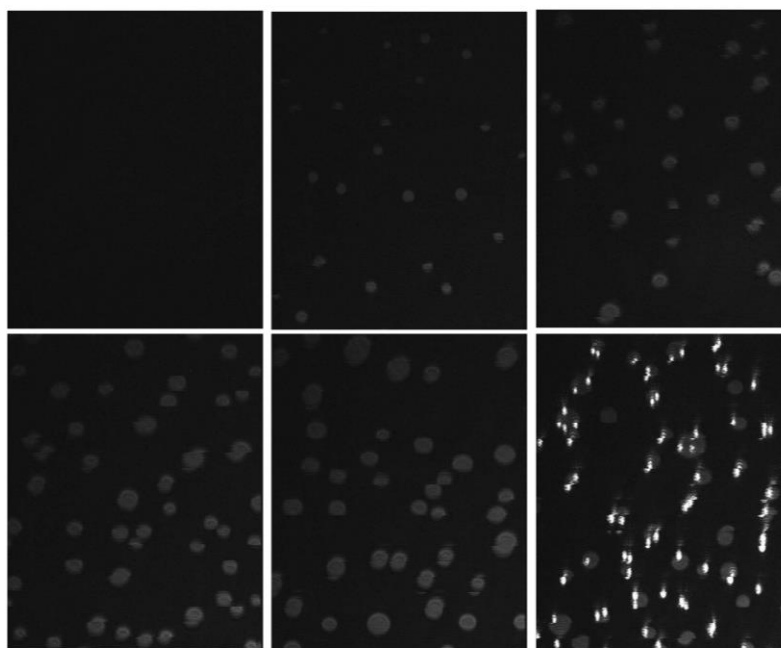
Figure 2.8. BAM images (220 µm wide) of CO:GT:PC 40:40:20 (ternary mixture) film at surface pressures (top, left to right): 2 mNm^{-1}, 7 mNm^{-1}, 11 mNm^{-1}, (bottom, left to right): 13 mNm^{-1}, 15 mNm^{-1} and 17 mNm^{-1} on PBS at 22 °C.

The CO:GT:FFA:PC 40:25:15:20 (quaternary) mixture isotherm also shows two phase transitions. The first phase transition, associated with the condensation of CO, occurs at a slightly smaller pressure compared with the same change in the ternary and binary films. The film shows an overall higher surface activity compared with the previous films, attributable to the addition of highly surface active FFA component., where these saturated FFAs are known to form condensed phases at all surface pressures above 0 mN m^{-1}. It has been previously studied that FFAs can easily be incorporated into the model membrane films of similar composition without an impact on the stability of the film due to their small headgroups [16].

The quaternary mixture film morphology is shown in Figure 2.7. The CO condensed phase domains begin to be visible at 4 mNm^{-1}. Although the film remains dominated by a continuous LE phase coexisting with these domains, they again increase in size and number with film compression. On the other hand, the surface pressure for the second phase transition of the quaternary mixture, which is associated with the GT expulsion (envelope transition), occurs at a higher pressure (20 mNm-1) than the ternary mixture (16 mNm^{-1}), although the morphology is similar. The interaction of the more surface active FFA with the GT molecules anchors the GT plane of the monolayer, driving the GT envelope transition to a higher surface pressure.

It is worth noting that the envelop transition coincides with the phase transition of FFAs film from a tilted to an untitled condensed phase (~ 20 mNm^{-}1). While not conclusive, this transition to a more highly packed monolayer could induce the expulsion of the GT. Similar to the ternary mixture, there is no evidence of CO multilayering on top the underlying monolayer, only the coexistence of CO condensed phase domains with the bright aggregates of GT at higher pressures after the second phase transition.
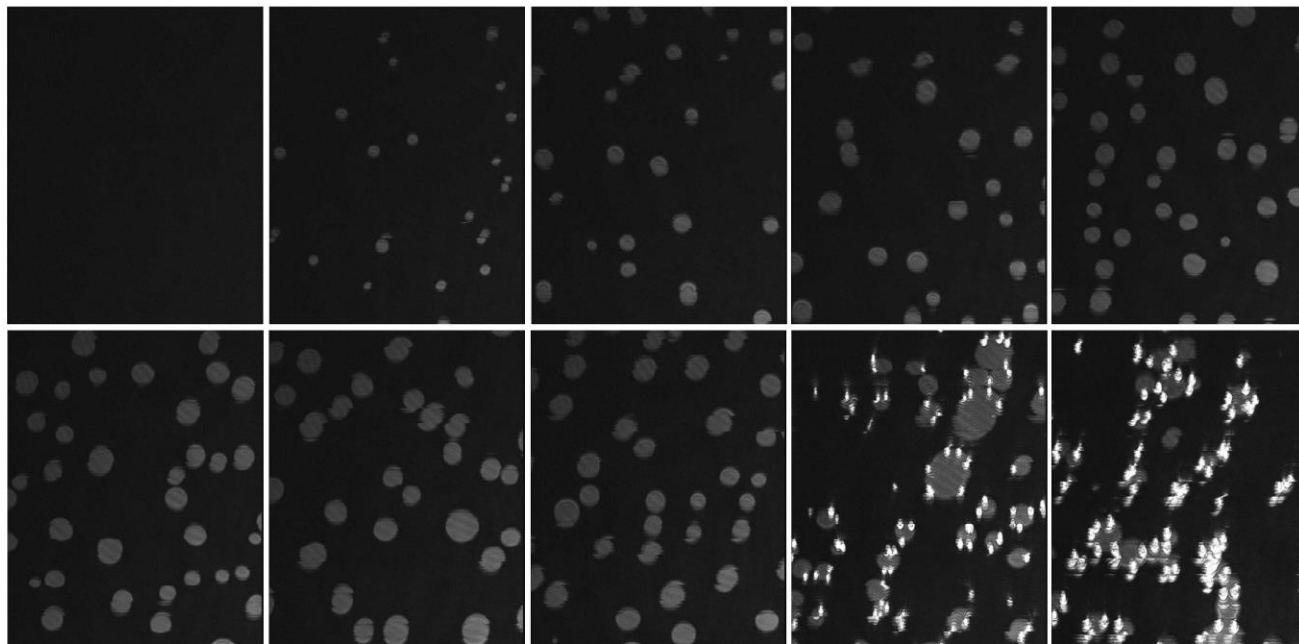
Figure 2.9. BAM images (220 nm wide) of CO:GT:FFA:PC 40:25:15:20 (quaternary mixture) film at surface pressures (top, left to right): 2 mNm^{-1}, 5 mNm^{-1}, 7 mNm^{-1}, 9 mNm^{-1}, 11 mNm^{-1}, (bottom, left to right): 13 mNm^{-1}, 16 mNm^{-1}, 18 mNm^{-1}, 20 mNm^{-1}, 22 mNm^{-1} on PBS at 22 °C.

Figure 2.8 directly compares the isotherms of the three TFLL models studied in this work. The phase transitions associated with CO and GT are conserved in the mixed films. For the CO condensation, the surface pressure of the phase transition is lowered in the case of the model membranes, in particular in the more complex ternary and quaternary mixtures. There is also an increase in the surface activity of the films as this progression in complexity of the film composition occurs. The binary mixture appears to be the least surface-active film with only 10% PC in its composition. However, the ternary and quaternary mixtures, both show higher surface activity. In the ternary mixture, the envelope pressure of GT, discussed previously by Mitsche et al., 2010 [160], has increased compared to GT film and it shows a more fluid like state over a greater range of pressures due to a higher PC %. The same behaviour is also observed in the quaternary mixture, showing the highest surface activity among the three films as well as a higher GT envelope pressure (20 mNm^{-1}). This is due to the impact of FFAs in the film composition, having been incorporated into the film and their phase transition into untilted condensed phase increasing the GT envelope transition pressure.
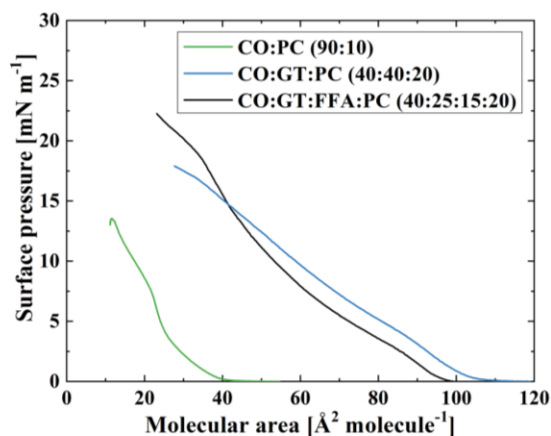
Figure 2.10. Comparison of isotherms of CO:PC 90:10 (binary mixture), CO:GT:PC 40:40:20 (ternary mixture) and CO:GT:FFA:PC 40:25:15:20 (quaternary mixture) on PBS at 22 °C.

To better understand the non-ideal behaviour of the three TFLL films, an additional area analysis was performed at five different surface pressures, i.e. the mixture area was compared to that expected for an ideal mixture based on the isotherms of the individual components (Figure 2.9). The relative experimental area of the binary mixture film shows a reduction in area compared to the calculated (ideal mixture) area which at its highest is at 20%. This is possibly due to the impact of PC on the film. As previously discussed, in the binary mixture, with increasing pressure, the CO molecules begin to get expelled from the film and form multilayers on top. The multilayering of CO occurred at a smaller pressure in the binary mixture compared with CO (Figures 2.2 & 2.5), meaning that at a smaller pressure, the film molecules started to be expelled form the monolayer and form multilayers. The calculation assumes all molecules reside in the plane of the film and thus smaller average molecular area reflects the expulsion of molecules out of this plane at lower surface pressures. Both the ternary and quaternary mixtures also exhibit non-ideal behaviour, however in these cases a notable expansion of the film is observed and the deviation from an ideal mixture decreases as the surface pressure increases. Given that both films have a reduced percentage of CO in their compositions (40% rather than 90%) compared with the binary mixture, and no evidence of CO multilayering was observed, it can be deduced that the increased average molecular area reflects the retention of CO molecules in the plane of the monolayer and the increased proportion of LE phase. This effect is amplified in the quaternary mixture with the addition of the surface active FFAs.
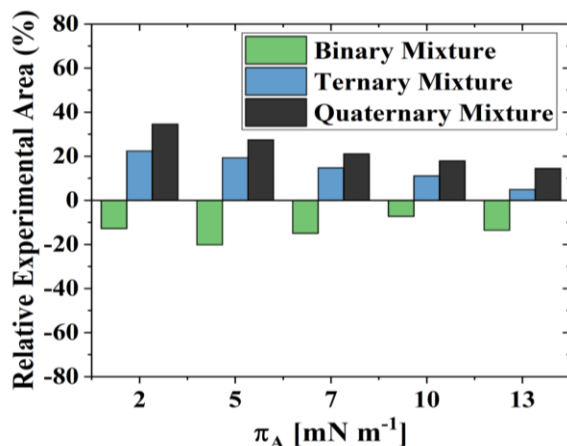
Figure 2.11. Analysis of non ideal behaviour of CO:PC 90:10 (binary mixture), CO:GT:PC 40:40:20 (ternary mixture) and CO:GT:FFA:PC 40:25:15:20 (quaternary mixture) on PBS at 22 °C.

2.4.3. Compression-Expansion Cycles of TFLL Model Membranes

Figure 2.10 depicts the compression-expansion cycles of the model TFLL films. Although the compression-expansion rate used (196 cm^2 min^{-1}, equivalent to 1.5 min/complete cycle) is slower than the average blinking rate of 10 blinks per minute [153], the films were compressed and expanded with the highest speed achievable by the Langmuir trough used, in order to mimic the blinking cycle. The Figure 2.10 insets show the change in relative area at 10 mN m^{-1} (taken as a representative pressure) as a function of cycle number. The relative area is the film area expressed relative to the initial molecular area of the first cycle at 2 mN m^{-1}. The hysteresis observed in the initial cycle which is apparent for all mixtures is typical to such compression-expansion cycles. The first cycle serves as a priming cycle after which a memory effect is observed.

The cycles of the binary mixture show an overall impressive respreadability and very little material loss as the number of cycles progresses, suggesting the reversibility of the formation of the CO multilayers atop of the underlying monolayer as the film goes through expansion. PC films also show this reversibility, if collapse has not been reached [160] which may have likely reenforced this behaviour in the mixed film. Respreadability and reversibility is a key

characteristic of TFLL [7,9] and even the binary mixture displays this key property with similarity to previously reported results for extracted meibum films [49,55,161,162].

There is a slight expansion of the binary film with each cycle at low surface pressures, i.e. below the first phase transition, after which all the cycles show a high respreadability and reproducibility in both compression and expansion segments of the cycles. This expansion leads to an overall increase in the hysteresis (difference between compression and expansion cycles) with increasing cycle number. As explained by Yoshida et al., 2019 [161], hysteresis occurs when the rate of the respreading of the film is slower than the increase in the area when undergoing expansion. In this case, the hysteresis is associated with the reversal of the CO multilayering. The consequence of this is that at each cycle the film exhibits higher surface pressures for the same molecular area than the previous cycle. This also leads to a higher surface pressure as the film undergoes compression, than it did in the previous cycle. Given the observed reproducibility above the phase transition which marks the beginning of multilayering, it can be assumed that the film multilayering adds to the overall stability of the film.

The ternary mixture also shows an impressive respreadability upon compression-expansion which is observed especially after the second phase transition of the film which is commensurate with the envelope transition point of GT. Interestingly, before this phase transition, i.e. the initial transition commensurate with that of CO where the film appears to remain in a mainly LE phase, less respreadablity is observed as the cycles progress. As shown in the inset, the cycle hysteresis is reduced as the cycles progress, an indication of the increased stability of the film due to the envelope transition of the GT within the film and the apparently reversible exclusion of GT molecules from the underlying monolayer into three-dimensional aggregates and creating a GT bulk phase [12,160].

The quaternary mixture is the least re-spreadable film and shows area shifts with each cycle. However, the inset indicates that as the cycles progress, the hysteresis is reduced. It is worth noting that unlike the binary mixture, both ternary and quaternary mixtures show a reduction in the area as the cycles progress. This may be due to some molecules not completely returning to the film upon each expansion which in turn, reduces the molecular area and leads to the observed phenomenon.

It has been reported that films comprised of lipid molecules with saturated acyl chains tend to lack respreadability compared with those comprised of lipids with unsaturated acyl chains [7,49,55]. Moreover, It has been previously observed in simulations of lung surfactants that the addition of unsaturated chained lipids to films otherwise comprised of saturated chained lipids improves the overall respreading behaviour of the film [163–166]. Therefore, the reduced respreadability of the quaternary mixture can be directly linked to the addition of FFAs with saturated acyl chains and the impact of other components of the film with unsaturated acyl chains i.e. CO, GT and > 53% of PC fatty acid distribution by reduction of the impact of FFAs on the re-spreading behaviour of the film. Overall, among all three models, the ternary mixture shows the highest stability, the lowest hysteresis, and the greatest similarity to extracted meibum lipid films. Thus, although FFAs are components of the TFLL, it appears that strong attention must be paid to the proportion of FFAs in TFLL model membranes [16].
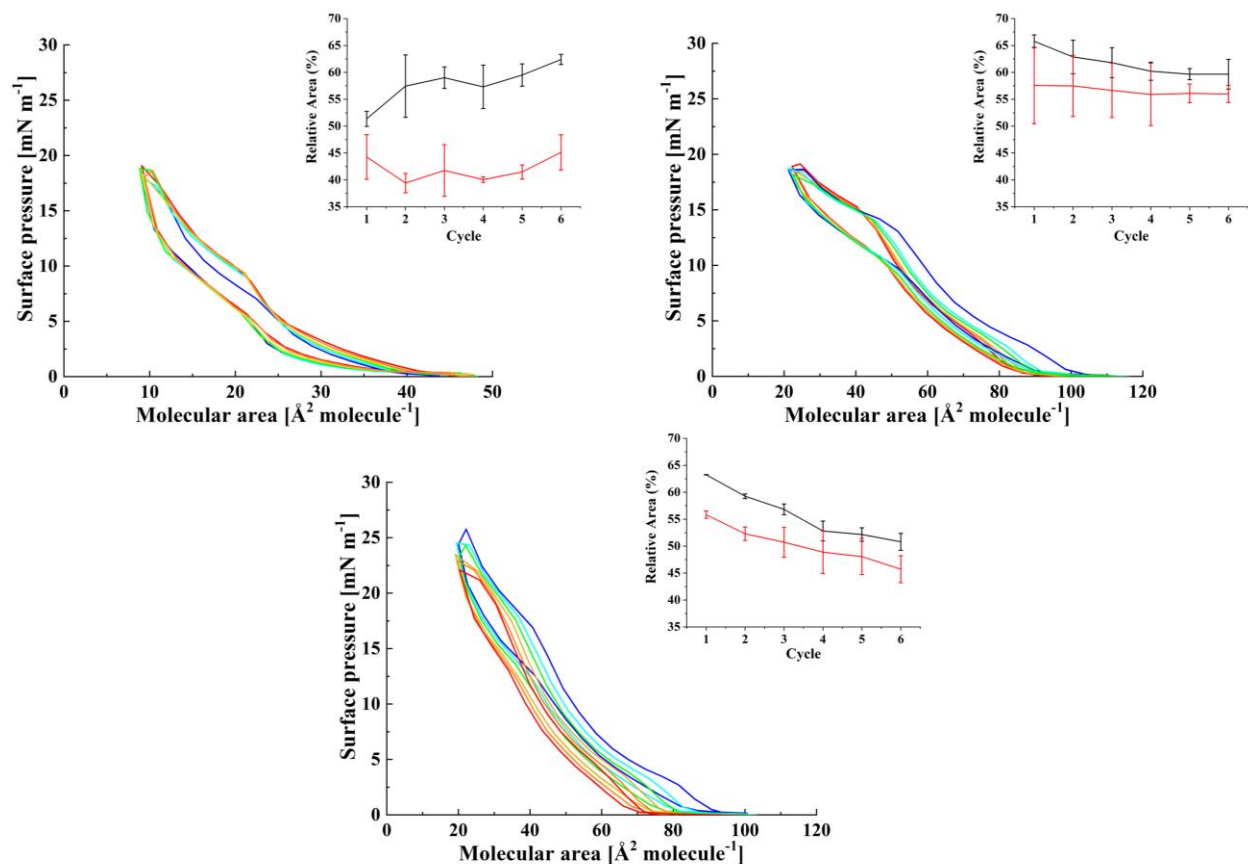
Figure 2.12. Compression-expansion cycles of CO:PC 90:10 (binary mixture, top, left), CO:GT:PC 40:40:20 (ternary mixture, top, right) and CO:GT:FFA:PC 40:25:15:20 (quaternary mixture, bottom) on PBS at 22 °C. The insets represent the relative area at 10 mNm^{-1} of the compression (black) and expansion (red) as a function of the number of cycles. The data points and error bars represent the mean and standard deviation of at least three independent cycling experiments. Cycle 1 blue, cycle 2 cyan, cycle 3 green, cycle 4 yellow, cycle 5 orange, cycle 6 red.

2.4.4. Rheology Measurements of TFLL Model Membranes

Figures 2.11 and 2.12 show the results of rheology measurements of the three TFLL model membranes. Detailed description of the methodology and the programs used in these experiments can be found in section 2.3. The films were oscillated at a frequency comparable with the frequency of blinking in normal subjects as reported in the literature [153]. Previous reports for extracted meibum as well as TFLL model membranes, employed a frequency sweep [47,48,54,162]. Herein, by oscillating the films at a blinking comparable frequency (0.16 Hz) which is possible with the Profile Analysis Tensiometer (but not with common Langmuir troughs),

physiologically relevant results are obtained. Moreover, the frequency used is well below the maximum limit of oscillation frequency in drop tensiometry i.e. (< 1 Hz) [135] and ensures no deviation from the Laplacian drop shape [135].

It can be immediately observed that all three films show a moderate elasticity and ultra low viscosity at the oscillating frequency of blinking at each given pressure. This is in agreement with previous reports of the viscoelastic behaviour of extracted meibomian lipids [47,48,162] at similar experimental parameters i.e. temperature & frequency. Although experimental conditions such as temperature in the TFLL membrane work by Xu et al., 2022 [54] are different from this work, i.e. the pressure at which the data was reported by their recombinant film (compositionally comparable with this work) is only achievable by the quaternary mixture (20 mNm^{-1}), they nonetheless also reported a highly elastic rather than a viscous film. Moreover, at the comparable frequency of 0.1 Hz their recombinant film shows similar ranges of elasticity and viscosity i.e. <40 mNm^{-1} and <10 mNm^{-1} [i] respectively compared with the maximums reported here (at the lowest molecular area i.e. highest surface pressure achieved by each TFLL film).

The dilational elasticities (~40-45 mNm^{-1}) and viscosities (~ 3-7 sec mNm^{-1}) reached by each film at surface pressures of 13-18 mNm^{-1} are comparable with those reached by extracted human meibomian lipids under similar experimental parameters i.e. temperature (20 °C) and frequency (1 rads^{-1} or 0.159 Hz) [47]. The differences are minimal considering the range of values typically reported for lipid films [95]. Thus the model membranes share similar dilational rheology characteristics with extracted meibum films, which may be attributable to the high non-polar to polar lipid ratio, rather than the presence of any one specific component [47,48,162]. It also lends support to the use of artificial model membranes to represent TFLL.

In general, all three mixtures show an increase in their elasticity as the film compresses to smaller molecular areas. As for the same increase in viscosity upon compression, it is mostly observed for the quaternary mixture and to a much smaller extent the binary mixture. In the latter, this occurs at molecular areas commensurate with where multilayering is observed i.e. 17

---

[i] The unit of viscosity used by Xu et al. 2022 [54] is mNm^{-1} rather than sec mNm^{-1}, thus, it is assumed in this work that the reported viscosity values were measured in 1 s to warrant the change in the unit.

Å^2 molecule^{-1} and smaller. Among the three films, the binary mixture film experiences higher standard deviations in both dilational elasticity and viscosity (Figures 2.11 and 2.12), especially as the film reaches smaller molecular areas i.e. at 27 Å^2 molecule^{-1} and lower. This is likely due to the aforementioned multilayering which can impact the response of the film to oscillations, especially when high hysteresis is observed. Predictably, this behaviour is observed in neither the dilational elasticity nor viscosity data of the ternary and quaternary mixtures, implying that the lack of multilayering, or rather the shift of the multilayering transition to surface pressures not achievable by the profile analysis tensiometer has generated more reproducible films. It is also worth noting that an increase is observed in the maximum elasticity and viscosity reached by the quaternary mixture compared with the ternary and the binary mixtures. This behaviour has been attributed to the addition of lipids with saturated acyl chains, reducing the fluidity of the overall film [131] which was observed with these films.
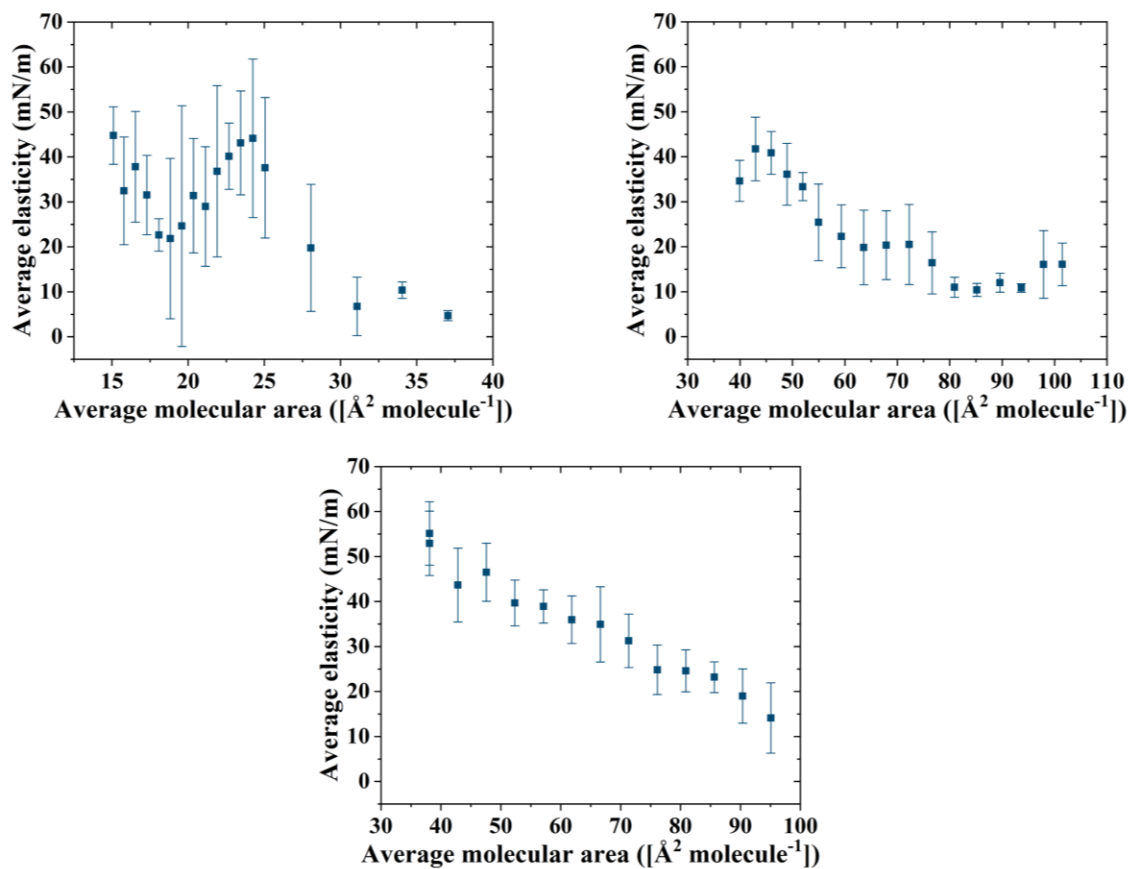
Figure 2.13. Surface dilational elasticity data of CO:PC 90:10 (binary mixture, top, left), CO:GT:PC 40:40:20 (ternary mixture, top, right) and CO:GT:FFA:PC 40:25:15:20 (quaternary mixture, bottom) on PBS at 22 °C. The data points and error bars represent the mean and standard deviation of at least four independent measurements.
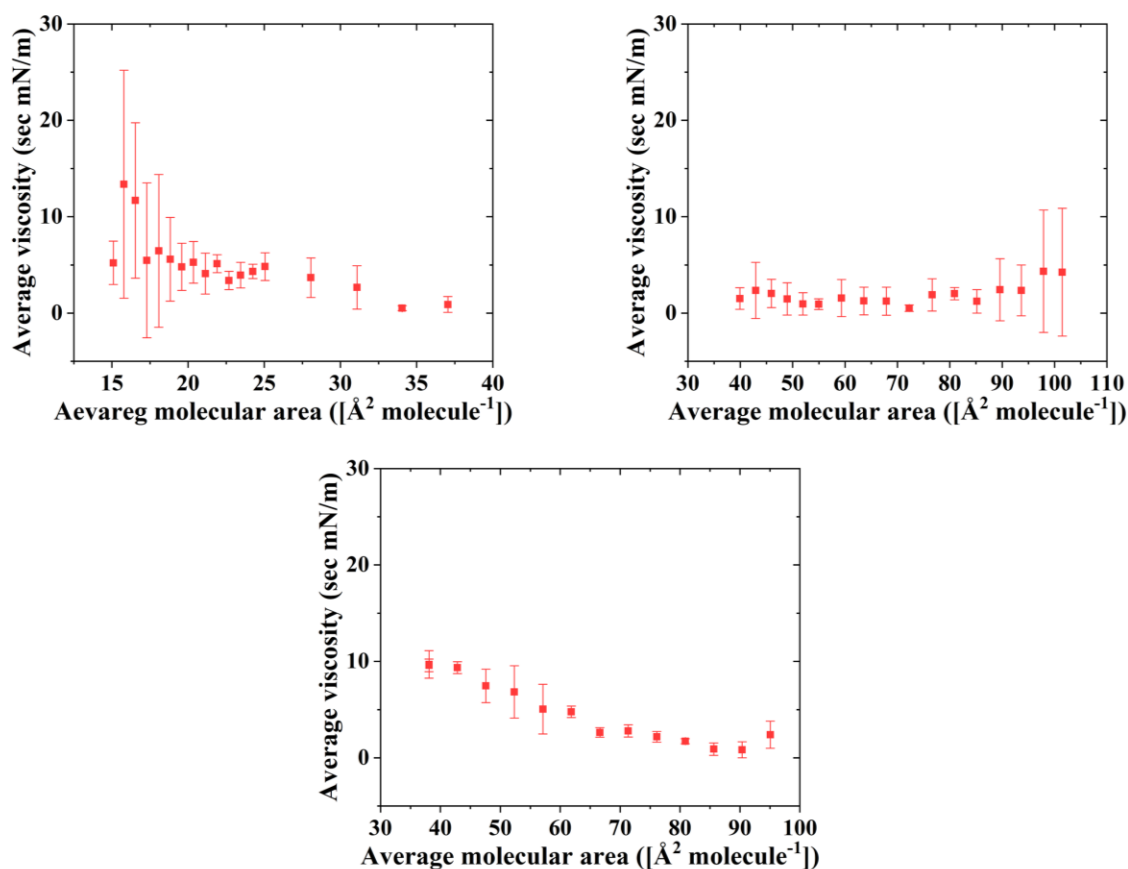
Figure 2.14. Surface dilational viscosity data of CO:PC 90:10 (binary mixture, top, left), CO:GT:PC 40:40:20 (ternary mixture, top, right) and CO:GT:FFA:PC 40:25:15:20 (quaternary mixture, bottom) on PBS at 22 °C. The data points and error bars represent the mean and standard deviation of at least four independent measurements.

2.5. Conclusion

By using a systematic approach of adding components to the TFLL model membranes and progressively creating more complex and more physiologically relevant model membranes, it can be deduced that each of the components in the TFLL model membranes play an independent role commensurate with their own surface behaviour. It was observed that both CO and GT have their own multilayering/envelope transition respectively, to a bulk phase which are retained in the mixtures i.e.there is no clear mixing of the components above their respective phase transition pressures. All the mixtures showed deviation from ideal mixing even at low surface

53

pressures, which appears to be primarily related to changes in the impact of cholesteryl esters on the film. For the binary mixture, a decrease in the molecular area is observed due to increased CO multilayering, whereas the ternary and quaternary films show an expansion, as no multilayering is observed within the molecular areas achievable by the Langmuir trough.

The respreadability is a key characteristic of a TFLL as in physiological conditions, the TFLL undergoes constant compressions and expansions while blinking. Among the mixtures studied in this work, the ternary mixture showed the most respreadable film with the lowest hysteresis within the cycles, indicative that the reversible envelope transition of GT plays a role in increasing the stability of the film as it undergoes compression-expansion cycles.

Overall, the binary mixture, while informing us on the role of polar phospholipids as well as cholesteryl esters of TFLL, does not itself sufficiently represent the properties of physiological meibum lipid film since it appears that the multilayering of CO makes rheological measurements less reproducible, shows a higher hysteresis in cycles experiments and creates non-ideal mixing behaviour. Moreover, the addition of just 10% phospholipid to CO, creating the binary mixture, seemed to induce an early onset of multilayering behaviour of CO in the mixture which may be attributed to the packing of the PC chains. While it is worth noting that physiologically, the cholesteryl ester proportion is lower than 90 % [1,8,11,19,22,28,29], comparison of the results of the binary and ternary mixtures is a useful tool for understanding the role of cholesteryl esters, triglycerides and phospholipids in TFLL. Moreover, the addition of saturated acyl chain FFAs makes the film more viscous than physiological TFLL, leads to reduced respreadability as well as increased non-ideality in the film which indicates the importance of tuning the percentage of FFAs when creating TFLL model membranes. While each of these components have a role to play, the ternary mixture best reproduces the characteristics of physiological TFLL.

It is important to remember that TFLL is a complex lipid mixture wherein each family of lipids play their own significant role in the many functions of TFLL. The results of this work are valuable in shedding light on some of these components' roles which will aid in our understanding of the impact of alterations in the tear film lipid layer composition on its dynamic structure in relation to DED.

Chapter 3. A Biophysical Study of Cholesteryl Oleate Film Crystalline Structure

3.1. Abstract

Cholesteryl esters are an important class of lipids found in the tear film lipid layer (TFLL) which coats the ocular surface, and it is paramount in maintaining the tear film stability while blinking. The crystalline structure of cholesteryl oleate (CO) films, frequently used in TFLL model membrane studies, were investigated using Langmuir balance and Brewster Angle Microscopy (BAM) to determine the surface activity and the morphology of the CO film, respectively. The lateral structure and ordering of the film were investigated using Grazing Incidence X-Ray Diffraction (GIXD). X-ray reflectivity (XR) and Grazing Incidence Off-Specular Scattering (GIXOS) were used to study the vertical structure of the CO film. BAM images revealed evidence of multilayer formation at higher surface pressures. The crystallinity of the CO film was determined to be the result of the cholesterol ring packing only and not the interdigitation of the CO unsaturated acyl chains. At lower surface pressures, CO forms a monolayer film with multilayers forming only above the CO phase transition observed. This is in contrast to saturated chain cholesteryl esters previously reported to form ordered interdigitated bilayers.

3.2. Introduction

Cholesteryl esters are one of the multiple lipid families comprising the complex and multicomponent human tear film lipid layer (TFLL) which is the outermost layer of the human tear film, covering the aqueous tear film and in direct contact with the environment [1,6]. TFLL is responsible for a number of important roles as it is capable of reducing the surface tension of the tear film while blinking due to its distinct surface properties [1,6]. The tear film must respread upon each blink, for which a stable tear film is needed and TFLL maintains this stability.

It has been suggested previously that TFLL has a multilayered structure at the air-tear interface [16–18]. The human TFLL composition is reasonably well represented by meibomian gland secretions (MGS), secreted by the meibomian glands located within the eyelids [8,19]. More than 90% of the entire TFLL composition is made up of non-polar lipids and the rest is composed of polar lipids [1,8,11,28]. The most widespread suggestion for the structure of TFLL is typically a

55

duplex film wherein a monolayer of polar lipids exists at the interface of aqueous tear film and TFLL, which facilitates the interaction of the highly hydrophobic layer on top of it which is composed of non-polar lipids, mainly cholesteryl esters and wax esters for which a multilayered structure has been previously suggested [1,3,7,8,16–18,24,34,41].

In order to understand the composition-structure-function relationship of TFLL, the study of TFLL model membranes has been a subject of interest in the literature for years. Model membrane studies focus on the biophysical investigation of mixtures composed of representative lipids with an emphasis on surface activity, morphology and rheology of these model membranes [16,17,52,53,57,58]. Many of the TFLL model membranes previously studied, contain a cholesteryl ester representative of the long acyl chain Cholesteryl esters (CEs) which constitute 30-45 mol% of human TFLL [1,8,11,19,22,28,29], in order to be physiologically relevant.

Cholesteryl oleate (CO) is a cholesteryl ester which has been used as a representative and common TFLL cholesteryl ester in model membranes for many years [16,17,52,53,57,58]. Despite this, while there are previous reports on several other cholesteryl esters, namely, cholesteryl tridecanoate, cholesteryl palmitate, and cholesteryl stearate [159], little research has focused on the biophysical properties of the cholesteryl oleate film, itself.

The current communication focuses on the biophysical properties of the cholesteryl oleate film. Langmuir balance and Brewster Angle Microscopy (BAM) are used to study the surface activity and morphology of the cholesteryl oleate film. Synchrotron-based X-ray surface characterization techniques are used to study the two-dimensional crystalline structure of cholesteryl oleate film. Specifically, Grazing Incidence X-Ray Diffraction (GIXD) was used to gain information on the lateral structure and X-ray reflectivity (XR) and Grazing Incidence Off-Specular Scattering (GIXOS) were used to study the vertical structure of the CO film.
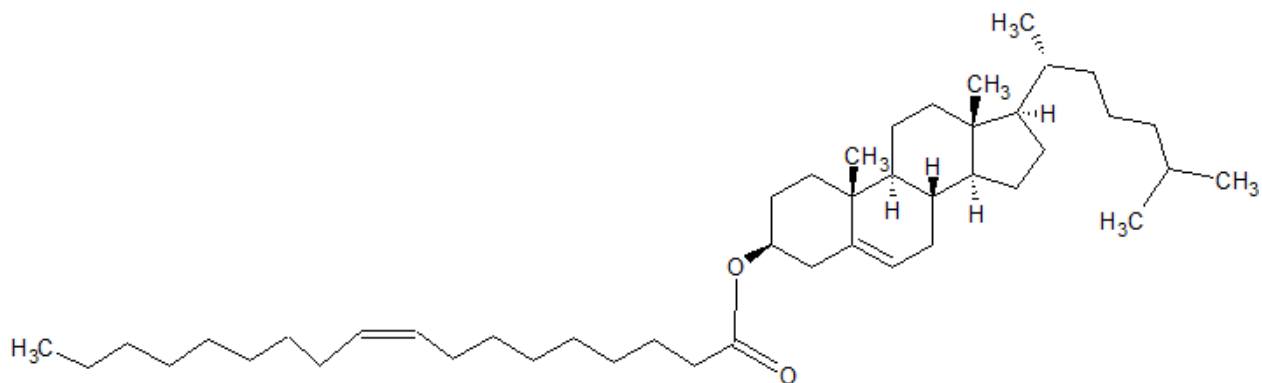
Figure 3.1. Chemical structure of cholesteryl oleate.

3.3. Materials & Methods

Materials. Cholesteryl oleate (CO, > 98%), and phosphate-buffered saline tablets (PBS, pH 7.4, 10 mM phosphate, 137 mM NaCl, 2.7 mM KCl) were purchased from Sigma-Aldrich. The spreading solvent was HPLC grade chloroform purchased from Fisher Scientific.

Preparation of Mixtures, Solutions & Subphases. Solutions of cholesteryl oleate were prepared with an average concentration of up to 1.0 mg mL^{-1} by dissolving the appropriate quantities of cholesteryl oleate in chloroform. Water subphases were comprised of ultrapure water with resistivity of 18.2 MΩ cm^{-1} from a Milli-Q® HX 7080 water purification system (HC). The PBS buffer was prepared by dissolving one phosphate-buffered saline tablet in 200 mL of ultrapure water.

Langmuir Film Balance, Surface Activity. To obtain the surface pressure-molecular area isotherms, Langmuir film balance was used. The cholesteryl oleate solution with concentrations of up to 1.0 mg mL^{-1} was spread at the air-buffer interface on a Langmuir trough (NIMA Technologies). After an equilibration period of 10 minutes for the film and the evaporation of chloroform, the barriers of the Langmuir balance closed at a speed of 5 cm^2 min^{-1} to generate the surface pressure-area isotherms. A wilhelmy plate was used to obtain the surface pressure (π). At least 3 reproducible measurements were performed for each experiment.

Brewster Angle Microscopy, Morphology. A Langmuir film balance from NIMA Technologies was coupled with an I-Elli2000 imaging ellipsometer (I-Elli2000, Nanofilm Technologies) equipped with a 50 mW Nd:YAG laser (λ = 532 nm) to obtain Brewster Angle

Microscopy (BAM) images. CO solutions with concentrations up to 1.0 mg mL^{-1} were spread on a physiologically relevant subphase (PBS buffer). BAM images were obtained during the compression of the film at a speed of 5 cm^2 min^{-1} with a 20X magnification lens, a resolution of 1 μm and an incident angle of 53.15°.

Grazing Incidence X-Ray Diffraction (GIXD) The GIXD experiments were carried out at beamline 15-ID-C ChemMatCARS at the Advanced Photon Source (APS) in Argonne National Laboratory using monochromatic X-rays of energy 10 keV. The following parameters were used for the experiments: X-ray beam wavelength of 1.239 Å, incidence angle of 0.0906°, horizontal size of 20 μm, and vertical size of 120 μm, creating a beam footprint of 20 μm by 7.6 cm. The 2D Swiss Light source PILATUS 100K set to single photon counting mode was used as the detector. Two sets of slits were used in order to minimize the intense low-angle scattering: one situated in front of the detector and the other at 292.0 nm from the sample. A Langmuir balance with the surface area of 340 cm^2 was used for the experiments. The films were spread at the air-buffer interface and following a 20-minute-long equilibration time, they were compressed at a speed of 5 cm^{2}min^{-1} (equivalent to 1.5 Å^{2}molecule^{-1}min^{-1}) using a mobile barrier. The measured GIXD data is plotted as contour plots of the X-ray intensity as a function of both the horizontal (Q_{xy}) and the vertical (Q_z) scattering vector components. The in-plane diffraction data was fit using Lorentzian function to obtain the lattice d spacing (equation 3.1) [141].

$$d = 2\pi/Q_{xy}$$
Equation 3.1. Lattice d spacing.

The full width at half maximum (fwhm) of the Bragg peaks were corrected for the instrumental resolution (0.0084 Å-1) (equation 3.2) [139–141].

$$fwhm_{intrinsic}(Q_{xy}) = [fwhm_{intrinsic}(Q_{xy})^2 - fwhm_{resolution}(Q_{xy})^2]^{1/2}$$
Equation 3.2. Correction for instrumental resolution of the full width at half maximum (fwhm) of the Bragg peaks [139–141].

Using the Scherrer formula, the full width at half maximum (fwhm) of the Bragg peaks was used to calculate the in-plane correlation length (equation 3.3) [139–141].

$x_{xy} \sim 0.9 \times 2\,\pi/fwhm_{intrinsic}(Q_{xy})$ Equation 3.3. The Scherrer formula for the calculation of in-plane correlation length [139–141].

The out of plane Bragg rod intensity was fit using a Gaussian function and the vertical correlation length was calculated using the fwhm of the Bragg rods (equation 3.4) [142].

$L \sim 0.9 \times 2\,\pi/fwhm(Q_z)$ Equation 3.4. The Scherrer formula for the calculation of the vertical correlation length [139–142].

The GIXD experiments were carried out at surface pressure of 3,8 and 12 mNm^{-1} on PBS buffer as the subphase and at the temperature of 22 °C. The GIXD data was analyzed using an open-source software developed by Wei Bu, who is a beamline scientist at ChemMatCARS as well as OriginPro 2018.

X-ray Reflectivity (XR) The XR experiments were carried out at beamline 15-ID-C ChemMatCARS at the Advanced Photon Source (APS) in Argonne National Laboratory using monochromatic X-rays of energy 10 keV. XR is measured as a function of the vertical scattering vector component (Q_z), measuring the variation in electron density $\rho(z)$ of the layers' vertical structure at the air-buffer interface. The film is represented using a slab model as a stack of slabs, with a constant thickness and electron density attributed to each slab. An average of the electron density profile $\rho(z)$ was calculated over both the ordered and disordered parts of the film under the X-ray beam footprint and was calculated by a sum of error functions (Equation 3.5) [141,147,148].

$\rho(z) = \frac{1}{2}\sum_{i-0}^{N-1} \mathrm{erf}\left(\frac{z-z_i}{\sqrt{2}\sigma}\right)(\rho_{i+1} - \rho_i) + \frac{\rho_0 + \rho_N}{2}$ Equation 3.5. The electron density profile[141,147,148].

The erf(z) in equation 3.5 is calculated as $\mathrm{erf}(z) = (2/\sqrt{\pi})\int_0^z e^{-t^2}\,dt$ and N is the number of internal interfaces. σ is the surface roughness calculated from capillary wave theory, z_i is the position of the ith interface, ρ_i is the electron density of the ith interface, and ρ_0 is the electron density of the aqueous subphase [141,147,148]. The X-ray reflectivity measured R (Q_z) is normalized by the Fresnel reflectivity $R_F(Q_z)$. The Fresnel reflectivity $R_F(Q_z)$ is calculated for a perfectly sharp air-water interface. The Parratt method was used to calculate the X-ray reflectivity [141,143–146]. XR measurements were carried out at a lateral surface pressure of 3 mNm^{-1} and temperature

of 22 °C. X-ray reflectivity data was analyzed using the open-source software developed by Wei Bu, beamline scientist at ChemMatCARS.

Grazing Incidence X-Ray Off-Specular Scattering (GIXOS) The GIXOS experiments were carried out at beamline 15-ID-C ChemMatCARS at the Advanced Photon Source (APS) in Argonne National Laboratory using monochromatic X-rays of energy 10 keV. The grazing incident geometry was achieved by fixing the X-ray incidence angle below that of the critical angle for total reflection (α=0.1°), minimizing the scattering from water [146]. The geometry was fixed while collecting the scattering pattern for a range of output angle ß (0° -7.3°) leading to the coverage of the vertical scattering vector component Q_z in the range 0.055 $A^{°-1}$ to 0.647 $A^{° -1}$ for an azimuthal angle θ=0.4 [146]. The 2D Swiss Light source PILATUS 100K set to single photon counting mode was used as the detector with a pixel size of 172 µm by 172 µm and a detected area of 33.5 mm (horizontal) and 83.8 mm (vertical) [146]. The detector was placed 570 mm downstream from the sample. Two sets of guard slits, open at 0.12 mm horizontally and 100 mm vertically, were used in order to reduce the background scattering, one 300 mm downstream from the sample and one directly against the detector [146].

The GIXOS data was normalized to the intensity of the initial minimum I_n in order to increase the reliability of the GIXOS data analysis [146]. Moreover, the scattering from the background was subtracted in all the GIXOS data obtained. A similar slab model technique to XR was used to probe the electron density variation $\rho(z)$ of the vertical structure of the film as a stack of slabs, each with distinct thickness and electron density. GIXOS data was also analyzed using the open-source software developed by Wei Bu, beamline scientist at ChemMatCARS.

Crystallography Analysis PyGid 0.9 xtreme edition is a crystallographic analysis software developed by Dr.Ingo Salzmann. It was used to analyze the Q_{xy} peak positions of cholesteryl esters in the literature using the reported unit cell parameters and compare the peak positions with those obtained in this work in order to determine the cholesteryl oleate unit cell type.

3.4. Results & Discussion

3.4.1. Surface Activity & Morphology

Figures 3.2 and 3.3 show the surface pressure vs. area isotherm and BAM images of the cholesteryl oleate film on PBS buffer at 22 °C, respectively. It can easily be seen that the cholesteryl oleate film has a phase transition at ~6 mNm^{-1}. Although it might be expected from the unit of unsaturation in the CO acyl chain that it would form a more or less fluid film [155], the BAM images of cholesteryl oleate show indications of a condensed phase forming at very low surface pressures (as low as 0.5 mNm^{-1} , image not shown) which is observed alongside an either liquid expanded or gaseous phase, the latter observed in the form of dark holes whose size change with surface pressure. Above the phase transition at ~ 6 mNm^{-1}, two levels of grey are observable in the enhanced BAM images (Appendix A, Figure A2, red arrow), as well as the growth of smaller and brighter domains from within the existing ones.

The emergence of areas with varying degrees of brightness within the BAM images is taken as evidence of multilayering of the film as the surface pressure increases. As the film is compressed to smaller molecular areas, brighter i.e. thicker areas, emerge atop the condensed phase that increase in surface coverage. The film shows three clear brightness levels. The behaviour of multilayering with compression has been suggested previously for different cholesteryl esters [61,158,159], most notably, cholesteryl nervonate films displayed the formation of these thick layers upon previous layers [61].
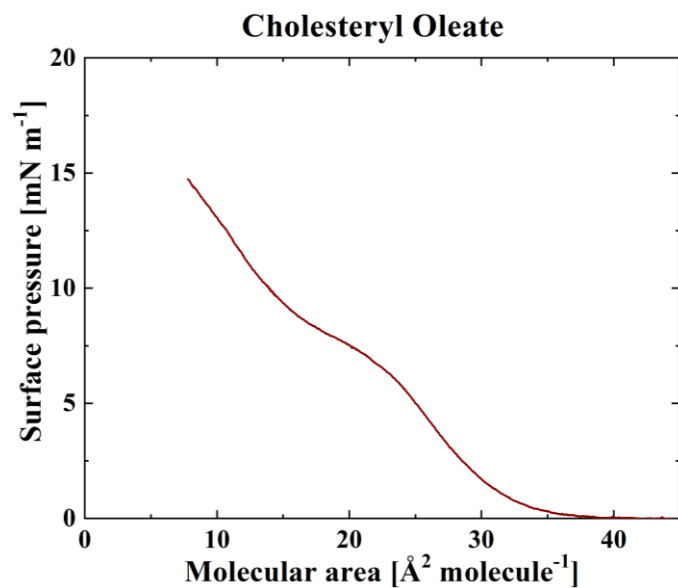
Figure 3.2. Isotherm of cholesteryl oelate on PBS at 22 °C.
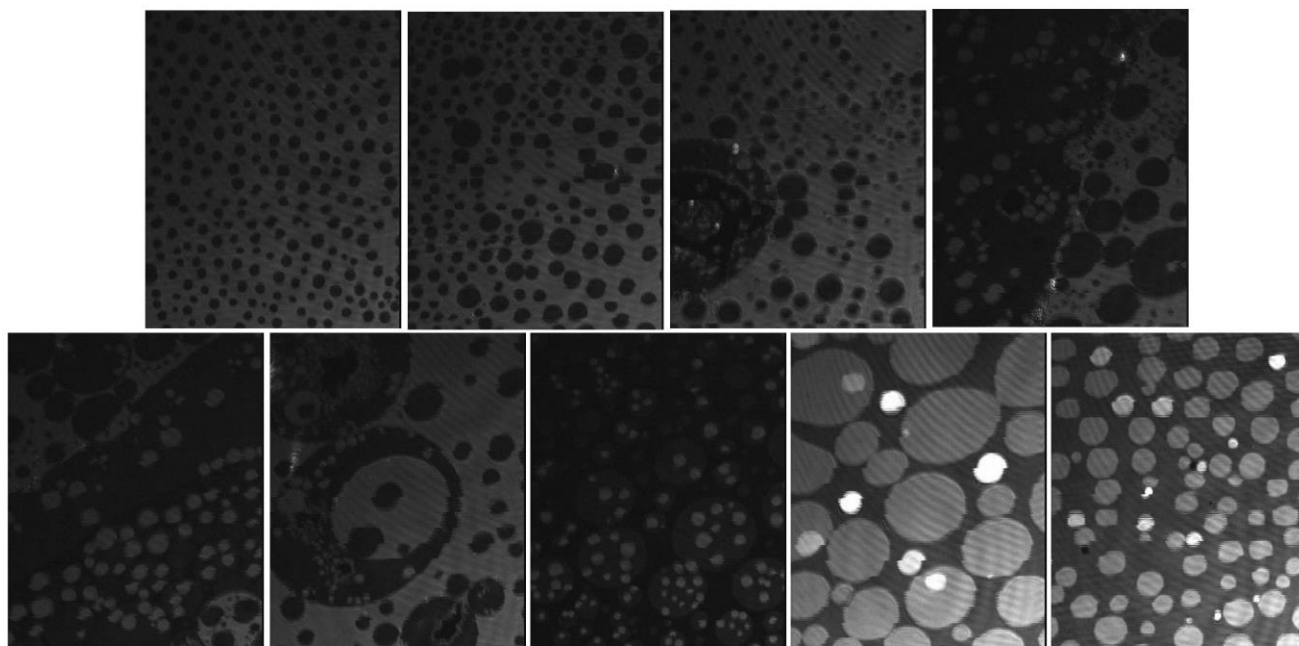
Figure 3.3. BAM images (220 μm wide) of cholesteryl oleate film at surface pressures (top, left to right): 2 mNm⁻¹, 5 mNm⁻¹, 7 mNm⁻¹, 9 mNm⁻¹, (bottom, left to right): 10 mNm⁻¹, 11 mNm⁻¹, 12 mNm⁻¹, 13 mNm⁻¹ and 14 mNm⁻¹ on PBS at 22 °C.

3.4.2. Grazing Incidence X-Ray Diffraction (GIXD) Analysis

In order to further analyze the structure of the condensed phase of CO, GIXD was performed at surface pressure of 3, 8 and 12 mNm^{-1}. Figure 3.4 shows the contour plots of the X-ray intensities for cholesteryl oleate versus scattering vector components horizontal Q_{xy} and vertical Q_z. It can be observed that the intensity of the 2-dimensional plot increases with surface pressure, indicating a higher signal to noise (S/N) ratio. This means that cholesteryl oleate film has a larger number of crystalline domains in the beam footprint at higher surface pressures which cumulatively give diffraction.
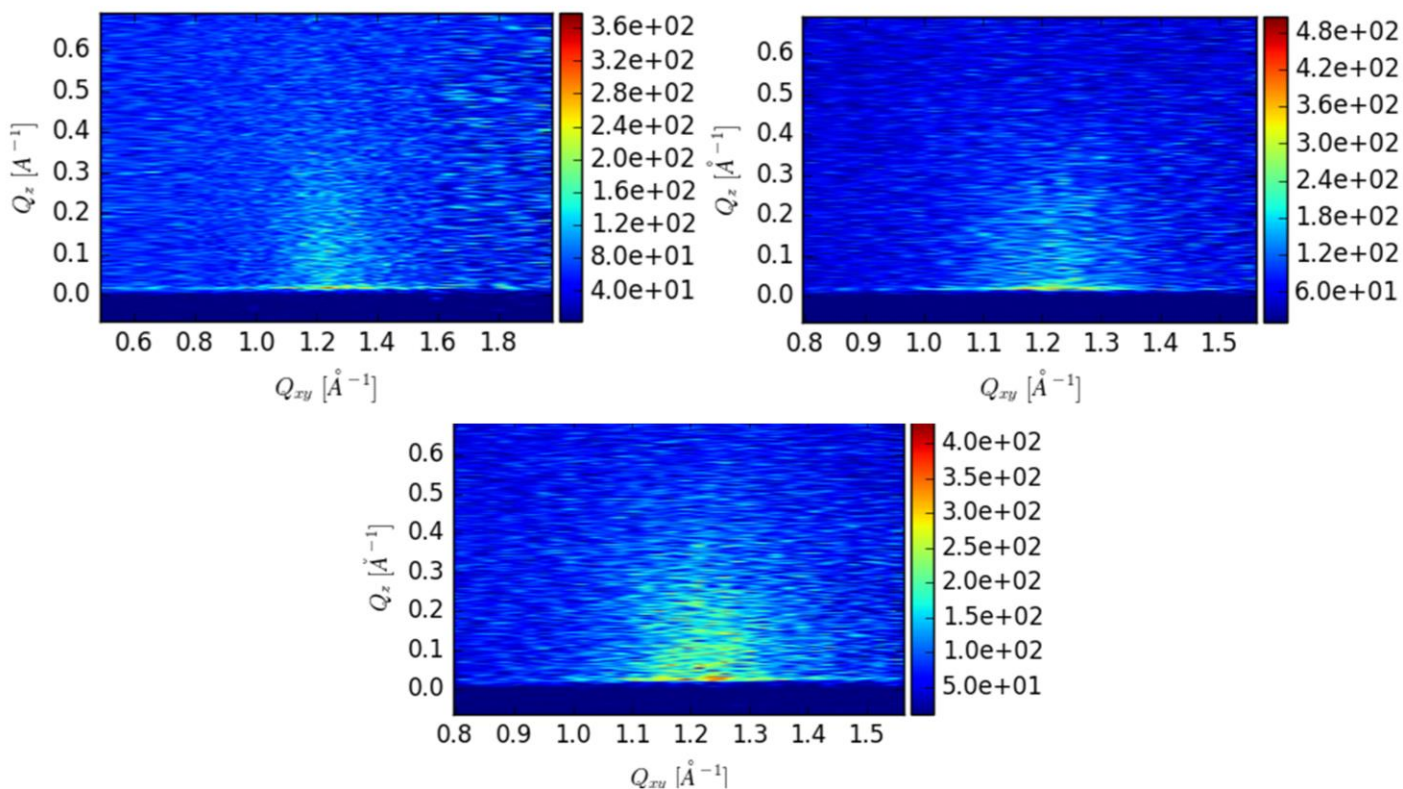
Figure 3.4. Contour plots of the X-ray intensities versus in-plane scattering vector components Q$_{xy}$ and Q$_z$ for cholesteryl oleate at surface pressures (top, left) 3 mNm^{-1}, (top, right) 8 mNm^{-1}, (bottom) 12 mNm^{-1} on PBS at 22 °C.

In order to analyze the GIXD data, initially, the intensity was integrated over the entire Q_z range to generate the Q_{xy} cholesteryl oleate Bragg peak. The resulting Bragg peak is shown in Figure 3.5. The resulting Bragg peak is quite broad peak compared to previous work on cholesteryl esters namely, cholesteryl tridecanoate (CE-13) and cholesteryl stearate (CE-18) who produced multiple sharp and distinct peaks [159]. In the same work however, cholesteryl palmitate (CE-16) was also studied and showed much broader and less intense Bragg peaks [159]. It was deduced that in the case of CE-13 and CE-18 a crystalline interdigitated bilayer results in the best fit [159]. It is important to note that the cholesteryl esters mentioned above, all contain fully saturated acyl chains which impacts the resulting interdigitation. However, cholesteryl oleate, similar to 43% of the cholesteryl esters [30] constituting the TFLL contains an unsaturation in its acyl chain which affects the chain packing behaviour of the molecules in the film and results in a more fluid film and broader diffraction peaks. In fact, the peak observed in Figure 3.5 is quite similar in width and position to the peak generated by cholesterol in the study of the interactions of cholesterol and phospholipid by Ivankin et al. 2010 [167].
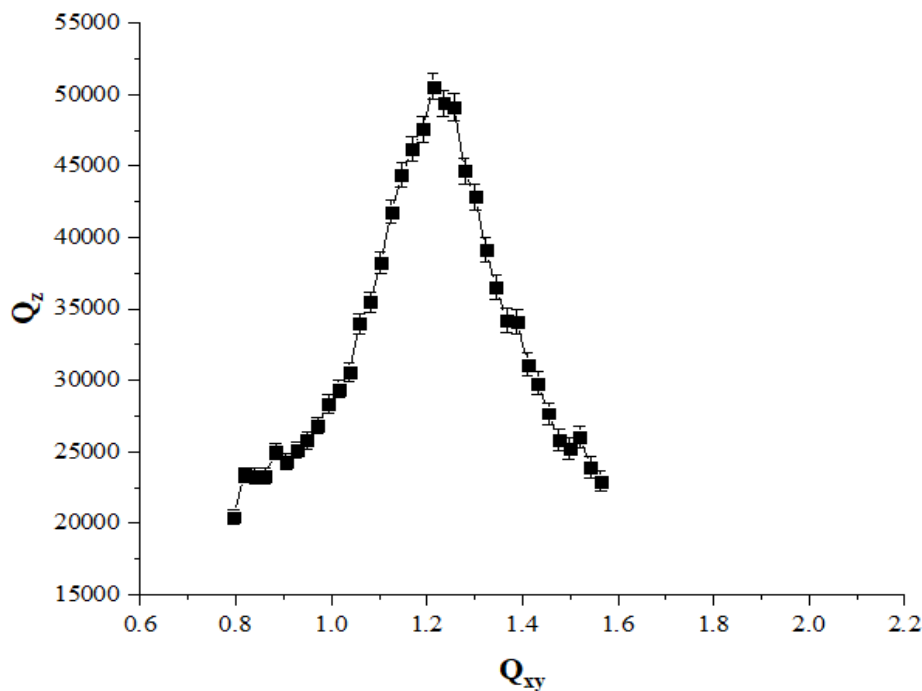
Figure 3.5. Cholesteryl oleate Bragg peak integrated over the entire Q_z range at 12 mNm^{-1} on PBS at 22 °C.

In order to further analyze the data, an approach was adopted wherein small 0.04 Å sized slices across the Q_z range were taken. An example of the result of this approach is shown in Figure 3.6. It can be observed that there are three main fitted Bragg peaks within these slices whose positions remain consistent not only across all the slices but also across surface pressures 3, 8 and 12 mNm^{-1}. It can be observed that the intensity of these peaks is quite low at 3 mNm^{-1}, gradually increasing as the surface pressure increases to 8 and 12 mNm^{-1}. This may be due to fewer crystalline domains at smaller surface pressures, which results in lower intensity of the peaks and higher diffuse scattering from the background (lower S/N ratio). However, as the surface presure increases, and the crystalline domains are compressing together, there is a larger number of domains in the beam footprint resulting in an increased S/N ratio as observed at higher surface pressures.

The average d-spacings and the horizontal correlation lengths of the cholesteryl oleate lattice were calculated and are listed in Table 1. In order to determine the unit cell type of cholesteryl oleate, a crystallography software was used to analyze the Bragg peak positions of previously studied cholesteryl esters and cholesteol using their reported unit cell parameters [159,167,168]. A pattern was observed in the peak positions of the cholesteryl esters CE-13, CE-16 and CE-18 [159] which was quite similar to the peak positions of the three Bragg peaks of cholesteryl oleate (Figure 3.6 and Table 1). The most similar pattern of peaks to those of cholesteryl oleate was cholesteryl acetate reported by Rapaport et al. 2001 [168] wherein a pseudo-rectangular lattice unit cell was suggested and implied that the cholesterol ring structure plays a part in the crystallization of the film. This is similar to previous reports of the crystalline cholesterol film structure [169,170]. Using this comparison, it was deduced that cholesteryl oleate also adopts a pseudo-rectangular unit cell.

Analysis of the Bragg rod showed that all the peaks were found in-plane, (Q_z=0) indicative of an untilted structure. Using the fwhm of the Bragg rod, the thickness of the crystalline portion of the film was determined to be 9.42 Å which corresponds almost exactly to the thickness of the cholesterol ring structure as reported previosuly by Ivankin et al. 2010 [169]. This is further evidence that the crystallinty observed in the cholesteryl oleate film is sourced in the cholesterol ring packing and not the interdigitaion in its unsaturated acyl chain [159].
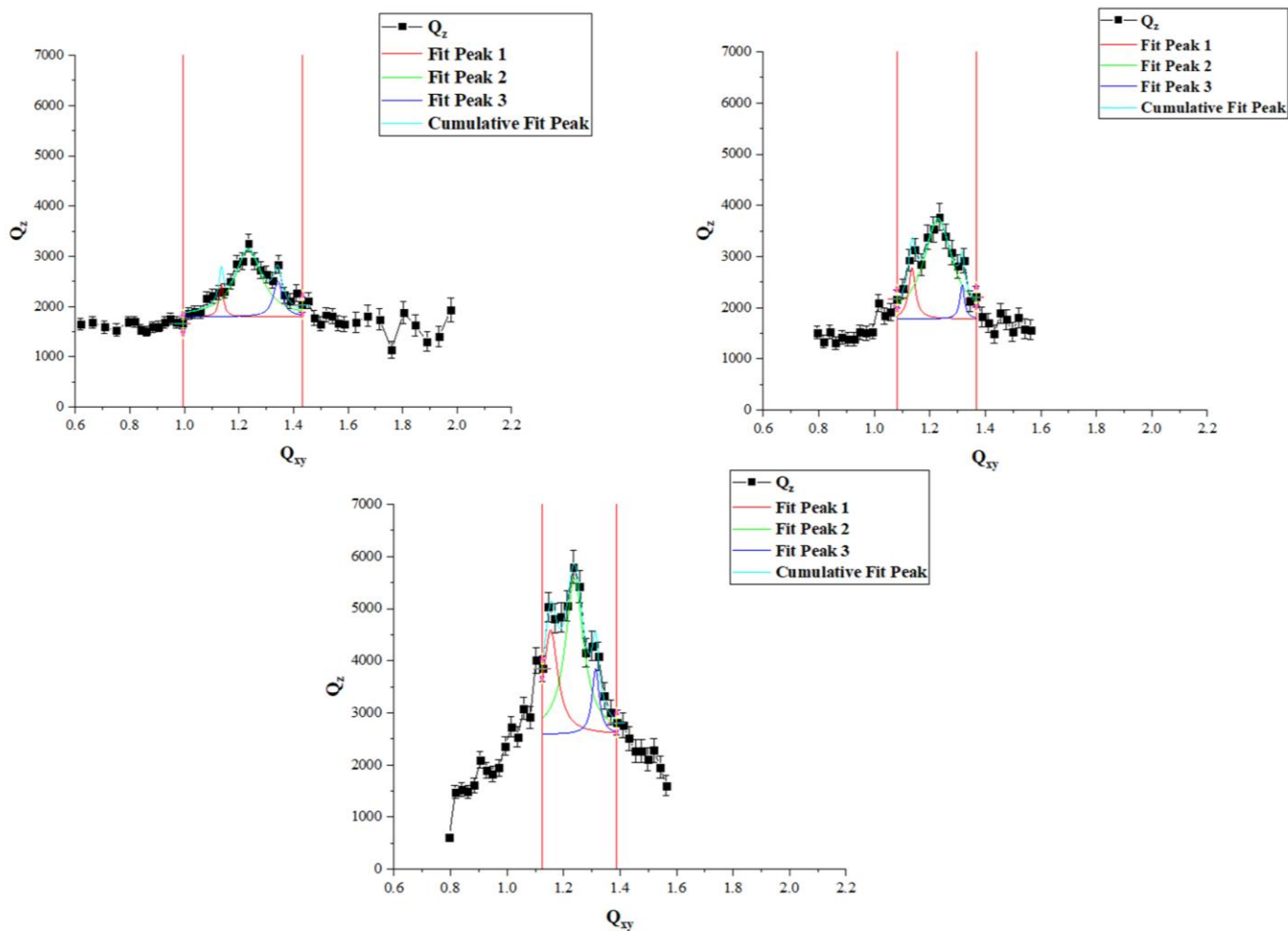
Figure 3.6. Q_{xy} peaks from the slice analysis of cholesteryl oleate at surface pressures (top, left) 3 mNm^{-1}, (top, right) 8 mNm^{-1}, (bottom) 12 mNm^{-1} on PBS at 22 °C.

Table 1. Q_{xy} peak positions, average d-spacing and average correlation length of the crystalline cholesteryl oleate film at surface pressures 3, 8 and 12 mNm^{-1} on PBS at 22 °C. The d-spacing reported represents the average for each peak position across multiple slices.

Pressure (mNm^{-1})		12	8	3
$Q_{xy}1$	Peak Position	1.16	1.13	1.13
	Average d-spacing (Å)	5.42	5.53	5.52
	Average Correlation Length (Å)	74.22	118.51	122.65
$Q_{xy}2$	Peak Position	1.24	1.23	1.23
	Average d-spacing (Å)	5.06	5.1	5.09
	Average Correlation Length (Å)	86.64	44.86	62.89
$Q_{xy}3$	Peak Position	1.31	1.33	1.34
	Average d-spacing (Å)	4.79	4.73	4.64
	Average Correlation Length (Å)	267.01	189.18	84.03

3.4.3. X-Ray reflectivity (XR) & Grazing Incidence X-Ray Off-Specular Scattering (GIXOS) Analysis

In order to analyze and evaluate the vertical layered structure, XR and GIXOS data of cholesteryl oleate were obtained. Using a slab model, based on the electron density and the thickness of each slab, models with 4 slabs generated the best possible fits for the data. The XR data analysis yielded two possible four slab models. The details of these two models are given in Table 2 and Figure 3.7.

In the first model (model 1), the thickness and the electron density of each slab i.e. the chain, the ester, the ring structure, and the smaller chain are in agreement with estimated values for each slab. Regarding the chain electron density, it is possible that the fluidity of the chain especially at the pressure of 3 mNm^{-1} could account for the lower electron density of the chain slab than what is usually expected from films with saturated acyl chains [141,159].

The slab thickness corresponding to the cholesterol ring structure in both models is in acceptable agreement with the scattering rod length obtained from GIXD as well as with literature values for cholesterol ring structure [169] and cholesteryl esters [159]. However, as can be observed in Figure 3.7 the fit with model 1 is not ideal. The notable difference between the two models is that the length of the smaller chain is twice the size of what would be expected in model 2. Model 1 suggests a flat film with the cholesteryl oleate molecules facing the buffer interface with the smaller chain and where no multilayering is occurring at the surface pressure of 3 mNm^{-1}. Model 2 yields chain regions above and below the ring of equal thickness. Given the difference in the length of these chains (Figure 2.2), this could only be explained with an alternating ring orientation. However, such a structure is not compatible with the ring-packing that has been observed from GIXD results both in this work and of cholesterol in the literature [169]. Despite this, model 2 gives a better fit to the data (Figure 3.7).

It is important to note that the XR data was only measured at the surface pressure of 3 mNm^{-1} where the film is quite inhomogeneous (Figure 3.3). At this low surface pressure, the phase coexistence of a condensed phase with a gaseous phase which have very different properties, makes fitting more challenging.

Due to time and film constraints, GIXOS was performed at the higher surface pressure of 8 mNm^{-1}. GIXOS provides the same information as XR but with inherently a lower resolution. The surface pressure of 8 mNm^{-1} was selected as it was just above the CO phase transition and should generate a film with high condensed phase surface coverage and only minimal multilayering. The GIXOS data at this surface pressure supports the validity of XR model 1. It supports the existence of a flat film at the surface pressure of 8 mNm^{-1} and that no multilayering is occurring. However, GIXOS is inherently a lower resolution technique and so XR data from higher surface pressure of CO would be needed to obtain the best model.

Table 2. Fitted parameters for XR and GIXOS data of cholesteryl oleate film at surface pressures 3 and 8 mNm⁻¹ on PBS at 22 °C.

Technique		XR		GIXOS
Model		1	2	1
Pressure (mNm⁻¹)		3	3	8
Chain (Small)	Thickness [Å]	6.3	12.6	6.3
	ρ [e⁻Å⁻³]	0.26	0.28	0.26
Cholesterol Ring	Thickness [Å]	10	10.2	11.9
	ρ [e⁻Å⁻³]	0.4	0.43	0.38
Ester Group	Thickness [Å]	4.7	4.4	3.6
	ρ [e⁻Å⁻³]	0.4	0.39	0.4
Chain (Long)	Thickness [Å]	11.7	12	14.9
	ρ [e⁻Å⁻³]	0.17	0.17	0.36
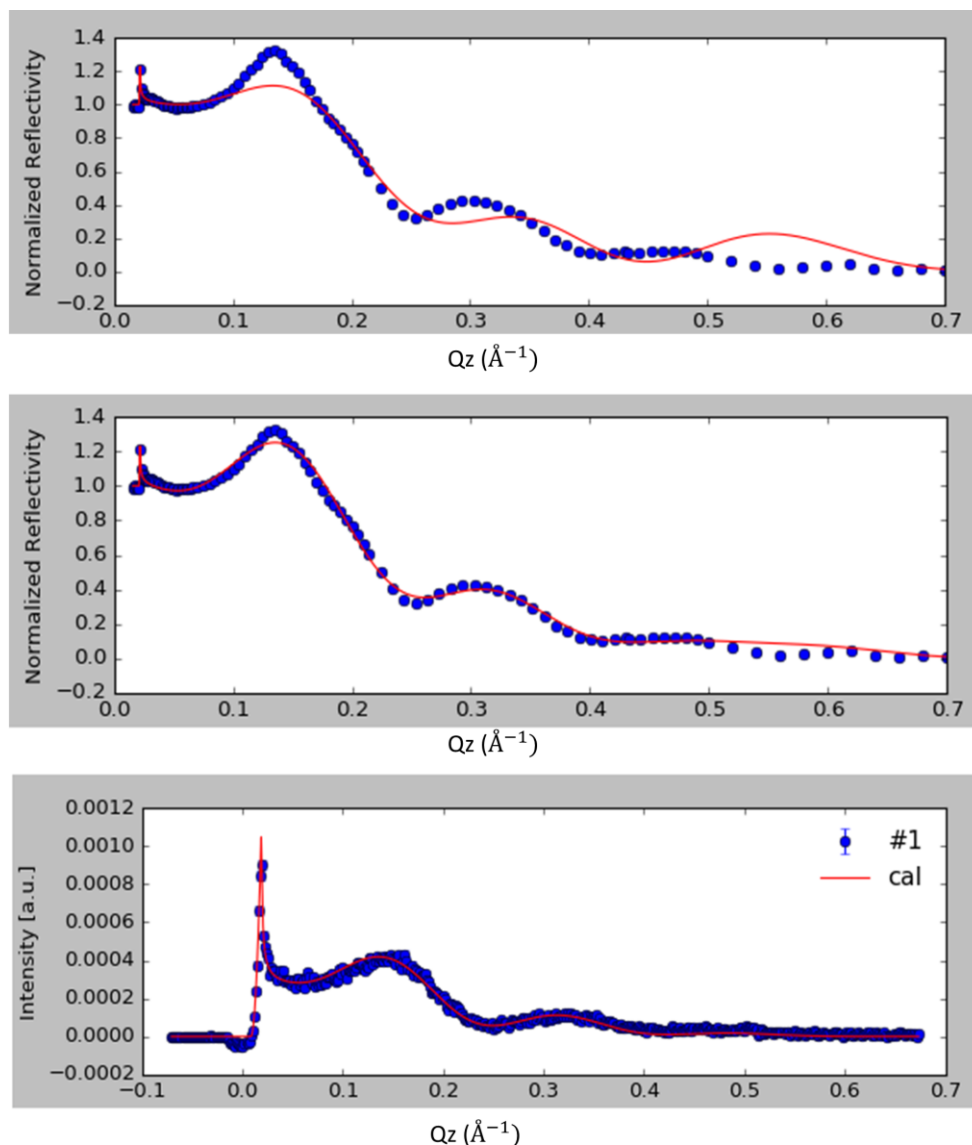
Figure 3.7. Fitted XR models of cholesteryl oleate at surface pressures 3 mNm^{-1} (model 1, top), 3 mNm^{-1} (model 2, middle), and GIXOS model of cholesteryl oleate at surface pressure 8 mNm^{-1} (model 1, bottom) on PBS at 22 °C.

3.5. Conclusion

This study focused on the crystalline structure of the cholesteryl oleate film, as an important cholesteryl ester used in multiple TFLL model membrane studies [16,17,52,53,57,58]. It was deduced that the cholesteryl oleate film forms a crystalline film wherein the crystalline thickness corresponds to that of the cholesterol ring structure. Thus, it is the cholesterol ring packing and not the packing of the cholesteryl oleate unsaturated chains that is the source of the crystallinity.

70

Moreover, no evidence of the chain interdigitation or bilayer formation previously reported for saturated acyl chain cholesteryl esters, was observed [159].

The results of X-ray reflectivity and GIXOS at lower surface pressures, showed that cholesteryl oleate does not form multilayers at lower surface pressures, but forms a flat film with the smaller chain facing the buffer subphase. In order to ascertain the multilayer formation of cholesteryl oleate, evidence of which was reported by BAM, X-ray reflectivity measurements from higher surface pressures are needed. The results of this work can contribute to better understanding the structure of cholesteryl esters with unsaturation in their acyl chain and provide physiologically relevant information on TFLL structure and function.

Chapter 4. Impact of Pollutant Ozone on the Biophysical Properties of Tear Film Lipid Layer Model Membranes

4.1. Abstract

Ozone exposure from environmental smog has been implicated as a risk factor for developing dry eye disease (DED). The tear film lipid layer (TFLL) which is the outermost layer of the tear film and responsible for surface tension reduction while blinking, is in direct contact with the environment and serves as the first line of defense against external aggressors such as environmental pollution. The impact of exposure to ozone on the biophysical properties of three TFLL model membranes was investigated. These model membranes include a binary mixture of cholesteryl oleate (CO) and L-α-phosphatidylcholine (egg PC), a ternary mixture of CO, glyceryl trioleate (GT) and PC as well as a quaternary mixture of CO, GT, a mixture of free fatty acids palmitic acid and stearic acid (FFAs) and PC. Langmuir balance, Brewster Angle Microscopy (BAM) and a Profile Analysis tensiometer (PAT) were used to study the surface activity and respreadability, the morphology as well as viscoelastic properties of the films, respectively. Expansion to higher molecular areas was observed in all the TFLL model membrane films which is attributable to the accommodation of the cleaved chains into the film. Significant morphological changes were observed, namely fluidization and the disruption of phase transition behaviour of GT and multilayer formation of CO. The hysteresis loop of the films was also impacted by ozone exposure. On the other hand, the viscoelastic properties of the films exhibited differential impacts from ozone exposure as a function of composition. These findings are correlated to chemical changes to the lipids determined using ESI-MS.

4.2. Introduction

Tear film lipid layer (TFLL) is the final layer of the human tear film which covers the surface of the cornea and is responsible for creating the air-tear interface [1]. TFLL is mainly composed of lipids secreted by the meibomian glands [8,19]. Despite the many controversies that exist in the literature regarding the exact composition of TFLL, it has been reported that the composition of TFLL is > 90% non-polar lipids [1,8,11,28] with a smaller percentage of polar lipids. The meibum is composed of 30-45 mol% cholesteryl esters (CEs), 30-50 mol% are wax esters [1,8,11,19,22,28,29] 2~4 mol% triglycerides [8,11,28,30], up to 2.5 mol% free fatty acids [3,28,31,32], 0.5-5.6 mol% free

cholesterol [3,8,11,28,30–32] , 2 mol% diesters [3,28,31,32] and 3-7 mol% hydrocarbons [3,28,31,32]. The polar lipids of TFLL are reported to be 3-5 mol% (O-Acyl)-ω-hydroxy fatty acids (OAHFA) [19,25,33] and ~13 mol% phospholipids [1,8,34] of meibomian and non-meibomian origins, respectively.

Despite the controversies in the literature and the challenges regarding the determination of the exact composition of TFLL, there is no doubt that this 15-160 nm thick interface is paramount in the function of blinking, responsible for the tear surface tension reduction [1,6] and the stability of the tear film while blinking by respreading after each blink due to its distinct surface characteristics [1,7,8]. A multilayered structure is suggested for TFLL [16–18] with the polar lipids creating an amphiphilic sublayer on top of the aqueous tear film and the non-polar lipids, creating a hydrophobic bulky layer on top of the polar amphiphilic layer [1,3,8,41]. The amphiphilic nature of the polar sub-layer aids in the spreading of the non-polar lipids on the aqueous layer underneath, allowing the stabilization of the TFLL[1,3,7,8,18,24].

Disruption in the composition and structure of TFLL leads to the development of dry eye disease (DED) which is a multifactorial disease impacting the ocular surface [62]. Meibomian gland dysfunction (MGD) is reported in 86% of DED cases [62,63] wherein an unstable and patchy tear film as well as a non- invasive break up time of <5 s is reported compared with the stable and continuous tear film in healthy subjects with a non- invasive break up time of > 15 s [8,48,83,85,86]. DED is one of the major ophthalmic health concerns of the modern world [8,62] with a life quality altering effect on 10%-30% of the global population [64] and an estimated annual cost of $55.4 billion [8,77] in USA with a similar global impact [8,78]. It is characterized with instability in the tear film, inflammation in the ocular surface as well as tear hyperosmolarity [8,62]. With a prevalence of 21.3% in Canada [73], many risk factors have been associated with DED including MGD [8,65], age [64,66–68], race [62], sex [62,64,66,68,69] and most recently air pollution [64,68,70–72].

Many studies in the recent years have reported a correlation between ophthalmic surface diseases and air pollution with a special emphasis on the air pollutant ozone. Air pollution was reported as one of the risk factors of DED in a study on USA veterans [108,109]. In a time-stratified study in in Hangzhou, China, higher concentrations of air pollutants were significantly associated with DED [70]. A smog analysis in Lahore associated increases in the concentrations of pollutants NO_x, PM_{10}, O_3, SO_2, CO, VOC as well as $PM_{2.5}$ with overall 60% increase in the number of ocular surface

patients with dry eye, irritation and lid erosion being the major contributors [71]. Significant associations have been found between DED prevalence and increased ozone levels in Korea [72,113]. Among other air pollutants, O_3 was reported as a DED risk factor in a large-scale study in China where the prevalence of DED was found to be 61.57% [68]. Moreover, exposure to ozone long term, is associated with increase in inflammation, lower tear production and conjunctival goblet cell density [116,117].

Tropospheric ozone is produced from the photolysis reaction of NO_2 in the troposphere layer which is produced the reaction of NO with the hydroperoxyl radicals (HO_2) which are produced from the reaction of hydrocarbons with hydroxyl radicals [95–98]. A increase in fossil fuel and biomass burning, has caused the increase in surface levels of NO_x radicals [95,97,100] and has led to a major reported increase in ground-levels of ozone compared to the pre-industrial era from 10 to 15 ppb to 30 to 40 ppb now [97,100] with levels as high as 300 ppb in very polluted areas and photochemical smog [101,103,104].

Despite the many studies focused on the correlation between DED prevalence and ground-level ozone concentrations, the research on the impact of ozone exposure on the mechanical properties and biophysical characteristics of TFLL is limited. Ozone is capable of reacting with the unsaturated double bond in the acyl chain of TFLL components via the Criegee mechanism as was shown in a study focused on the impact of ambient ozone exposure on wax esters [123]. Thus, with a large proportion of the TFLL components' acyl chains containing one or more unsaturated carbon-carbon double bond [30], it is valuable to know the impact of ozone oxdiation on the TFLL characteristics.

The goal of this work is to study the impact of ozone exposure on the biophyical and surface characteristics of TFLL model membranes. Three TFLL model membranes are used in this study which are created using a systematic approach of adding on representative components to create more complex mixtures as used in a previous study (Chapter 2). A binary, ternary and quaternary mixture is used which are composed of cholesteryl oleate (CO), egg PC 90:10, CO:glyceryl trioleate (GT):PC 40:40:20 and CO:GT:FFAs (palmitic acid:stearic acid 50:50):PC 40:25:15:20.

The impact of ozone on the surface activity of the model membranes as well as cycle experiments to study the respreadablity of the films, are studied using Langmuir balance.

Brewster Angle Microscopy (BAM) is used to study the morphology of the films and the dilational rheology experiments were carried out using pendant drop experiments by Profile Analysis Tensiometer (PAT). ESI-MS is used to study the products of the ozonolysis. The findings of these experimental techniques begin to describe the impact of ozone exposure on the mechanical and biophysical properties on TFLL and aid in better understanding of the relationship between ozone exposure and DED prevalence.

4.3. Materials & Methods

Materials. L-α-phosphatidylcholine (egg PC, > 99%) was purchased from Avanti Polar Lipids. Cholesteryl oleate (CO, > 98%), glyceryl trioleate (GT, ≥ 99%), palmitic acid (PA, > 99%), stearic acid (SA, > 99%) and phosphate-buffered saline tablets (PBS, pH 7.4, 10 mM phosphate, 137 mM NaCl, 2.7 mM KCl) were purchased from Sigma-Aldrich. HPLC grade chloroform was purchased from Fisher Scientific and used in all experiments as the spreading solvent.

Preparation of Mixtures, Solutions & Subphases. Stock solutions of CO, Egg PC and GT were used to reach molar ratio of 90:10 for the binary mixture and 40:40:20 for the ternary mixture. Stock solutions of PA and SA were used to achieve a molar ratio of 50:50 for the FFA (free fatty acids) mixture to be used as a component of the quaternary mixture. Solutions of CO, GT, FFA and Egg PC were used to reach molar ratios of 40:25:15:20 respectively and make the CO:GT:FFA:PC (Quaternary mixture) mixture. The PBS buffer subphase was prepared by dissolving one phosphate-buffered saline tablet in 200 mL of ultrapure water with resistivity of 18.2 MΩ cm^{-1} from a Milli-Q® HX 7080 water purification system (HC).

Langmuir Film Balance, Surface Activity. Langmuir film balance was used to obtain surface pressure-area isotherm on which the surface pressure (π) is obtained using a Wilhelmy plate. The monolayer solutions with concentrations of up to 1.0 mg mL^{-1} were prepared as explained previously as well as the PBS subphase solution. Monolayer solutions were spread on PBS buffer on a Langmuir trough (NIMA Technologies). 10 minutes was allowed for the films to equilibrate and the chloroform solvent to evaporate. After the equilibration time, the barriers of the Langmuir balance closed at the speed of 5 cm^2 min^{-1} to compress the films and produce the

surface pressure-area isotherms. At least 3 reproducible measurements were performed for each system.

Ozone exposure experiments were performed on the Langmuir trough by enclosing the trough with a Plexiglass cover equipped with and inlet and outlet at opposite ends. After spreading the films and the 10-minute equilibration time, the films were exposed to ozone concentrations of an average of 800 ppb, with a flow rate of 100 mLm^{-1} for a period of 30 minutes, after which the experiments were carried out. To generate ozone, first, dry and hydrocarbon-free air was generated by passing compressed air first through a drying tube filled with anhydrous calcium sulfate and then a VOC scrubber and a ChromGas zero air generator (Parker). A UVP ozone generator with a Pen-Ray lamp (wavelength 185 nm, power 2 to 20 watts) was used and to monitor ozone concentrations as well as the flow of the gas, a 2B Technology ozone monitor based on the absorption level of UV light at 254 nm and an Aalborg digital mass flow controller was used respectively.

Brewster Angle Microscopy, Morphology. Brewster Angle Microscopy (BAM) was performed through coupling Langmuir film balance from NIMA Technologies with an I-Elli2000 imaging ellipsometer (I-Elli2000, Nanofilm Technologies). This ellipsometer has a 50 mW Nd:YAG laser ($\lambda = 532$ nm). The monolayer solutions of the films with concentrations up to 1.0 mg mL^{-1} were spread on PBS subphase and similar to obtaining surface pressure-area isotherms, the barriers of the Langmuir trough compressed the film at the speed of 5 cm^2 min$^{-1.}$ The images of the films were obtained as the films were compressed with a 20X magnification lens and a resolution of 1 μm and an incident angle of 53.15˚.

To carry out the ozone exposure BAM experiments, the Langmuir trough was enclosed with a Plexiglass cover with and inlet and outlet at opposite ends. After spreading the films and the 10-minute equilibration time, the films were exposed to ozone with similar parameters as explained above.

Compression-Expansion Cycles The compression-expansion cycles were obtained by spreading the monolayer solutions on PBS buffe and after the equilibration (10-minutes) and solvent evaporation period, the films were compressed and expanded for 6 consecutive cycles at

the speed of (196 cm^2 min^{-1}) which is the highest achievable speed with the Langmuir trough. The measurements for each system were repeated at least 3 times.

To carry out the ozone exposure cycles experiments, the Langmuir trough was enclosed with a Plexiglass cover with and inlet and outlet at either end. After spreading the films and the 10-minute equilibration time, the films were exposed to ozone with similar parameters as above.

Profile Analysis Tensiometer, Rheology. A SINTERFACE profile analysis tensiometer (PAT) was used for the rheology experiments. Detailed description of this method can be found in the literature [150–152]. The films with concentrations up to 0.1 mg mL^{-1} were spread on a PBS pendant drop with a volume of 13 µL at the area of 32 mm^2. After an equilibration time of 3 minutes, the area was increased to 40 mm^2 followed by an additional 3 minutes of equilibration. After the equilibration time, the drop area was adjusted to 40 mm^2 in order for the TFLL model membrane film specific Step Through Program (STR) programs to begin and perform rheological measurements on the films at different surface pressures.

The axisymmetric drop shape analysis (ASDA) [130,132,133] is used by PAT which relates arc of the drop to the surface pressure using the Young-Laplace equation [130,134]. The surface pressure is calculated by PAT, using a camera and the profile of the drop and so, it is important for the drop to keep its Laplacian shape throughout the experiments. Thus, there must be negligible disturbance to the drop profile such as harmonic distortions as well as drop loss while the measurements are being performed [130]. This can be done by correctly choosing the oscillation frequency and the amplitude of the rheological measurements as it has been previously reported that they can impact rheological measurements [130–132,136,137]. An amplitude of 2.50 % (of the drop area) was chosen in order to minimize such effects [130]. The frequency of 0.16 Hz calculated from the frequency of blinking i.e. 10 blinks per minute in normal subjects as reported previously in the literature [153] to be physiologically comparable.

A system-specific program was built to specifically account for the changes of 1 mN min^{-1} in the slope of the pressure-area isotherms of each film, allowing efficient experiment time. The CO:PC 90:10 (binary mixture) program underwent an initial compression from 40 mm^2 to 37 mm^2, after which there was an equilibration time of 300 seconds. The drop then underwent 25 oscillations for 156.25 s with an amplitude of 2.50 % (of the drop area) and a frequency of 0.16

Hz [153] followed by an equilibration time of 180 s, then compressed to 34 mm^2, equilibrated (300 s), and underwent oscillations of the same parameters. After 4 more repeats of this cycle, the program moved on to the next part where, following the binary mixture isotherm slope change, the drop area change was reduced to ensure the 1 mN min^{-1} surface pressure increase. Thus, after the 5th. oscillations cycles and the equilibration time (180 s), the drop area was reduced from 25 mm^2 to 24.2 mm^2. The same cycle was repeated until the drop area of 15.1 mm^2 was reached with the rheology experiments providing the measurements of viscosity and elasticity of the film [130,132,134].

The initial compression of the CO:GT:PC 40:40:20 (ternary mixture) film was from 40 mm^2 to 38.66 mm^2, after which the drop was equilibrated (300 s) and oscillated with the same parameters as before. After the second set of oscillations and the following equilibration time (180 s), to ensure the 1 mN min^{-1} increase, the amount of reduction of the drop area was changed. The drop area was reduced from 37.33 mm^2 to 35.69 mm^2, followed by equilibration (300 s), oscillations with the same parameters as before, equilibration (180 s) and the next compression. This cycle was repeated until the 12th. set of oscillations had been completed, after whose equilibration (180 s), the next compression comprised of drop area reducing from 20.95 mm^2 to 19.8 mm^2. The same cycle was repeated for a total of 5 times until a drop area of 15.23 mm^2 was achieved.

the initial compression of the CO:GT:FFA:PC 40:25:15:20 (quaternary mixture) program changed the drop area from 40 mm^2 to 38 mm^2, followed by an equilibration time of 300 s, oscillations with similar parameters as before, and an equilibration time of 180 s. The program then entered its second stage where a change in the drop area reduction size was needed, thus the drop area was reduced from 38 mm^2 to 36.1 mm^2, followed by equilibration time (300 s), oscillations of the same parameters and equilibration time (180 s). This cycle was repeated for a total of 12 times, until the area of the drop reached 15.2 mm^2, completing the rheology measurements and providing the dilational surface elasticity and viscosity of the film. For each system, the experiment was repeated at least 4 separate times.

Ozone exposure experiments were performed by first spreading the film followed by a 3-minute equilibration time, after which the drop was exposed to ozone with the same parameters as above in a 40 mL reaction chamber prior to each rheology measurement.

Electrospray ionization mass spectrometry (ESI-MS) was performed on Thermo LTQ Orbitrap Velos mass spectrometer in both negative and positive ESI modes to identify the ozonolysis products. MS samples were prepared by spreading the film on a pendant drop and exposing it to an average of 800 ppb ozone for a period of 30 minutes with similar parameters as the rheology ozone exposure experiment. An average 6 to 10 drops were collected to reach sufficient material for analysis (approximately 30 ng). The drops containing the oxidized lipid material were dried under nitrogen and resolubilized in a 2:1 chloroform/methanol solution and were directly injected in the ESI-MS using an autosampler. Full scans were performed in an m/z range of 15-2000. Mass spectra were analyzed using the software FreeStyle [TM] 1.8 SP2. A putative identification of products was performed based on MS1 data only by comparison to the theoretical mass of known products and pathways.

4.4. Results & Discussion

4.4.1. The Impact of Ozone Exposure on the Surface Activity & Morphology of TFLL Model Membranes

Surface pressure-area isotherms of the three TFLL model membrane systems are presented in Figure 4.1. For all three systems, an expansion to higher molecular areas is observed in their ozone exposed isotherms, which is the most pronounced in the case of the binary mixture, and less so consecutively for the ternary and quaternary mixtures. Similar behaviour was observed in previous work in ozone exposed lung surfactant model membranes composed of phospholipids DPPC and POPG where only POPG contains unsaturated acyl chain in its structure and can be oxidised by ozone [95,130].

It is known that ozone reacts with the carbon-carbon double bond via the Criegee reaction mechanism [120,171,172] which acts through an ozonide being formed leading to the formation of the Criegee intermediate and whose final major products are aldehydes, hydroxyl hydroperoxides or carboxylic acids [122,173,174] and water-soluble species such as short chain aldehyde (nonanal) and

79

nonanoic acid [175]. In the case of the ozonolysis of wax esters by ambient ozone, in addition to these products, a stable ozonide was also observed [123]. Regarding the components of the TFLL model membranes utilized in this work, CO, GT, and > 53% of the egg PC fatty acid distribution have unsaturation in their acyl chains and are predisposed to oxidation by ozone. Thus, the expansion observed in the isotherms could be due to accommodation within the film of the cleaved lipid chains which are the products of the ozonolysis and have altered surface characteristics. Most notably, given the increased polarity upon chain cleavage, the oxidized chains will disrupt the film organization and disturb the packing of the lipid molecules. These alterations affect film permeability and enable the water molecules to enter the film [130,172].

Interestingly, despite the oxidation, all three films retain their amphiphilic characteristics and surface activity, displaying similar or higher surface pressures as they are compressed to lower molecular areas. Moreover, oxidation has also impacted the phase change behaviour of the films i.e. a smoothing effect can be observed in their compression isotherms, where previously distinct phase transitions would be observed. This impact will be further discussed using the BAM imaging.

Following exposure to ozone, the lipid films were collected for analysis by ESI-MS which confirmed the existence of the aldehydes, carboxylic acids, hydroxyl hydroperoxides, stable ozonide as well as interestingly some Criegee intermediates, all of which contribute to the film's net surface behaviour (Appendix A, tables A1, A2, and A3). It was previously reported by Thompson et al. 2013 [176] that the exposure of 1-palmitoyl-2-oleoyl-sn-glycero-3-phosphocholine (POPC) to ozone leads to the C9 fragment being lost, either entering the bulk phase or gas phase and the increase in the surface pressure was attributed not to the incorporation of the separated C9 fragment into the film but to the rearrangement of the molecules to allow for the reversal in the orientation of the damaged oxidized acyl chain and its incorporation into the film led by the formation of an aldehyde or carboxylic acid group at the tail [95,176].

Compared with the impact of oxidation on the ternary and the quaternary mixture films, the increase in surface activity for the binary mixture is much more prominent. Since 90% of the composition of this mixture is CO, it is reasonable to assume that with nonanal leaving the film through either evaporation or dissolution, the enhanced surface activity observed in the binary

film post oxidation may be due to the incorporation of the CO aldehyde and carboxylic acid chains into the film through orientation reversal or the stable ozonide remaining in the film, which has lead to the an almost two-fold increase in the surface activity observed. The same impact may also be attributed to the aldehyde and carboxylic species observed from egg PC oxidation [95,176].

As noted already, the ternary mixture also shows an expansion to higher molecular areas post oxidation that is less extensive than that observed with the binary mixture. ESI-MS revealed that oxidation of GT yielded products with varying degrees of reaction progress, that is, combinations of uncreated chains, Criegee intermediates, fully oxidized aldehydes and carboxylic acids (Appendix A, Table A2). With some of the products, all of the chains are found in the fully reacted aldehyde form, moreover, no stable ozonide is observed. These species may also be incorporated into the film much as explained before, although one might assume that the smaller percentage of CO compared with the binary mixture led to the smaller film expansion upon oxidation. However, considering the ESI-MS analysis shows oxidation of the unsaturated acyl chains of CO, GT and PC, there may be competing factors impacting the film's behaviour and the smaller impact of oxidation on the ternary mixture isotherm (incorporation versus dissolution of products).

As for the quaternary mixture, it is expected that this film would be less predisposed to oxidation due to 15% of the film composition being FFAs with saturated acyl chains. This is observed with the smaller shift to higher molecular areas, meaning there was less need for the accommodation of the Criegee reaction products in the film. It is apparent that the GT oxidation products also play a role in the increase in the surface activity of the film, as the reduction of their composition percentage has led to reduced surface activity in the oxidated quaternary film. This is especially the case, since the addition of saturated acyl chain FFAs has not helped the film retain its surface activity. As the reduction of surface tension is paramount as one of the major functions of TFLL, the reduction in the maximum surface pressure attained by the film due to the existence of damaged lipid species in the film, will strain the overall TFLL system. Moreover, the oxidation has impacted the envelope transition of GT [12,160] in both the ternary and quaternary films, (evident both from the isotherms and BAM images). This could imply that the oxidized GT species do not have a GT typical phase transition, possibly impacting the film stability.
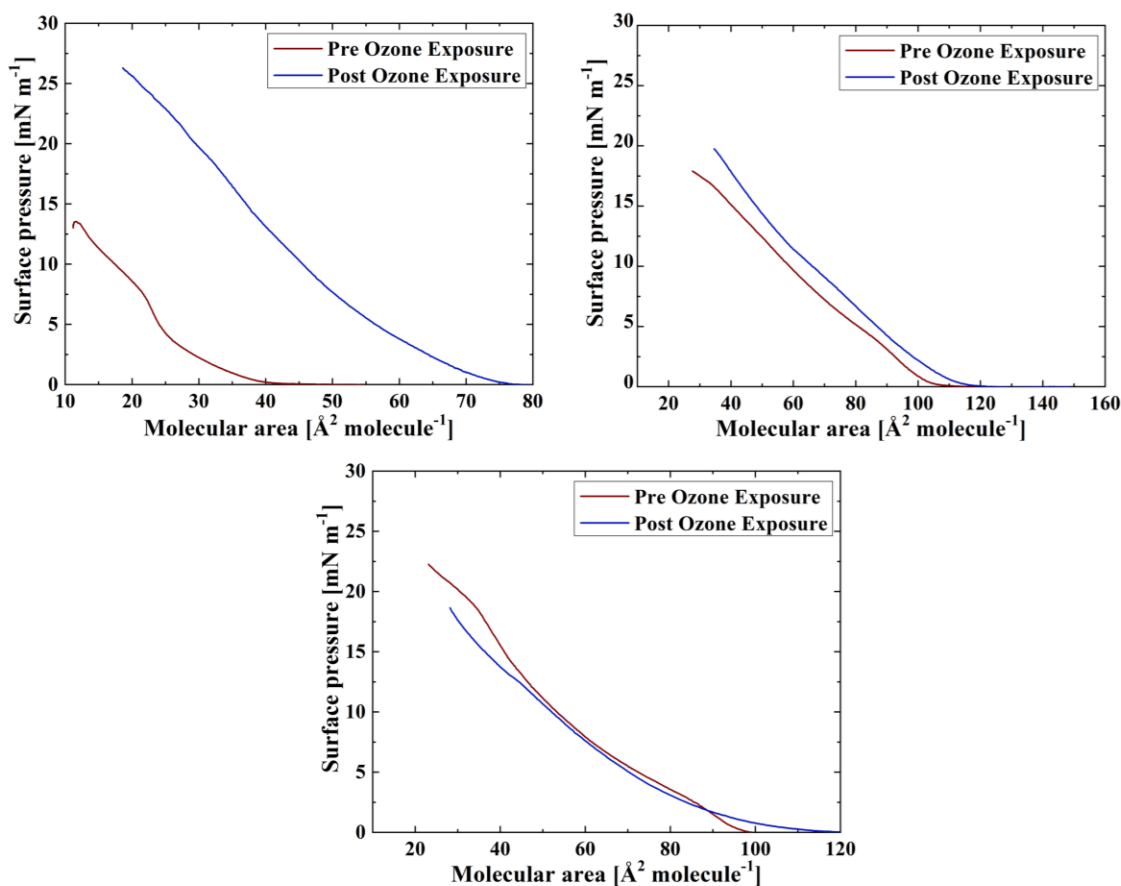
Figure 4.1 Isotherms of CO:PC (binary mixture) (top, left), CO:GT:PC (ternary mixture) (top, right) and CO:GT:FFA:PC (quaternary mixture) (bottom) before ozone exposure (red) and after ozone exposure (blue) on PBS at 22 °C.

The BAM images of the CO:PC 90:10 (binary mixture) film (Figure 4.2 A&B) show significant morphological changes to the film after ozone oxidation. The oxidized film shows what is predominantly gaseous or LE phase, with some circular domains periodically appearing with low contrast (5 mNm⁻¹, Appendix A, Figure A3, red arrow), whereas at the same pressures for the unoxidized film, the growth of the condensed phase domains could be easily observed. This is in agreement with the isotherms wherein the phase transitions are not as apparent for the oxidized film as they are on the unoxidized film. Moreover, periodically irregular aggregates with higher contrast appear (Figure 4.2 A, 7 mNm⁻¹) on a film that seems to be predominantly in a fluid phase. This is quite different from the unoxidized film where at the same pressures, a large

surface percentage of the film is predominantly covered by condensed phase domains. Thus, the oxidation of CO unsaturated acyl chains has impacted the domain formation of the film and the packing of the cholesteryl oleate molecules, and as a result, the eventual multilayering which is observed on the unoxidized film at higher surface pressures. More than 53% of the PC fatty acid distribution contains unsaturated acyl chains and the majority of these lipid molecules comprise at least one unsaturated chain which can be impacted by ozone exposure.

Interestingly, the ozone exposed binary film eventually starts to display a phase transition and more regular and brighter domains begin to appear at around 12 mNm^{-1} (image not shown). Where in the unoxidized binary film at pressure of 13 and 14 mNm^{-1}, the film shows predominantly condensed phase with evidence of multilayering (two brightness levels), the oxidized film shows regular and small domains of condensed phase surrounded by a predominantly fluid film, thus oxidation has made the film fairly fluid. The phase transition and the domain formation of the film may be from the cholesterol ring packing in the oxidized species, evidence of which was gained through GIXD of CO film (Chapter 3). The same behaviour is also observed at higher surface pressures than reachable by the unoxidized film, where small areas of very bright multilayers with a higher level of brightness than that of the condensed phase domains are observed until mostly irregular aggregates are apparent. It was observed that after the compression of the oxidized film was finished and the Langmuir trough barriers remained closed, the film's surface pressure almost immediately lowered and large areas of very bright chain-like aggregates were detected (Figure 4.2 B, the last image to the right), which is evidence of oxidation disrupting the oxidized film's otherwise stable characteristics.

A
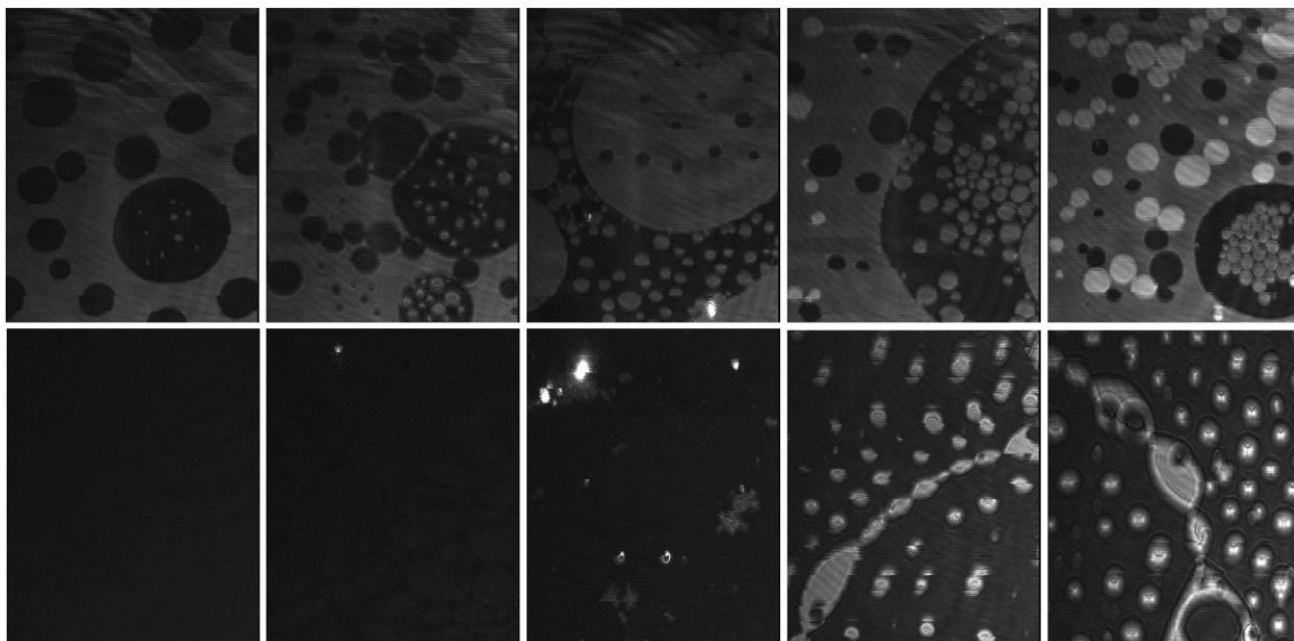
B
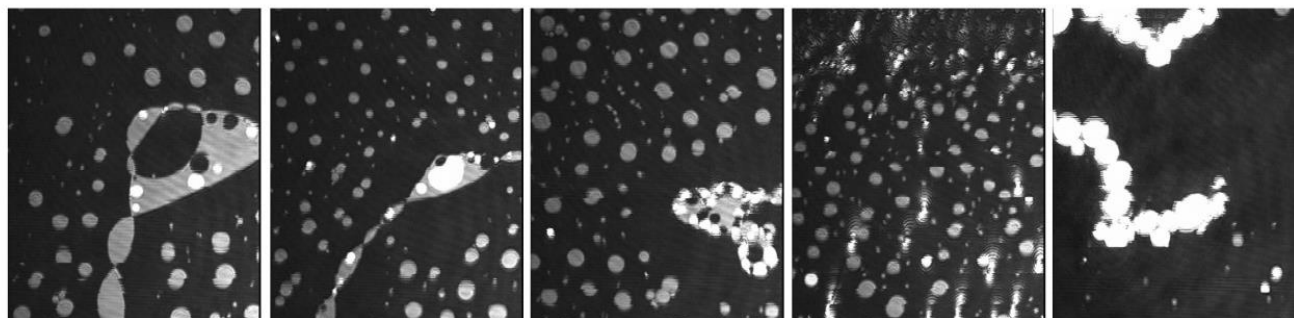
Figure 4.2. (A) BAM images (220 μm wide) of CO:PC 90:10 (binary mixture) film at surface pressures (left to right): 2 mNm^{-1}, 5 mNm^{-1}, 7 mNm^{-1}, 13 mNm^{-1} and , 14 mNm^{-1} before ozone exposure (top) and after ozone exposure (bottom) on PBS at 22 °C. (B) BAM images (220 μm wide) of CO:PC 90:10 (binary mixture) film at surface pressures (left to right): 16 mNm^{-1}, 18 mNm^{-1}, 19 mNm^{-1}, 23 mNm^{-1} after ozone exposure on PBS at 22 °C. The last BAM image to the right is of CO:PC 90:10 (binary mixture) film at surface pressure of 20 mNm^{-1} after ozone exposure on PBS at 22 °C taken after the end of film compression.

The BAM images of the CO:GT:PC 40:40:20 (ternary mixture) (Figure 4.3 A&B) shows the impact of oxidation by ozone exposure on the morphology of the film. At the same pressures, the oxidized film has become more fluid with much smaller CO domains than the unoxidized film.

Thus, it can be deduced that the oxidation of CO acyl chain has impacted its domain growth behaviour which is readily observed on the unoxidized film.

Most notable is the impact of oxidation on the envelope transition of GT in the ternary mixture. On the unoxidized film, the transition of GT into aggregates of similar diameter occurs through the expulsion of GT from the film as was previously observed [160], whereas this transition into three-dimensional aggregates, is not observed on the oxidized film. This is attributed to one or more of the GT acyl chains being oxidized. Instead, the oxidized film shows small domains of CO increasing in number but not size as the surface pressure increases to higher than those achieved by the unoxidized film.

Similar to the binary mixture, the ternary mixture morphology and surface behaviour was also investigated after the compression was finished where the Langmuir trough barriers remained closed (Figure 4.3, B, the last three images to the right), immediately after which, the surface pressure of the film dropped, and the film showed irregular aggregates with CO like domains surrounded by brighter and thicker 3-dimensional aggregates.

A

B
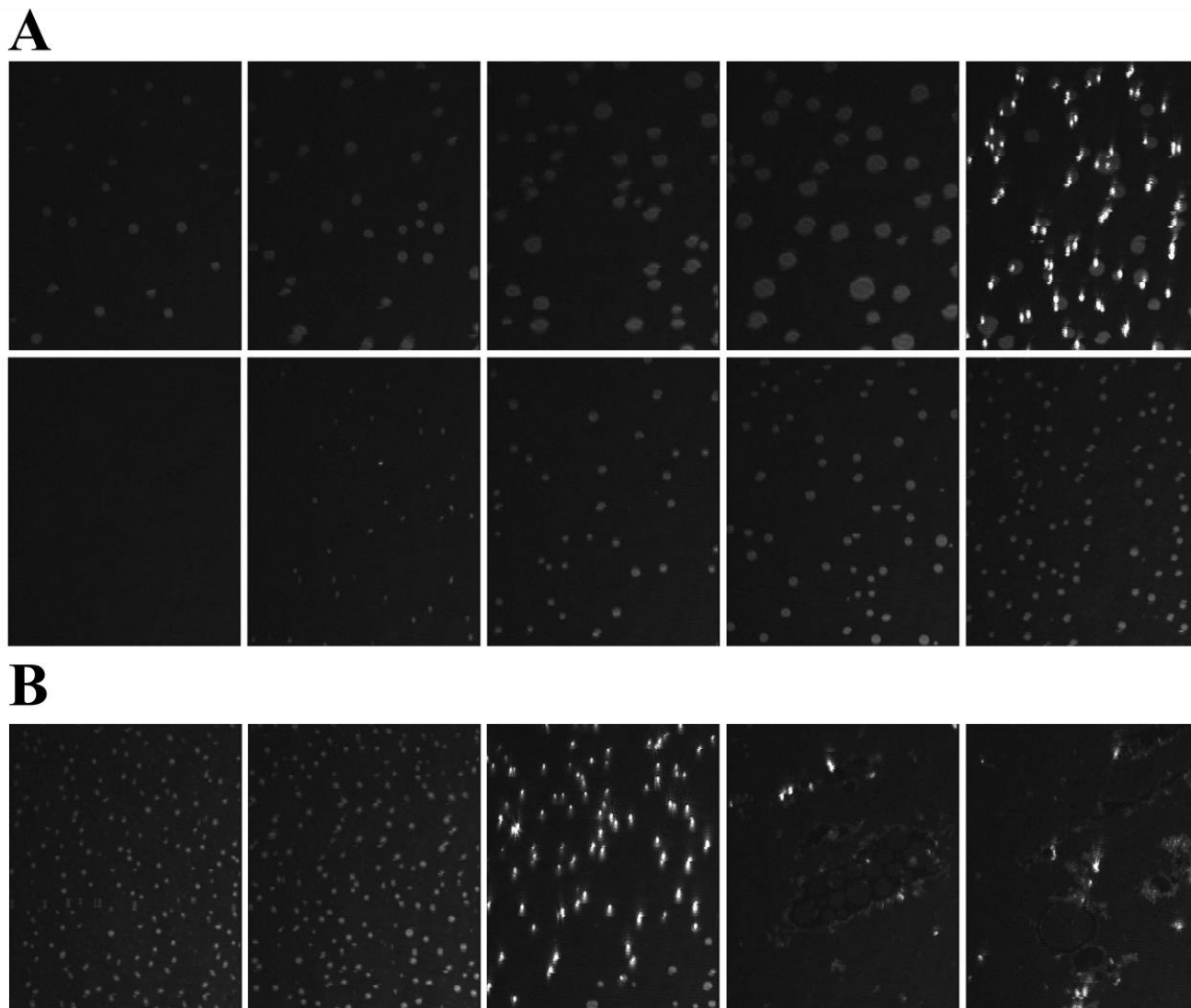
Figure 4.3. (A) BAM images (220 μm wide) of CO:GT:PC 40:40:20 (ternary mixture) film at surface pressures (left to right): 7 mNm⁻¹, 9 mNm⁻¹, 12 mNm⁻¹, 14 mNm⁻¹ and , 17 mNm⁻¹ before ozone exposure (top) and after ozone exposure (bottom) on PBS at 22 °C. (B) BAM images (220 μm wide) of CO:GT:PC 40:40:20 (ternary mixture) film at surface pressures (left to right): 18 mNm⁻¹ and 20 mNm⁻¹ after ozone exposure on PBS at 22 °C. The last three BAM images to the right is of CO:GT:PC 40:40:20 (ternary mixture) film at surface pressures (left to right): 18 mNm⁻¹, 16 mNm⁻¹, 15 mNm⁻¹ after ozone exposure on PBS at 22 °C taken after the end of film compression.

The BAM images of the CO:GT:FFA:PC 40:25:15:20 (quaternary mixture) show that at the same surface pressures on the oxidized film, there are more CO condensed phase domains than on the unoxidized film. Moreover, while before ozone exposure, the domains show a growth in their size, but this does not seem to be the case post-ozone exposure, though the surface coverage

86

of the CO domains has increased. Additionally, the contrast between the phases is diminished after oxidation which may be due to a decrease in domain thickness due to chain cleavage. The smaller size of the CO domains on the oxidized film may be due to the presence of the saturated chain FFAs component which affects the line tension and are enriched in these domains as other components are oxidized. A similar impact was previously observed as a result of PA on a lung surfactant model [95]. Therefore, though they cannot be oxidized, the FFAs can still impact the film's characteristics post-oxidation. This is observed in the CO domains as there is a noticeable difference in the post oxidation morphology behaviour of the ternary and the quaternary films, even though their CO composition is the same.
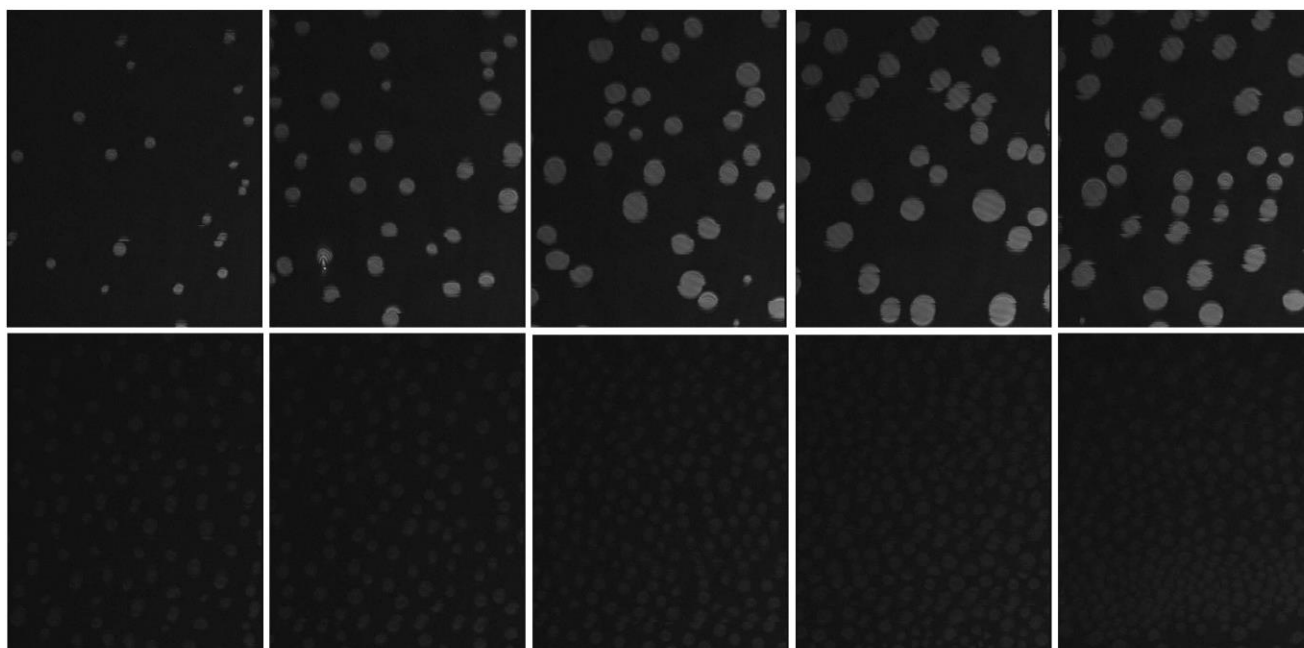
Figure 4.4. BAM images (220 μm wide) of CO:GT:FFA:PC 40:25:15:20 (quaternary mixture) film at surface pressures (left to right): 5 mNm^{-1}, 9 mNm^{-1}, 13 mNm^{-1}, 16 mNm^{-1} and , 18 mNm^{-1} before ozone exposure (top) and after ozone exposure (bottom) on PBS at 22 °C.

4.4.2. The Impact of Ozone Exposure on Compression-Expansion Cycles of TFLL Model Membranes

Figure 4.5 shows the impact of oxidation by ozone on the compression-expansion cycles of the model TFLL films. The compression-expansion rate used (196 cm^2 min^{-1}) is slower than the average blinking rate of 10 blinks per minute [153], however, it is the highest possible speed by the Langmuir trough used, in order to mimic the blinking cycle. Figure 4.6 shows the change in relative area percentage at the representative pressure of 10 mN m^{-1} as a function of cycle number. The relative area percentage is the percentage of the film area relative to the molecular area of the first cycle at 2 mN m^{-1}. The compression-expansion cycles shown in Figure 4.5 have been normalized to their relative area for easier comparison of ozone impact. To study the cycles expressed by their molecular area, please refer to Appendix A, Figure A4. There are two key parameters that are evaluated through these compression-expansion cycles: 1. Changes to the hysteresis loop wherein the area between the compression and expansion represents the work done in the cycle representing the blinking process. 2. The extent to which the films recover after each subsequent cycle, that is the shift in area per molecule, which is indicated by the slope of the change in the relative area % as a function of cycle number (Figure 4.6). Respreadability and reversibility are of paramount importance in the proper function of a healthy TFLL[7,9], observed typically as a characteristic of extracted meibum films [49,55,161,162].

Other than the expansion observed due to oxidation of the binary mixture film and the increased surface activity, also observed in the isotherms (Figure 4.1), the impact of ozone on the respreadability of the films is fairly small. The impact of ozone on the compression-expansion cycles of the binary mixture can more easily be observed in Figure 4.6 where before oxidation hysteresis (the difference between compression and expansion) got larger as a function of cycles, but interestingly, a smaller hysteresis is observed from the oxidized film.

The binary mixture displays high respreadability before ozone exposure, indicated by the fairly constant relative area as a function of cycles, which was previously suggested to be the result of reversible multilayer formation (Chapter 2), adding to the stability of the film. The compression isotherms are relatively similar, reflecting a high recoverability after a couple of priming cycles. Thus, the respreadability has only been slightly impacted as a result of ozone oxidation, which is possibly due to the reduced multilayering of the film as well as a larger composition of the film

being composed of lipids with saturated fatty acid chains. However the expansions show distinctly different relative areas pre- and post exposure but do not appear to change significantly with cycle number for either. The greater difference between the compression and expansion cycles (Figure 4.6) reflects a larger hysteresis pre-exposure, however it should be noted that the loss of the distinct phase transition amplifies the difference at this particular pressure (10 mNm^{-1}) which is the phase transition. The oxidation seems to have reduced this observed hysteresis.

For the ternary mixture, both pre- and post oxidation compression isotherms show a shift in the molecular area at pressure below the phase transition, evidenced by the slope of the line in Figure 4.6. This shift is only observed on the oxidized film above the phase transition pressure (Figure 4.5), this is likely because the GT envelope transition was impacted by oxidation (observed in isotherms and BAM images). It can be suggested that the lack of reversibility could have been caused by the disruption of the typically reversible GT phase transition i.e. GT acyl chains have oxidized and no longer pack as they normally would. As with the binary mixture, the size of the hysteresis loop is larger in the pre-oxidized film, evident from the difference between the compression and expansion isotherms in Figure 4.6, although less pronounced in the ternary mixture.

The quaternary mixture isotherm is less spreadable by nature even pre-oxidation which may be attributable to the existence of the saturated chain FFAs which are known to reduce the respreadability of the film as opposed to films primarily composed of unsaturated acyl chain lipids [7,49,55,163–166]. The impact of ozone exposure on the quaternary mixture cycles is quite small. Previous to oxidation, the film showed little respreadability typical to films with higher proportion of saturated acyl chain lipids [7,49,55,163–166]. It can be observed that after being oxidized, the respreadability slightly reduces which is expected due to the higher saturated chain lipid composition (PC). Moreover, similar to the film before oxidation, the oxidized film also shows a similar hysteresis pattern as a function of cycles where the hysteresis is reduced at higher cycle numbers.
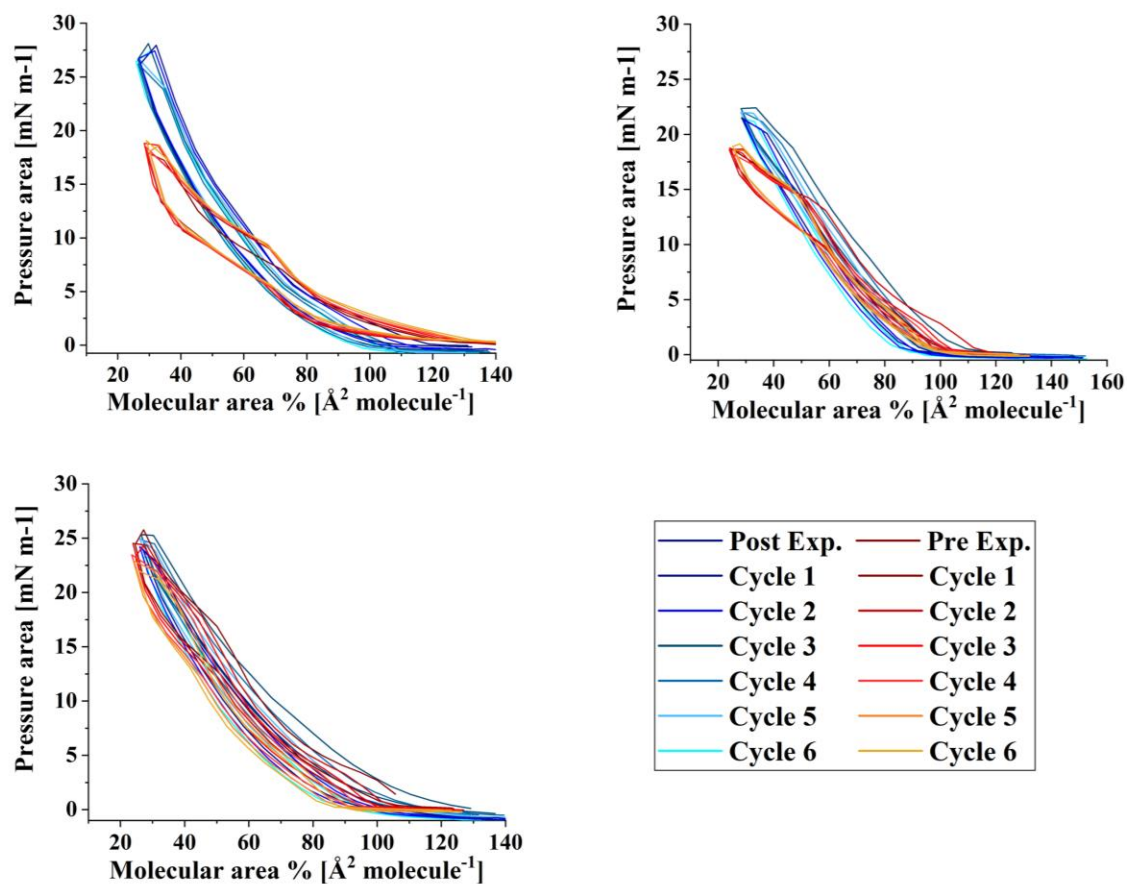
Figure 4.5. Compression-expansion cycles of CO:PC 90:10 (binary mixture, top, left), CO:GT:PC 40:40:20 (ternary mixture, top, right) and CO:GT:FFA:PC 40:25:15:20 (quaternary mixture, bottom) before ozone exposure (red color family) and after ozone exposure (blue color family) on PBS at 22 °C.
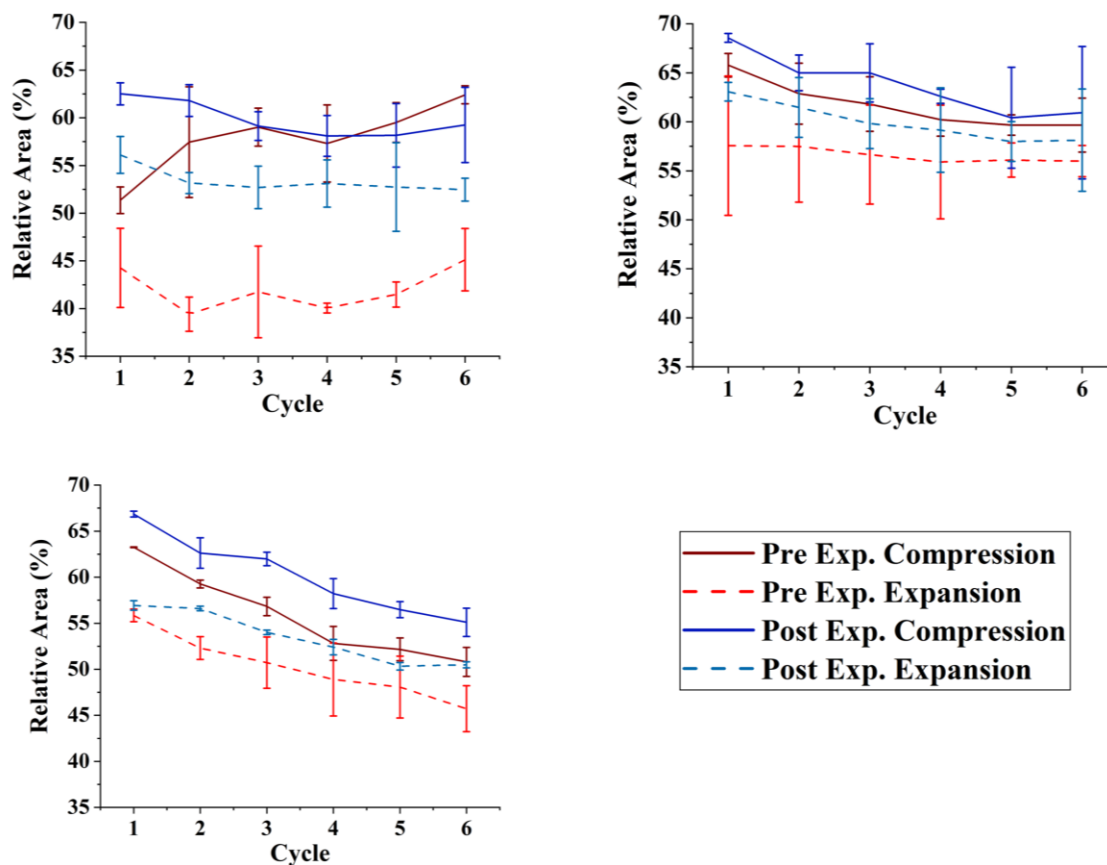
Figure 4.6. The relative area at 10 mNm⁻¹ of the compression (dark red line (before ozone exposure), dark blue line (after ozone exposure)) and expansion (dashed light red (before ozone exposure), dashed light blue (after ozone exposure)) as a function of the number of cycles of CO:PC 90:10 (binary mixture, top, left), CO:GT:PC 40:40:20 (ternary mixture, top, right) and CO:GT:FFA:PC 40:25:15:20 (quaternary mixture, bottom) before ozone exposure (red) and after ozone exposure (blue) on PBS at 22 °C. The data points and error bars represent the mean and standard deviation of at least three independent cycling experiments.

4.4.3. The Impact of Ozone Exposure on the Rheology Measurements of TFLL Model Membranes

The impact of ozone exposure on the viscoelastic properties of the TFLL model membrane films is shown in Figures 4.7 and 4.8. For further details on the description of the technique and the programs used for each film, please refer to section 4.3. The oscillation frequency chosen for the rheological measurements (0.16 Hz) is similar to the reported blinking frequency in healthy subjects in the literature [153] in order to ensure physiologically comparable results as well as no deviation from the drop's Laplacian shape (< 1Hz) [135].

It can immediately be observed that the binary mixture rheology measurements show the highest standard deviations compared with the other two mixtures. This is evident in the rheology

measurements both before and after exposure to ozone. The high standard deviation of the binary film is especially observable in molecular areas smaller than 27 Å^2 molecule^{-1} which is where the film shows evidence of multilayering. The inhomogeneity generated by the multilayering appears to impact the response of the film to oscillations, which is amplified with increasing hysteresis. Although the ozone exposure reduced the multilayering to only very small and occasional areas at smaller molecular areas, the standard deviation for the exposed film remains high at these areas compared to the other mixtures. Moreover, the ozone exposure seems to have increased the elasticity of the film throughout the compression. It is important to note that in the oxidized binary film, for the same areas, the surface pressure is much higher (Figure 4.1) which contributes to the higher elasticity and viscosity observed. In the case of viscosity, the differences due to ozone exposure are only observed at areas smaller than 23 Å^2 molecule^{-1}. The viscosity and the elasticity increases can be attributed to the remaining CO moiety after the chain has cleaved off, adding to the elasticity and viscosity of the film at areas where condensed phase forms by the remaining CO moiety.

Interestingly, the impact of ozone exposure on the ternary mixture is negligible for both the elasticity and the viscosity of the film. Compared to the binary mixture, the addition of GT has already reduced the multilayering and increased the fluidity of the pre-oxidation film as seen in BAM (Figure 4.3). This dominance of the fluid phase is retained even after oxidation (Figure 4.3). which explains the low viscosity and elasticity and the lack of change upon oxidation.

In contrast to both binary and ternary mixtures, ozone exposure decreases both the elasticity and the viscosity of the quaternary mixture film where the viscosity of the film remains at ultra low values throughout the compression. It is important to note that unlike the binary mixture, for the quaternary mixture, the shift in molecular area upon oxidation is very small.

For the binary mixture, it was the change in the surface pressure at a given area that was a dominant factor in the elasticity and viscosity increase upon oxidation. For the quaternary mixture, this was not the case and therefore changes in the intermolecular interactions and morphology of the film are implicated. An intermediate molecular area shift is observed in the ternary mixture and morphology changes similar to the quaternary mixture. Thus, it can be

deduced that the apparent small impact of ozone exposure on the ternary mixture is probably due to the existence of competing factors.

One of the factors is clearly the reduced CO content in both ternary and quaternary mixtures compared with the binary mixture. Thus, any of its oxidation products which seemingly are the reason behind the increase in the binary mixture's elasticity and viscosity, are now present in lower amounts and its impact is observed in the form of no impact or reduction of elasticity and viscosity of the ternary and quaternary mixture films. It can also be deduced that GT's oxidation products have an increasing impact on the viscoelastic properties of the films as well, as can be seen from the lowered elasticity and viscosity of the quaternary mixture post oxidation as opposed to the negligible impact of oxidation on the ternary mixture.
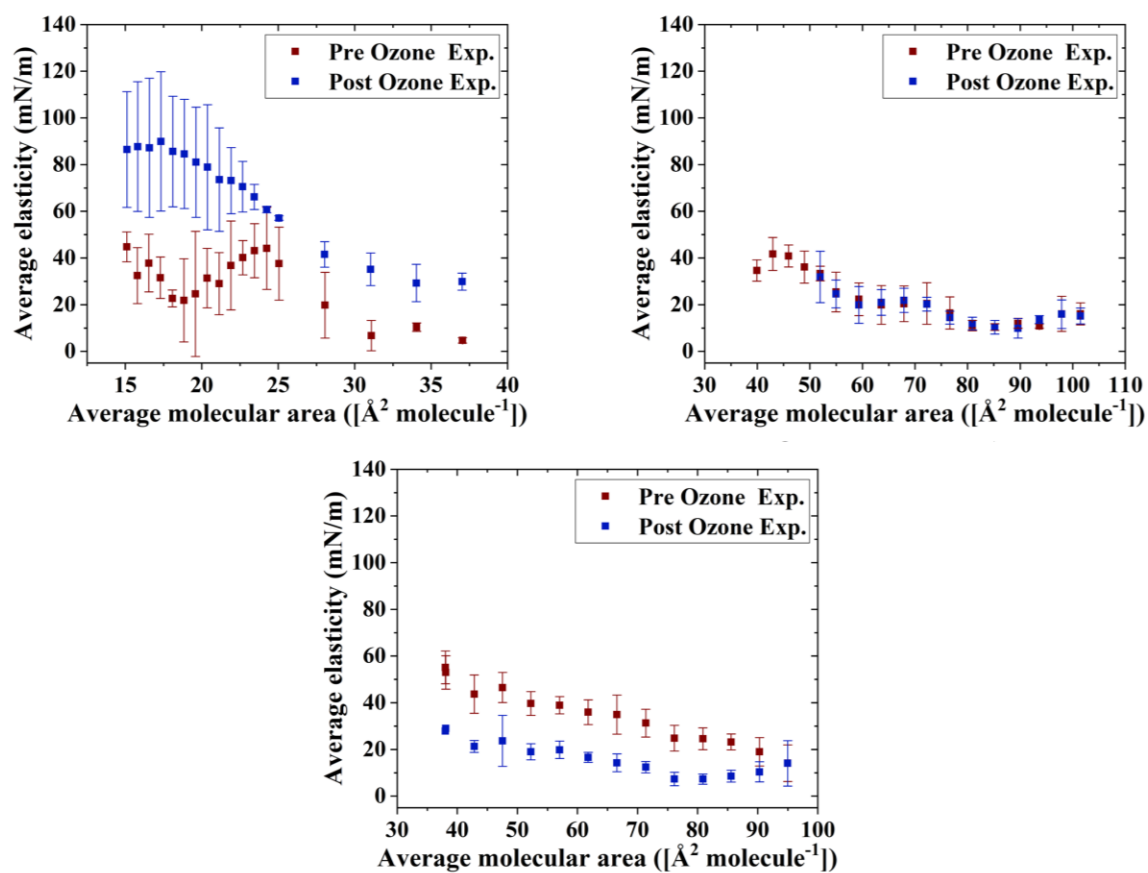
Figure 4.7. Surface dilational elasticity data of CO:PC 90:10 (binary mixture, top, left), CO:GT:PC 40:40:20 (ternary mixture, top, right) and CO:GT:FFA:PC 40:25:15:20 (quaternary mixture, bottom) before ozone exposure (red) and after ozone exposure (blue) on PBS at 22 °C.
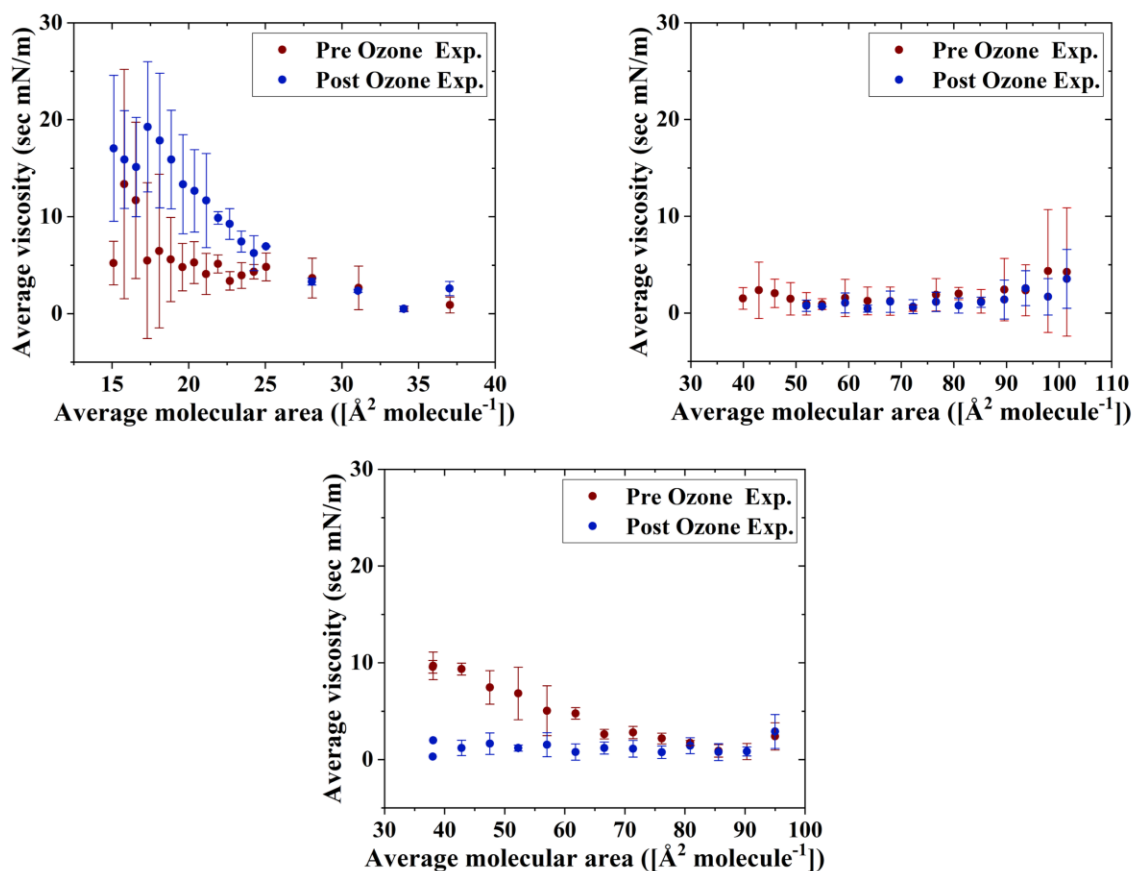
Figure 4.8. Surface dilational viscosity data of CO:PC 90:10 (binary mixture, top, left), CO:GT:PC 40:40:20 (ternary mixture, top, right) and CO:GT:FFA:PC 40:25:15:20 (quaternary mixture, bottom) before ozone exposure (red) and after ozone exposure (blue) on PBS at 22 °C.

4.5. Conclusion

The purpose of this work was to study the impact of exposure to ozone on the mechanical properties of TFLL model membranes. Surface ozone oxidation generated aldehydes, carboxylic acids and in some cases, stable ozonide, hydroxyhydroperoxides and some Criegee intermediates. Ozone exposure leads to an increase in surface pressure as well as an expansion to higher molecular areas in the surface pressure-area isotherms of the TFLL model membranes attributable to the accommodation of the cleaved chains into the film which is most apparent for the binary mixture and less so for the ternary and the quaternary mixtures. This may be due to competing factors impacting the film's surface behaviour. Moreover, the oxidation has a

significant impact on the morphology of all of the TFLL model membranes, fluidizing the binary and ternary mixture films, disrupting the CO condensed phase domain growth and multilayering behaviour, as well as the phase transition of GT. The oxidation of CO, GT, and PC leads to a more unstable film. The presence of FFAs which do not themselves oxidize, impact the line tension and leads to a higher condensed phase surface coverage post oxidation. The impact of ozone oxidation on the film respreadability is strongly correlated with GT content and alteration of the GT envelope transition, which has been shown to be reversible in unoxidized film, adding to the stability of the film. The effect of oxidation on the film elasticity and viscosity is highly dependant on film composition, underlining the importance of using appropriate model membranes.

Thus, it is evident that exposure to high concentrations of ozone induces significant changes in the surface characteristics and behaviour of the TFLL model membranes, impacting their surface activity, morphology, viscoelasticity and stability, all of which are paramount in the proper function of physiological TFLL. The results of this work help shed light on the impact of ozone on TFLL and ocular surface health on which little investigation was done previously. This can aid in better understanding the correlation between a compromised structure of TFLL in DED patients with ozone concentrations in the troposphere layer as well as prevention planning.

Chapter 5. Conclusions & Future Work

The purpose of this thesis research was to determine the impact of the pollutant ozone exposure on the biophysical properties of tear film lipid layer (TFLL) model membranes. First, it was important to investigate the surface characteristics of lipid mixtures with relevant compositions of representatives of important TFLL lipid families i.e. cholesteryl esters, triglycerides, phospholipids, and free fatty acids, with a physiologically relevant non-polar to polar lipid ratio. As understanding the contribution of each component to the biophysical characteristics of TFLL model membranes is important in its own right, in addition to being necessary to investigate how ozone exposure may impact their behaviour. Thus, the first manuscript is dedicated to the study of three TFLL model membranes and an effort was made to glean the possible roles of each component on their distinct surface characteristics, by studying both the individual components as well as the mixtures. The second manuscript is devoted specifically to the detailed study of surface characteristics of cholesteryl oleate film, as an important cholesteryl ester, typically used in TFLL model membrane studies.

The systematic study of the TFLL model membranes led to intriguing results. BAM imaging revealed that CO forms a condensed phase quite early in its compression and also forms multilayers at higher surface pressures. This CO phase behaviour was interestingly retained in the mixtures, leading to non-ideal mixing through molecular area decrease in the binary mixture, but increased molecular area in the ternary and quaternary mixtures where multilayering is not observed in BAM imaging. Moreover, CO also increased the hysteresis observed in the compression-expansion cycles of the binary mixture and produced less reproducible viscoelasticity measurement results. Thus, although the CO proportion in the binary mixture is higher than physiologically occurring in natural meibum (90% vs. 60%) [1,8,11,19,22,28,29], its comparison with the ternary and quaternary mixtures has helped in gleaning the possible impact of cholesteryl esters and phospholipids in physiological TFLL.

In the more detailed study of the two-dimensional CO crystalline structure, outlined in the second manuscript in this thesis, GIXD revealed that the crystallinity of the CO film structure is rooted in the cholesterol ring-packing and not the interdigitation of its chains as is typically observed with saturated acyl chains of cholesteryl esters [159]. Additionally, the crystalline areas of the CO film led to more prominent intensity observed at higher surface pressures, corroborating

the assumption that the proportion of the crystalline film increases as molecular area decreases. However, XR and GIXOS indicate that the CO film forms a flat film and not multilayers at surface pressures below that of its phase transition, emphasising that the multilayering behaviour of CO may only be observed at higher surface pressures than 8 mNm^{-1}. Thus, future XR and GIXOS measurements of the CO film should focus on higher surface pressures to better understand the multilayering behaviour of the film. The condensing and multilayering behaviour of CO are physiologically relevant, as it was previously suggested that the meibum film may reach areas corresponding with multilayering [8,19,43–48] (59 Å^2-9.7 Å^2). As similar molecular areas were observed in the binary mixture, the multilayering behaviour observed in the natural meibum film may be partly attributed to the non-polar cholesteryl esters.

The study of the TFLL model membranes in the first manuscript also revealed possible roles for other important representative lipids. BAM imaging revealed that the addition of phospholipid PC to the binary mixture, induced phase transitions as well as multilayering of the CO at lower surface pressures than their onset on the individual CO film. This impact has been observed previously with cholesteryl nervonate (CN) [61] where the PC-PC and CO-CO interactions dominating the CO-PC interdigitation were suggested as the cause of less homogenous multilayer formation than for CO alone. This indicates that the packing of the polar phospholipids of meibum, creates an overall more stable TFLL, while retaining the multilayer formation of the non-polar cholesteryl esters. Additionally, it was observed that the GT envelope phase transition to a bulk phase is also retained in the mixtures, indicating a lack of mixing of the components. The compression-expansion cycles revealed that the ternary mixture is the most respreadable film of the three TFLL model membranes with the lowest hysteresis observed. This indicates that the reversible GT envelope transition is responsible for the increased stability of the film. This has implications for the physiological role of triglycerides in natural TFLL. The respreading of the physiological TFLL is paramount in the blinking function and the respreading of the TFLL upon blinking and there is evidence in this work that triglycerides of TFLL play a part in it. The addition of FFAs lead to increased deviation from ideal behaviour in the quaternary mixture, as well as increased viscosity to higher levels than reported for extracted meibum film [47]. Moreover, the saturated acyl chains of FFAs reduced the respreability of the film. Thus, while the FFAs can easily be incorporated in the TFLL film, this highlights the importance of finetuning their proportion in TFLL model membranes, in order to best duplicate

the behaviour of physiological TFLL as it was the ternary and not the quaternary mixture that best achieved this in this work, in terms of respreadability and rheology.

Thus, the results of the first and second manuscripts are valuable in understanding the role of each component in the TFLL composition, structure and function relationship. In order to further study the phase behaviour and the crystallinity of the three TFLL model membranes studied in this work, GIXD analysis must be performed with the mixed lipid model membranes to determine how the CO multilayering impacts the mixture films' structure and lateral ordering. Moreover, XR analysis of the films will be quite helpful at higher surface pressures of the films, to understand the multilayer thickness and vertical structure of the three model membrane films. Atomic force microscopy (AFM) would also be a valuable additional analysis to achieve this. Additionally, the addition of OAHFAs as another important class of polar TFLL lipids is essential to take another step towards a physiologically relevant TFLL model membrane.

After the study of the biophysical properties of the three TFLL model membranes and better understanding of the components' roles, the impact of ozone exposure on these films was investigated. The surface ozonolysis yielded aldehydes, carboxylic acids as well as stable ozonide, hydroxyhydroperoxides and some Criegee intermediates. The observance of the latter was not expected and demonstrates that these intermediates are long-lived in the surface environment. The mechanism behind this stability is not known and must be investigated. The compression isotherms of the mixtures showed a surface pressure increase as well as an expansion to higher molecular areas as the result of the accommodation of the cleaved unsaturated chains in the films. This impact is most prominent in the binary mixture. BAM images revealed significant morphological changes on the TFLL model membrane films. The most prominent of these morphological changes was observed in the case of the binary and the ternary mixtures where they were quite fluidized compared to their unoxidized equivalents. Moreover, the CO condensed phase domain formation and growth behaviour as well as its multilayering, implied to be an important behaviour in the first and second manuscript in TFLL film function, were disrupted due to oxidation by ozone. Very significantly, BAM images revealed that the reversible envelope transition of GT to a bulk phase, discovered to be important in the stability and rerpreadability of the TFLL film, was also disrupted after ozone exposure. However, while the quaternary mixture film became less surface active after oxidation, it showed

a higher coverage of CO condensed phase which points to the impact of the FFAs with saturated acyl chains. As the fluidization of the films also points to the PC oxidation reducing the film's stability, these two factors both reflects a less stable and respreadable ternary film, as observed in the results of the compression-expansion cycles. While all films showed reduced hysteresis upon ozone oxidation, it was only the respreadability of the ternary mixture that was reduced significantly as a result of the GT phase transition disruption, as little impact was observed on the binary and quaternary mixtures' respreadability. This result also further consolidates the result of the first manuscript regarding the impact of triglycerides on the TFLL stability. Quite significantly, differing changes were observed on the viscoelasticity of the films upon ozone exposure. While the increase in the surface pressure of the binary mixture after oxidation has led to increased viscoelasticity, The seemingly negligible impact of oxidation on the rheology of the ternary and the reduction of the viscoelasticity of the quaternary mixture film after oxidation, point to competing factors playing their parts in the intermolecular interactions.

Further analysis of the ozone exposure impact on the TFLL model membranes must be performed to further dissect each effect. Atomic force microscopy (AFM) must be done in order to compare the films' thicknesses before and after ozone exposure, which in turn can help understand the exact impact of oxidation on the multilayer formation and their thickness. Additionally, GIXD analysis of the films would aid in shedding light on the ozone exposure effect on the crystallinity and lateral ordering of the films. XR studies of the films would be a helpful additional tool in the study of ozone impact on multilayer formation of the films and their thickness.

Previous studies have associated other airborne pollutants with DED prevalence [68,71]. Using the approach developed in this work, this investigation can be expanded to include NO_x, particulate matter and VOCs.

To generalize the results outlined in this research, possible roles for each of the studied representative lipids of TFLL model membranes were deduced as to the function of a healthy physiological TFLL which were significantly impacted by exposure to ozone. Thus these are strong implications that the high concentrations of ground-level ozone negatively impact the composition, structure and function of the TFLL which is in direct contact with the environment.

These findings provide mechanical and biophysical results to further explain the correlation between the prevalence of DED with higher ozone concentrations. The investigation of possible remedies for DED has been a subject of great interest, especially in the recent years [177–183]. These remedies range from oral medication [177] to topical eye-drop formulations [178–183]. Eye drop formulations typically contain several components each with different purposes such as surface lubrication and humectation, osmotic stress balancing, stabilization of the formulation as well as lipids such as castor oil, flaxseed oil and mineral oil to help in the stabilization of the TFLL [179]. Recently, the use of antioxidant species such as tocopherol acetate (vitamin E) and polyphenols has been suggested in eye drop solutions with fairly significant success [178,180]. Thus, the results of this thesis can help in better understanding the impact of atmospheric pollutants on the blinking function of TFLL and DED emergence which can in turn, aid in more effective formulations of eye drop solutions targeted at DED.

References

1. Cwiklik, L. Tear film lipid layer: A molecular level view. *Biochim. Biophys. Acta - Biomembr.* **1858**, 2421–2430 (2016).

2. Wolff, E. & Last, R. J. *Anatomy of the Eye and Orbit*. (Lewis, 1933).

3. McCulley, J. P., Shine, W. & Smith, R. E. A compositional based model for the tear film lipid layer. *Trans. Am. Ophthalmol. Soc.* **95**, 79–93 (1997).

4. King-Smith, P. E., Fink, B. A., Hill, R. M., Koelling, K. W. & Tiffany, J. M. The thickness of the tear film. *Curr. Eye Res.* **29**, 357–368 (2004).

5. Zhou, L. & Beuerman, R. W. Tear analysis in ocular surface diseases. *Prog. Retin. Eye Res.* **31**, 527–550 (2012).

6. Miller, D. Measurement of the Surface Tension of Tears. *Arch. Ophthalmol.* **82**, 368–371 (1969).

7. King-Smith, P. E., Bailey, M. D. & Braun, R. J. Four characteristics and a model of an effective tear film lipid layer (tfll). *Ocul. Surf.* **11**, 236–245 (2013).

8. Georgiev, G. A., Eftimov, P. & Yokoi, N. Structure-function relationship of tear film lipid layer: A contemporary perspective. *Exp. Eye Res.* **163**, 17–28 (2017).

9. Bron, A. J., Tiffany, J. M., Gouveia, S. M., Yokoi, N. & Voon, L. W. Functional aspects of the tear film lipid layer. *Exp. Eye Res.* **78**, 347–360 (2004).

10. Forrester, J. V, Dick, A. D., McMenamin, P. G., Roberts, F. & Pearlman, E. *The eye e-book: basic sciences in practice*. (Elsevier Health Sciences, 2020).

11. Millar, T. J. & Schuett, B. S. The real reason for having a meibomian lipid layer covering the outer surface of the tear film - A review. *Exp. Eye Res.* **137**, 125–138 (2015).

12. Olyńskaż, A., Wizert, A., Štefl, M., Iskander, D. R. & Cwiklik, L. Mixed polar-nonpolar lipid films as minimalistic models of Tear Film Lipid Layer: A Langmuir trough and

fluorescence microscopy study. *Biochim. Biophys. Acta - Biomembr.* **1862**, (2020).

13. Green-Church, K. B. *et al.* The international workshop on meibomian gland dysfunction: Report of the subcommittee on tear film lipids and lipid-protein interactions in health and disease. *Investig. Ophthalmol. Vis. Sci.* **52**, 1979–1993 (2011).

14. Ewen King-Smith, P., Hinel, E. A. & Nichols, J. J. Application of a novel interferometric method to investigate the relation between lipid layer thickness and tear film thinning. *Investig. Ophthalmol. Vis. Sci.* **51**, 2418–2423 (2010).

15. Butovich, I. A. On the lipid composition of human meibum and tears: Comparative analysis of nonpolar lipids. *Investig. Ophthalmol. Vis. Sci.* **49**, 3779–3789 (2008).

16. Kulovesi, P. *et al.* The impact of lipid composition on the stability of the tear fluid lipid layer. *Soft Matter* **8**, 5826–5834 (2012).

17. Kulovesi, P. *et al.* Molecular organization of the tear fluid lipid layer. *Biophys. J.* **99**, 2559–2567 (2010).

18. Rantamäki, A. H., Telenius, J., Koivuniemi, A., Vattulainen, I. & Holopainen, J. M. Lessons from the biophysics of interfaces: Lung surfactant and tear fluid. *Prog. Retin. Eye Res.* **30**, 204–215 (2011).

19. Butovich, I. A. Tear film lipids. *Exp. Eye Res.* **117**, 4–27 (2013).

20. Haworth, K. M., Nichols, J. J., Thangavelu, M., Sinnott, L. T. & Nichols, K. K. Examination of human meibum collection and extraction techniques. *Optom. Vis. Sci. Off. Publ. Am. Acad. Optom.* **88**, 525 (2011).

21. Butovich, I. A., Lu, H., McMahon, A. & Eule, J. C. Toward an animal model of the human tear film: biochemical comparison of the mouse, canine, rabbit, and human meibomian lipidomes. *Invest. Ophthalmol. Vis. Sci.* **53**, 6881–6896 (2012).

22. Butovich, I. A. The Meibomian Puzzle: Combining pieces together. *Prog. Retin. Eye Res.* **28**, 483–498 (2009).

23. Nichols, K. K., Ham, B. M., Nichols, J. J., Ziegler, C. & Green-Church, K. B. Identification of fatty acids and fatty acid amides in human meibomian gland secretions. *Investig. Ophthalmol. Vis. Sci.* **48**, 34–39 (2007).

24. Pucker, A. D. & Haworth, K. M. The presence and significance of polar meibum and tear lipids. *Ocul. Surf.* **13**, 26–42 (2015).

25. Georgiev, G. A. Controversies regarding the role of polar lipids in human and animal tear film lipid layer. *Ocul. Surf.* **3**, 176–178 (2015).

26. Lam, S. M. *et al.* Extensive characterization of human tear fl uid collected using different techniques unravels the presence of novel lipid amphiphiles. *J. Lipid Res.* **55**, 289–298 (2014).

27. Lam, S. M. *et al.* Lipidomic analysis of human tear fluid reveals structure-specific lipid alterations in dry eye syndrome. *J. Lipid Res.* **55**, 299–306 (2014).

28. McCulley, J. P. & Shine, W. E. The lipid layer: The outer surface of the ocular surface tear film. *Biosci. Rep.* **21**, 407–418 (2001).

29. Pucker, A. D. & Nichols, J. J. Analysis of meibum and tear lipids. *Ocul. Surf.* **10**, 230–250 (2012).

30. Brown, S. H. J. *et al.* A comparison of patient matched meibum and tear lipidomes. *Investig. Ophthalmol. Vis. Sci.* **54**, 7417–7423 (2013).

31. Mathers, W. D. & Lane, J. A. Meibomian gland lipids, evaporation, and tear film stability. *Lacrimal Gland. Tear Film. Dry Eye Syndr. 2* 349–360 (1998).

32. Nicolaides, N. *et al.* Meibomian gland studies: comparison of steer and human lipids. *Investig. Ophthalmol. Vis. Sci.* **20**, 522–536 (1981).

33. Schuett, B. S. & Millar, T. J. An investigation of the likely role of (O-acyl) ω-hydroxy fatty acids in meibomian lipid films using (O-oleyl) ω-hydroxy palmitic acid as a model. *Exp. Eye Res.* **115**, 57–64 (2013).

34. Rantamäki, A. H., Seppänen-Laakso, T., Oresic, M., Jauhiainen, M. & Holopainen, J. M. Human tear fluid lipidome: From composition to function. *PLoS One* **6**, 1–7 (2011).

35. McMahon, A., Lu, H. & Butovich, I. A. The spectrophotometric sulfo-phospho-vanillin assessment of total lipids in human meibomian gland secretions. *Lipids* **48**, 513–525 (2013).

36. Ong, B.-L., Hodson, S. A., Wigham, T., Miller, F. & Larke, J. R. Evidence for keratin proteins in normal and abnormal human meibomian fluids. *Curr. Eye Res.* **10**, 1113–1119 (1991).

37. Borchman, D., Yappert, M. C. & Foulks, G. N. Changes in human meibum lipid with meibomian gland dysfunction using principal component analysis. *Exp. Eye Res.* **91**, 246–256 (2010).

38. Tsai, P. S. *et al.* Proteomic analysis of human meibomian gland secretions. *Br. J. Ophthalmol.* **90**, 372–377 (2006).

39. Miano, F., Calcara, M., Millar, T. J. & Enea, V. Insertion of tear proteins into a meibomian lipids film. *Colloids Surfaces B Biointerfaces* **44**, 49–55 (2005).

40. Ma, P., Wang, N., McKown, R. L., Raab, R. W. & Laurie, G. W. Focus on molecules: lacritin. *Exp. Eye Res.* **86**, 457 (2008).

41. Tiffany, J. M., Todd, B. S. & Baker, M. R. Calculation of the exposed area of the human eye. in *Investigative Ophthalmology & Visual Science* vol. 38 766 (LIPPINCOTT-RAVEN PUBL 227 EAST WASHINGTON SQ, PHILADELPHIA, PA 19106, 1997).

42. Petrov, P. G. *et al.* Two-dimensional order in mammalian pre-ocular tear film. *Exp. Eye Res.* **84**, 1140–1146 (2007).

43. Leiske, D. L. *et al.* Molecular structure of interfacial human meibum films. *Langmuir* **28**, 11858–11865 (2012).

44. Leiske, D. L. *et al.* Temperature-induced transitions in the structure and interfacial

rheology of human meibum. *Biophys. J.* **102**, 369–376 (2012).

45. Rosenfeld, L. *et al.* Structural and rheological properties of meibomian lipid. *Investig. Ophthalmol. Vis. Sci.* **54**, 2720–2732 (2013).

46. Lu, H., Wojtowicz, J. C. & Butovich, I. A. Differential scanning calorimetric evaluation of human meibomian gland secretions and model lipid mixtures: Transition temperatures and cooperativity of melting. *Chem. Phys. Lipids* **170**–**171**, 55–64 (2013).

47. Raju, S. R., Palaniappan, C. K., Ketelson, H. A., Davis, J. W. & Millar, T. J. Interfacial dilatational viscoelasticity of human meibomian lipid films. *Curr. Eye Res.* **38**, 817–824 (2013).

48. Georgiev, G. A. *et al.* Surface relaxations as a tool to distinguish the dynamic interfacial properties of films formed by normal and diseased meibomian lipids. *Soft Matter* **10**, 5579–5588 (2014).

49. Mudgil, P. & Millar, T. J. Surfactant properties of human meibomian lipids. *Investig. Ophthalmol. Vis. Sci.* **52**, 1661–1670 (2011).

50. Holly, F. J. Surface chemistry of tear film component analogs. *J. Colloid Interface Sci.* **49**, 221–231 (1974).

51. Langmuir, I. & Schaefer, V. J. Rates of evaporation of water through compressed monolayers on water. *J. Franklin Inst.* **235**, 119–162 (1943).

52. Rantamäki, A. H., Javanainen, M., Vattulainen, I. & Holopainen, J. M. Do lipids retard the evaporation of the tear fluid? *Investig. Ophthalmol. Vis. Sci.* **53**, 6442–6447 (2012).

53. Kulovesi, P., Rantamäki, A. H. & Holopainen, J. M. Surface properties of artificial tear film lipid layers: Effects of wax esters. *Investig. Ophthalmol. Vis. Sci.* **55**, 4448–4454 (2014).

54. Xu, X., Li, G. & Zuo, Y. Y. Biophysical properties of tear film lipid layer I. Surface tension and surface rheology. *Biophys. J.* **121**, 439–450 (2022).

55.   Millar, T. J. & King-Smith, P. E. Analysis of comparison of human meibomian lipid films and mixtures with cholesteryl esters in vitro films using high resolution color microscopy. *Investig. Ophthalmol. Vis. Sci.* **53**, 4710–4719 (2012).

56.   Dwivedi, M., Brinkkötter, M., Harishchandra, R. K. & Galla, H. J. Biophysical investigations of the structure and function of the tear fluid lipid layers and the effect of ectoine. Part B: Artificial lipid films. *Biochim. Biophys. Acta - Biomembr.* **1838**, 2716–2727 (2014).

57.   Telenius, J., Koivuniemi, A., Kulovesi, P., Holopainen, J. M. & Vattulainen, I. Role of neutral lipids in tear fluid lipid layer: Coarse-grained simulation study. *Langmuir* **28**, 17092–17100 (2012).

58.   Wizert, A., Iskander, D. R. & Cwiklik, L. Organization of lipids in the tear film: A molecular-level view. *PLoS One* **9**, (2014).

59.   Patterson, M., Vogel, H. J. & Prenner, E. J. Biophysical characterization of monofilm model systems composed of selected tear film phospholipids. *Biochim. Biophys. Acta - Biomembr.* **1858**, 403–414 (2016).

60.   Patterson, M., Vogel, H. J. & Prenner, E. J. The effect of repeated lateral compression and expansions mimicking blinking on selected tear film polar lipid monofilms. *Biochim. Biophys. Acta - Biomembr.* **1859**, 319–330 (2017).

61.   Paananen, R. O. *et al.* Interactions of polar lipids with cholesteryl ester multilayers elucidate tear film lipid layer structure. *Ocul. Surf.* (2020) doi:10.1016/j.jtos.2020.06.001.

62.   Craig, J. P. *et al.* TFOS DEWS II Report Executive Summary. *Ocul. Surf.* **15**, 802–812 (2017).

63.   Lemp, M. A., Crews, L. A., Bron, A. J., Foulks, G. N. & Sullivan, B. D. Distribution of aqueous-deficient and evaporative dry eye in a clinic-based patient cohort: a retrospective study. *Cornea* **31**, 472–478 (2012).

64.   Gayton, J. L. Etiology, prevalence, and treatment of dry eye disease. *Clin. Ophthalmol.*

(Auckland, NZ) **3**, 405 (2009).

65. Chan, T. C. Y., Chow, S. S. W., Wan, K. H. N. & Yuen, H. K. L. Update on the association between dry eye disease and meibomian gland dysfunction. *Hong Kong Med. J.* **25**, 38–47 (2019).

66. Moss, S. E., Klein, R. & Klein, B. E. K. Prevalance of and risk factors for dry eye syndrome. *Arch. Ophthalmol.* **118**, 1264–1268 (2000).

67. Lin, P.-Y. *et al.* Prevalence of dry eye among an elderly Chinese population in Taiwan: the Shihpai Eye Study. *Ophthalmology* **110**, 1096–1101 (2003).

68. Yu, D. *et al.* Air Pollutants are associated with Dry Eye Disease in Urban Ophthalmic Outpatients: A Prevalence Study in China. *J. Transl. Med.* **17**, 1–9 (2019).

69. Schaumberg, D. A., Sullivan, D. A., Buring, J. E. & Dana, M. R. Prevalence of dry eye syndrome among US women. *Am. J. Ophthalmol.* **136**, 318–326 (2003).

70. Mo, Z. *et al.* Impacts of air pollution on dry eye disease among residents in Hangzhou, China: A case-crossover study. *Environ. Pollut.* **246**, 183–189 (2019).

71. Ashraf, A., Butt, A., Khalid, I., Alam, R. U. & Ahmad, S. R. Smog analysis and its effect on reported ocular surface diseases: A case study of 2016 smog event of Lahore. *Atmos. Environ.* **198**, 257–264 (2019).

72. Hwang, S. H. *et al.* Potential importance of ozone in the association between outdoor air pollution and dry eye disease in South Korea. *JAMA Ophthalmol.* **134**, 503–510 (2016).

73. Caffery, B. *et al.* Prevalence of dry eye disease in Ontario, Canada: A population-based survey. *Ocul. Surf.* **17**, 526–531 (2019).

74. McCarty, C. A., Bansal, A. K., Livingston, P. M., Stanislavsky, Y. L. & Taylor, H. R. The epidemiology of dry eye in Melbourne, Australia. *Ophthalmology* **105**, 1114–1119 (1998).

75. Lee, A. J. *et al.* Prevalence and risk factors associated with dry eye symptoms: a population based study in Indonesia. *Br. J. Ophthalmol.* **86**, 1347–1351 (2002).

76. Shimmura, S., Shimazaki, J. & Tsubota, K. Results of a population-based questionnaire on the symptoms and lifestyles associated with dry eye. *Cornea* **18**, 408–411 (1999).

77. Yu, J., Asche, C. V & Fairchild, C. J. The economic burden of dry eye disease in the United States: a decision tree analysis. *Cornea* **30**, 379–387 (2011).

78. McDonald, M., Patel, D. A., Keith, M. S. & Snedecor, S. J. Economic and humanistic burden of dry eye disease in Europe, North America, and Asia: a systematic literature review. *Ocul. Surf.* **14**, 144–167 (2016).

79. Daniel Nelson, J. *et al.* The international workshop on meibomian gland dysfunction: Report of the definition and classification subcommittee. *Investig. Ophthalmol. Vis. Sci.* **52**, 1930–1937 (2011).

80. Arita, R. *et al.* Meibum color and free fatty acid composition in patients with meibomian gland dysfunction. *Investig. Ophthalmol. Vis. Sci.* **56**, 4403–4412 (2015).

81. Butovich, I. A. *et al.* Biophysical and morphological evaluation of human normal and dry eye meibum using hot stage polarized light microscopy. *Investig. Ophthalmol. Vis. Sci.* **55**, 87–101 (2013).

82. Lam, S. M. *et al.* Meibum lipid composition in Asians with dry eye disease. *PLoS One* **6**, (2011).

83. Guillon, M. Tear film examination of the contact lens patient. *OPTICIAN-SUTTON-* **206**, 21 (1993).

84. Doane, M. G. An instrument for in vivo tear film interferometry. *Optom. Vis. Sci. Off. Publ. Am. Acad. Optom.* **66**, 383–388 (1989).

85. Korb, D. R. *et al.* Tear film lipid layer thickness as a function of blinking. *Cornea* **13**, 354–359 (1994).

86. Yokoi, N., Takehisa, Y. & Kinoshita, S. Correlation of tear lipid layer interference patterns with the diagnosis and severity of dry eye. *Am. J. Ophthalmol.* **122**, 818–824

(1996).

87. Tomlinson, A. *et al.* ✔The international workshop on meibomian gland dysfunction: Report of the diagnosis subcommittee. *Investig. Ophthalmol. Vis. Sci.* **52**, 2006–2049 (2011).

88. Danjo, Y. & Hamano, T. Observation of precorneal tear film in patients with Sjögren's syndrome. *Acta Ophthalmol. Scand.* **73**, 501–505 (1995).

89. Di Pascuale, M. A., Goto, E. & Tseng, S. C. G. Sequential changes of lipid tear film after the instillation of a single drop of a new emulsion eye drop in dry eye patients. *Ophthalmology* **111**, 783–791 (2004).

90. Tiffany, J. M., Winter, N. & Bliss, G. Tear film stability and tear surface tension. *Curr. Eye Res.* **8**, 507–515 (1989).

91. Nagyová, B. & Tiffany, J. M. Components responsible for the surface tension of human tears. *Curr. Eye Res.* **19**, 4–11 (1999).

92. Butovich, I. A., Wilkerson, A., Bhat, N., McMahon, A. & Yuksel, S. On the pivotal role of Elovl3/ELOVL3 in meibogenesis and ocular physiology of mice. *FASEB J.* **33**, 10034–10048 (2019).

93. Miyamoto, M., Sassa, T., Sawai, M. & Kihara, A. Lipid polarity gradient formed by ω-hydroxy lipids in tear film prevents dry eye disease. *Elife* **9**, 1–22 (2020).

94. Sassa, T., Tadaki, M., Kiyonari, H. & Kihara, A. Very long-chain tear film lipids produced by fatty acid elongase ELOVL1 prevent dry eye disease in mice. *FASEB J.* **32**, 2966–2978 (2018).

95. Selladurai, S. Airborne Pollutants and Lung Surfactant: Biophysical Impacts of Surface Oxidation Reactions. (2015).

96. Jacob, D. J. Heterogeneous chemistry and tropospheric ozone. *Atmos. Environ.* **34**, 2131–2159 (2000).

97. Finlayson-Pitts, B. J. & Pitts, J. N. Tropospheric air pollution: Ozone, airborne toxics, polycyclic aromatic hydrocarbons, and particles. *Science (80-.).* **276**, 1045–1052 (1997).

98. Crutzen, P. J. Introductory lecture. Overview of tropospheric chemistry: Developments during the past quarter century and a look ahead. *Faraday Discuss.* **100**, 1–21 (1995).

99. Holton, J. R. *et al.* Stratosphere-troposphere exchange. *Reviews of Geophysics* vol. 33 403–439 (1995).

100. Hough, A. M. & Derwent, R. G. Changes in the global concentration of tropospheric ozone due to human activities. *Nature* **344**, 645–648 (1990).

101. Gomez, A. L., Lewis, T. L., Wilkinson, S. A. & Nizkorodov, S. A. Stoichiometiy of ozonation of environmentally relevant olefins in saturated hydrocarbon solvents. *Environ. Sci. Technol.* **42**, 3582–3587 (2008).

102. Oltmans, S. J. *et al.* Long-term changes in tropospheric ozone. *Atmos. Environ.* **40**, 3156–3173 (2006).

103. Haagen-Smit, A. J. Chemistry and Physiology of Los Angeles Smog. *Ind. Eng. Chem.* **44**, 1342–1346 (1952).

104. Ma, J., Xu, X., Zhao, C. & Yan, P. A review of atmospheric chemistry research in China: Photochemical smog, haze pollution, and gas-aerosol interactions. *Adv. Atmos. Sci.* **29**, 1006–1026 (2012).

105. Künzli, N. *et al.* Association between lifetime ambient ozone exposure and pulmonary function in college freshmen—results of a pilot study. *Environ. Res.* **72**, 8–23 (1997).

106. Tager, I. B. *et al.* Chronic exposure to ambient ozone and lung function in young adults. *Epidemiology* 751–759 (2005).

107. Jerrett, M. *et al.* Long-term ozone exposure and mortality. *N. Engl. J. Med.* **360**, 1085–1095 (2009).

108. Galor, A., Kumar, N., Feuer, W. & Lee, D. J. Environmental factors affect the risk of dry

eye syndrome in a United States veteran population. *Ophthalmology* **121**, 972–974 (2014).

109. Ong, E. S. *et al.* Longitudinal examination of frequency of and risk factors for severe dry eye symptoms in us veterans. *JAMA Ophthalmol.* **135**, 116–123 (2017).

110. Kumar, N., Feuer, W., Lanza, N. L. & Galor, A. Seasonal Variation in Dry Eye. *Ophthalmology* **122**, 1727–1729 (2015).

111. Fu, Q. *et al.* Air pollution and outpatient visits for conjunctivitis: A case-crossover study in Hangzhou, China. *Environ. Pollut.* **231**, 1344–1350 (2017).

112. Berg, E. J. *et al.* Climatic and environmental correlates of dry eye disease severity: A report from the dry eye assessment and management (dream) study. *Transl. Vis. Sci. Technol.* **9**, 1–11 (2020).

113. Kim, Y., Choi, Y.-H., Kim, M. K., Paik, H. J. & Kim, D. H. Different adverse effects of air pollutants on dry eye disease: Ozone, PM2.5, and PM10. *Environ. Pollut.* **265**, 115039 (2020).

114. Lee, H., Kim, E. K., Kim, H. Y. & Kim, T. I. Effects of exposure to ozone on the ocular surface in an experimental model of allergic conjunctivitis. *PLoS One* **12**, 1–18 (2017).

115. Li, J. & Kang, M. *The Correlation Between Atmospheric Conditions and Clinical Dry Eye. (2022).

116. Lee, H. *et al.* Effects of ozone exposure on the ocular surface. *Free Radic. Biol. Med.* **63**, 78–89 (2013).

117. Hao, R. *et al.* The effects of short-term and long-term air pollution exposure on meibomian gland dysfunction. *Sci. Rep.* **12**, 1–14 (2022).

118. Georgiev, G. A., Borchman, D., Eftimov, P. & Yokoi, N. Lipid saturation and the rheology of human tear lipids. *Int. J. Mol. Sci.* **20**, (2019).

119. Criegee, R. Mechanism of Ozonolysis. *Angew. Chemie Int. Ed. English* **14**, 745–752 (1975).

120. Pryor, W. A., Das, B. & Church, D. F. The Ozonation of Unsaturated Fatty Acids: Aldehydes and Hydrogen Peroxide as Products and Possible Mediators of Ozone Toxicity. *Chem. Res. Toxicol.* **4**, 341–348 (1991).

121. Krisyuk, B. E., Maiorov, A. V. & Popov, A. A. Kinetics and mechanism of ozone addition to olefins and dienes. *Kinet. Catal.* **57**, 326–332 (2016).

122. Neeb, P., Sauer, F., Horie, O. & Moortgat, G. K. Formation of hydroxymethyl hydroperoxide and formic acid in alkene ozonolysis in the presence of water vapour. *Atmos. Environ.* **31**, 1417–1423 (1997).

123. Paananen, R. O., Rantamäki, A. H., Parshintsev, J. & Holopainen, J. M. The effect of ambient ozone on unsaturated tear film wax esters. *Investig. Ophthalmol. Vis. Sci.* **56**, 8054–8062 (2015).

124. Pockels, A. Surface tension. *Nature* **43**, 437–439 (1891).

125. Langmuir, I. The constitution and fundamental properties of solids and liquids. II. Liquids. *J. Am. Chem. Soc.* **39**, 1848–1906 (1917).

126. Adamson, A. W. & Gast, A. P. Electrical aspects of surface chemistry. *Phys. Chem. surfaces* **4**, 185–229 (1997).

127. Kaganer, V. M., Möhwald, H. & Dutta, P. Structure and phase transitions in- Langmuir monolayers. *Rev. Mod. Phys.* **71**, 779–819 (1999).

128. Kim, K., Choi, S. Q., Zasadzinski, J. A. & Squires, T. M. Interfacial microrheology of DPPC monolayers at the air-water interface. *Soft Matter* **7**, 7782–7789 (2011).

129. Wüstneck, N., Wüstneck, R., Fainerman, V. B., Miller, R. & Pison, U. Interfacial behaviour and mechanical properties of spread lung surfactant protein/lipid layers. *Colloids Surfaces B Biointerfaces* **21**, 191–205 (2001).

130. Conway, J. W. The Surface Activity And Rheological Changes Induced In Lung Surfactant Resulting From Ozone Exposure. *Thesis* (2009).

131. Vrânceanu, M., Winkler, K., Nirschl, H. & Leneweit, G. Surface rheology of monolayers of phospholipids and cholesterol measured with axisymmetric drop shape analysis. *Colloids Surfaces A Physicochem. Eng. Asp.* **311**, 140–153 (2007).

132. Krägel, J. *et al.* Surface rheology of monolayers. *Thin Solid Films* **284**, 361–364 (1996).

133. Miller, R., Wüstneck, R., Krägel, J. & Kretzschmar, G. Dilational and shear rheology of adsorption layers at liquid interfaces. *Colloids Surfaces A Physicochem. Eng. Asp.* **111**, 75–118 (1996).

134. D Moebius, R. M. *Novel methods to study interfacial layers*. (Elsevier, 2001).

135. Leser, M. E., Acquistapace, S., Cagna, A., Makievski, A. V. & Miller, R. Limits of oscillation frequencies in drop and bubble shape tensiometry. *Colloids Surfaces A Physicochem. Eng. Asp.* **261**, 25–28 (2005).

136. Wüstneck, R. *et al.* Interfacial properties of pulmonary surfactant layers. *Adv. Colloid Interface Sci.* **117**, 33–58 (2005).

137. Veldhuizen, E. J. A. & Haagsman, H. P. Role of pulmonary surfactant components in surface film formation and dynamics. *Biochim. Biophys. Acta - Biomembr.* **1467**, 255–270 (2000).

138. Kaercher, T., Hönig, D. & Möbius, D. Brewster angle microscopy - A new method of visualizing the spreading of Meibomian lipids. *Int. Ophthalmol.* **17**, 341–348 (1993).

139. Stefaniu, C. & Brezesinski, G. Grazing incidence X-ray diffraction studies of condensed double-chain phospholipid monolayers formed at the soft air/water interface. *Adv. Colloid Interface Sci.* **207**, 265–279 (2014).

140. A. Guinier. Imperfect Crystals and Amorphous Bodies. *W. H. Free. Co* **19**, 313–314 (1964).

141. Behyan, S. *et al.* Nanoparticle-induced structural changes in lung surfactant membranes: An X-ray scattering study. *Environ. Sci. Nano* **5**, 1218–1230 (2018).

142. Kjaer, K. 4-Some Simple Ideas on XR & GIXD from thin surfactant films. (1994).

143. Parratt, L. G. Surface studies of solids by total reflection of x-rays. *Phys. Rev.* **95**, 359–369 (1954).

144. Dai, Y. *et al.* Synchrotron X-ray studies of rapidly evolving morphology of self-assembled nanoparticle films under lateral compression. *Langmuir* vol. 29 14050–14056 (2013).

145. Stenger, P. C. *et al.* X-ray diffraction and reflectivity validation of the depletion attraction in the competitive adsorption of lung surfactant and albumin. *Biophys. J.* **97**, 777–786 (2009).

146. Dai, Y. *et al.* A comparative study of Langmuir surfactant films: Grazing incidence x-ray off-specular scattering vs. x-ray specular reflectivity. *J. Appl. Phys.* **110**, (2011).

147. Bu, W. *et al.* X-ray studies of interfacial strontium-extractant complexes in a model solvent extraction system. vol. 118 12486–12500 (2014).

148. You, S. S. *et al.* Liquid Surface X-ray Studies of Gold Nanoparticle-Phospholipid Films at the Air/Water Interface. **120**, 9132–9141 (2016).

149. Nagyova, B. & Tiffany, J. M. Components responsible for the surface tension of human tears. *Curr. Eye Res.* **19**, 4–11 (1999).

150. Benjamins, J., Cagna, A. & Lucassen-Reynders, E. H. Viscoelastic properties of triacylglycerol/water interfaces covered by proteins. *Colloids Surfaces A Physicochem. Eng. Asp.* **114**, 245–254 (1996).

151. Monteux, C., Fuller, G. G. & Bergeron, V. Shear and dilational surface rheology of oppositely charged polyelectrolyte/surfactant microgels adsorbed at the air-water interface. influence on foam stability. *J. Phys. Chem. B* **108**, 16473–16482 (2004).

152. Miano, F., Winlove, C. P., Lambusta, D. & Marletta, G. Viscoelastic properties of insoluble amphiphiles at the air/water interface. *J. Colloid Interface Sci.* **296**, 269–275 (2006).

153. Islam, A., Rahaman, N. & Ahad, M. A study on tiredness assessment by using eye blink detection. *J. Kejuruter.* **31**, 209–214 (2019).

154. Gradella Villalva, D. *et al.* Molecular Packing in Langmuir Monolayers Composed of a Phosphatidylcholine and a Pyrene Lipid. *J. Phys. Chem. B* **120**, 1126–1133 (2016).

155. Vollhardt, D. Effect of unsaturation in fatty acids on the main characteristics of langmuir monolayers. *J. Phys. Chem. C* **111**, 6805–6812 (2007).

156. McFate, C., Ward, D. & Olmsted, J. Organized Collapse of Fatty Acid Monolayers. *Langmuir* **9**, 1036–1039 (1993).

157. Oliveira, O. N., Taylor, D. M. & Morgan, H. Modelling the surface potential-area dependence of a stearic acid monolayer. *Thin Solid Films* **210**–**211**, 76–78 (1992).

158. Smaby, J. M. & Brockman, H. L. Novel Surface Phase Containing Cholesteryl Esters. 1. Structural Characteristics Determined from Surface Pressure-Area Measurements. *Biochemistry* **20**, 718–723 (1981).

159. Alonso, C. *et al.* Self-assembly of crystalline films of interdigitated long-chain cholesteryl esters at the air-water interface. *J. Phys. Chem. B* **105**, 8563–8568 (2001).

160. Mitsche, M. A., Wang, L. & Small, D. M. Adsorption of egg phosphatidylcholine to an air/water and triolein/water bubble interface: Use of the 2-dimensional phase rule to estimate the surface composition of a phospholipid/triolein/water surface as a function of surface pressure. *J. Phys. Chem. B* **114**, 3276–3284 (2010).

161. Yoshida, M. *et al.* Role of Endogenous Ingredients in Meibum and Film Structures on Stability of the Tear Film Lipid Layer against Lateral Compression. *Langmuir* **35**, 8445–8451 (2019).

162. Leiske, D. L., Raju, S. R., Ketelson, H. A., Millar, T. J. & Fuller, G. G. The interfacial viscoelastic properties and structures of human and animal Meibomian lipids. *Exp. Eye Res.* **90**, 598–604 (2010).

163. Pérez-gil, J. Structure of pulmonary surfactant membranes and films : The role of proteins and lipid – protein interactions. **1778**, 1676–1695 (2008).

164. Zuo, Y. Y., Veldhuizen, R. A. W., Neumann, A. W., Petersen, N. O. & Possmayer, F. Current perspectives in pulmonary surfactant - Inhibition, enhancement and evaluation. *Biochim. Biophys. Acta - Biomembr.* **1778**, 1947–1977 (2008).

165. Wang, Z., Hall, S. B. & Notter, R. H. Dynamic surface activity of films of lung surfactant phospholipids, hydrophobic proteins, and neutral lipids. *J. Lipid Res.* **36**, 1283–1293 (1995).

166. Notter, D. R. H. *Lung surfactants: basic science and clinical applicationsitle. Gastronomía ecuatoriana y turismo local.* vol. 1 (1967).

167. Ivankin, A., Kuzmenko, I. & Gidalevitz, D. Cholesterol-phospholipid interactions: New insights from surface x-ray scattering data. *Phys. Rev. Lett.* **24**, 1–4 (2010).

168. Rapaport, H. *et al.* Cholesterol monohydrate nucleation in ultrathin films on water. *Biophys. J.* **81**, 2729–2736 (2001).

169. Ivankin, A., Kuzmenko, I. & Gidalevitz, D. Cholesterol-phospholipid interactions: New insights from surface x-ray scattering data-Supplementary Material. *Phys. Rev. Lett.* **104**, 1–5 (2010).

170. Lafont, S. *et al.* Monitoring the nucleation of crystalline films of cholesterol on water and in the presence of phospholipid. *J. Phys. Chem. B* **102**, 761–765 (1998).

171. Pryor, W. A. & Church, D. F. Aldehydes, hydrogen peroxide, and organic radicals as mediators of ozone toxicity. *Free Radic. Biol. Med.* **11**, 41–46 (1991).

172. Salgo, M. G., Cueto, R. & Pryor, W. A. Effect of lipid ozonation products on liposomal membranes detected by Laurdan fluorescence. *Free Radic. Biol. Med.* **19**, 609–616 (1995).

173. Santrock, J., Gorski, R. A. & O'Gara, J. F. Products and Mechanism of the Reaction of

Ozone with Phospholipids in Unilamellar Phospholipid Vesicles. *Chem. Res. Toxicol.* **5**, 134–141 (1992).

174. Stegemann, J. P. Time Resolved Studies of Interfacial Reactions of Ozone with Pulmonary Phospholipid Surfactants Using Field Induced Droplet Ionization Mass Spectrometry. *Tissue Eng.* **23**, 1–7 (2007).

175. Wadia, Y., Tobias, D. J., Stafford, R. & Finlayson-Pitts, B. J. Real-time monitoring of the kinetics and gas-phase products of the reaction of ozone with an unsaturated phospholipid at the air-water interface. *Langmuir* vol. 16 9321–9330 (2000).

176. Thompson, K. C. *et al.* Degradation and Rearrangement of a Lung Surfactant Lipid at the Air − Water Interface during Exposure to the Pollutant Gas Ozone. (2013).

177. Blades, K. J., Patel, S. & Aidoo, K. E. Oral antioxidant therapy for marginal dry eye. *Eur. J. Clin. Nutr.* **55**, 589–597 (2001).

178. Li, L. *et al.* Effects of eye drops containing a mixture of 3% diquafosol sodium and tocopherol acetate (vitamin E) on the ocular surface of murine dry eye. *Cutan. Ocul. Toxicol.* **40**, 350–358 (2021).

179. Downie, L. E. *et al.* An artificial tear containing flaxseed oil for treating dry eye disease: A randomized controlled trial. *Ocul. Surf.* **18**, 148–157 (2020).

180. Favero, G., Moretti, E., Krajčíková, K., Tomečková, V. & Rezzani, R. Evidence of polyphenols efficacy against dry eye disease. *Antioxidants* **10**, 1–17 (2021).

181. Saija, M. C. & Cwiklik, L. Interactions of surfactant-coated triglyceride nanodroplets with the tear film lipid layer in the context of dry eye disease. *Biophys. J.* **121**, 489a (2022).

182. Lin, P. H. *et al.* Alleviation of dry eye syndrome with one dose of antioxidant, anti-inflammatory, and mucoadhesive lysine-carbonized nanogels. *Acta Biomater.* **141**, 140–150 (2022).

183. Jin, K. *et al.* Anti-oxidative and mucin-compensating dual-functional nano eye drops for

synergistic treatment of dry eye disease. *Appl. Mater. Today* **27**, 101411 (2022).

Appendices

Appendix A

Figure A1 presents a detailed schematic of the ozonolysis reaction of cholesteryl oleate and the products of the ozonolysis via the Criegee mechanism.
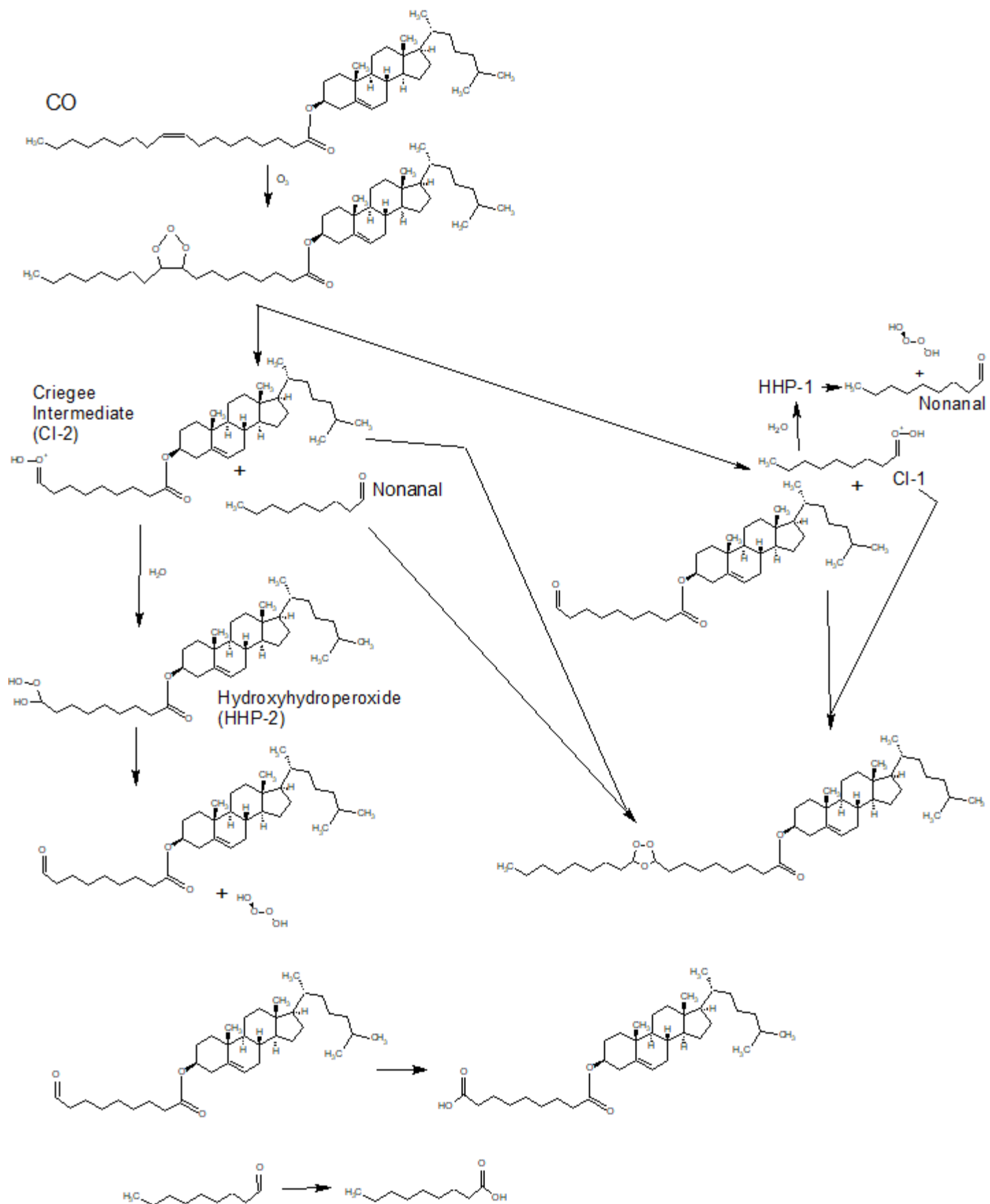
Figure A1. Ozonolysis of cholesteryl oleate (CO) via the Criegee mechanism (Detailed).
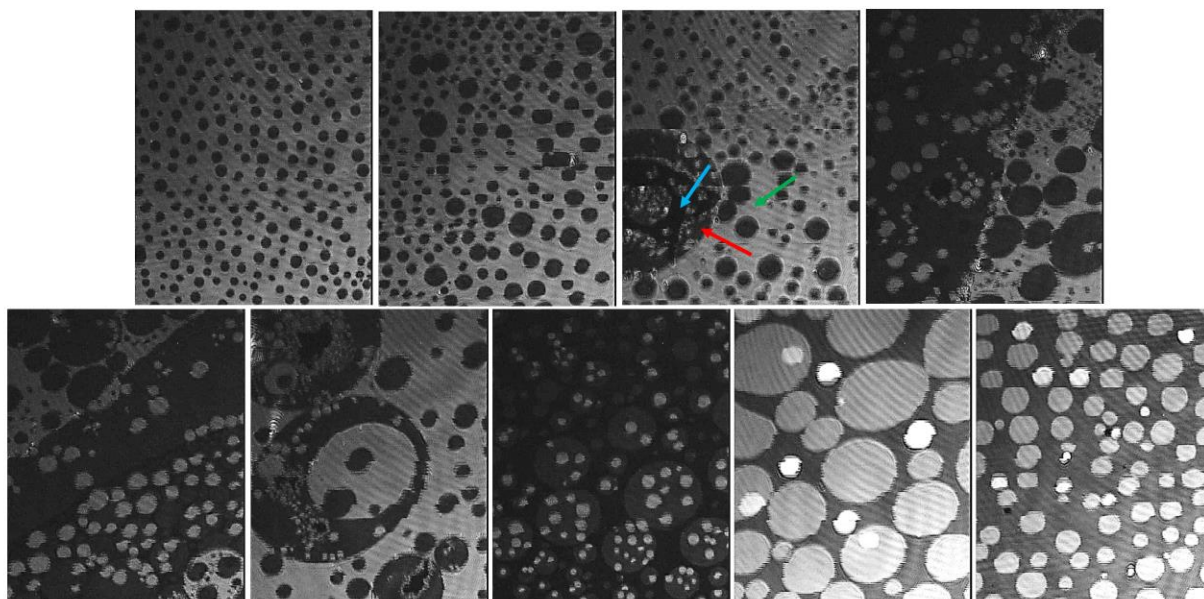
Figure A2. Contrast, brightness, and sharpness enhanced BAM images (220 μm wide) of cholesteryl oleate film at surface pressures (top, left to right): 2 mNm^{-1}, 5 mNm^{-1}, 7 mNm^{-1}, 9 mNm^{-1}, (bottom, left to right): 10 mNm^{-1}, 11 mNm^{-1}, 12 mNm^{-1}, 13 mNm^{-1} and 14 mNm^{-1} on PBS at 22 °C. The enhanced BAM image of CO film at the pressure of 7 mNm^{-1} shows three distinct phases, liquid expanded or gaseous phase (black area, blue arrow), intermediate phase (grey area, red arrow) and condensed phase (bright area, green arrow).
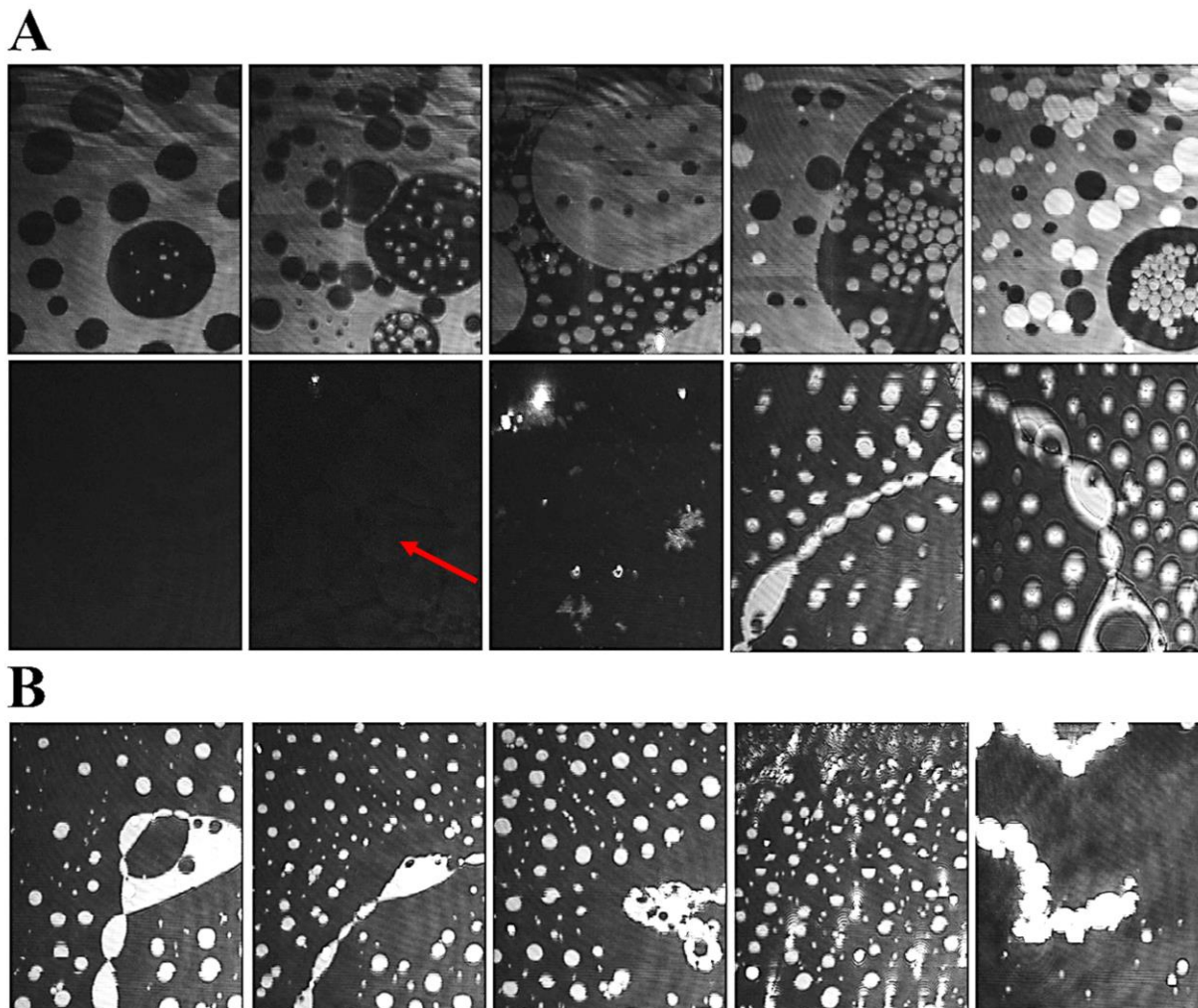
Figure A3. (A) Contrast, brightness and sharpness enhanced BAM images (220 μm wide) of CO:PC 90:10 (binary mixture) film at surface pressures (left to right): 2 mNm⁻¹, 5 mNm⁻¹, 7 mNm⁻¹, 13 mNm⁻¹ and , 14 mNm⁻¹ before ozone exposure (top) and after ozone exposure (bottom) on PBS at 22 °C. (B) BAM images (220 μm wide) of CO:PC 90:10 (binary mixture) film at surface pressures (left to right): 16 mNm⁻¹, 18 mNm⁻¹, 19 mNm⁻¹, 23 mNm⁻¹ after ozone exposure on PBS at 22 °C. The last BAM image to the right is of CO:PC 90:10 (binary mixture) film at surface pressure of 20 mNm⁻¹ after ozone exposure on PBS at 22 °C taken after the end of film compression. The enhanced BAM image of the film at the pressure of 5 mNm⁻¹ shows circular domains with low contrast (red arrow).
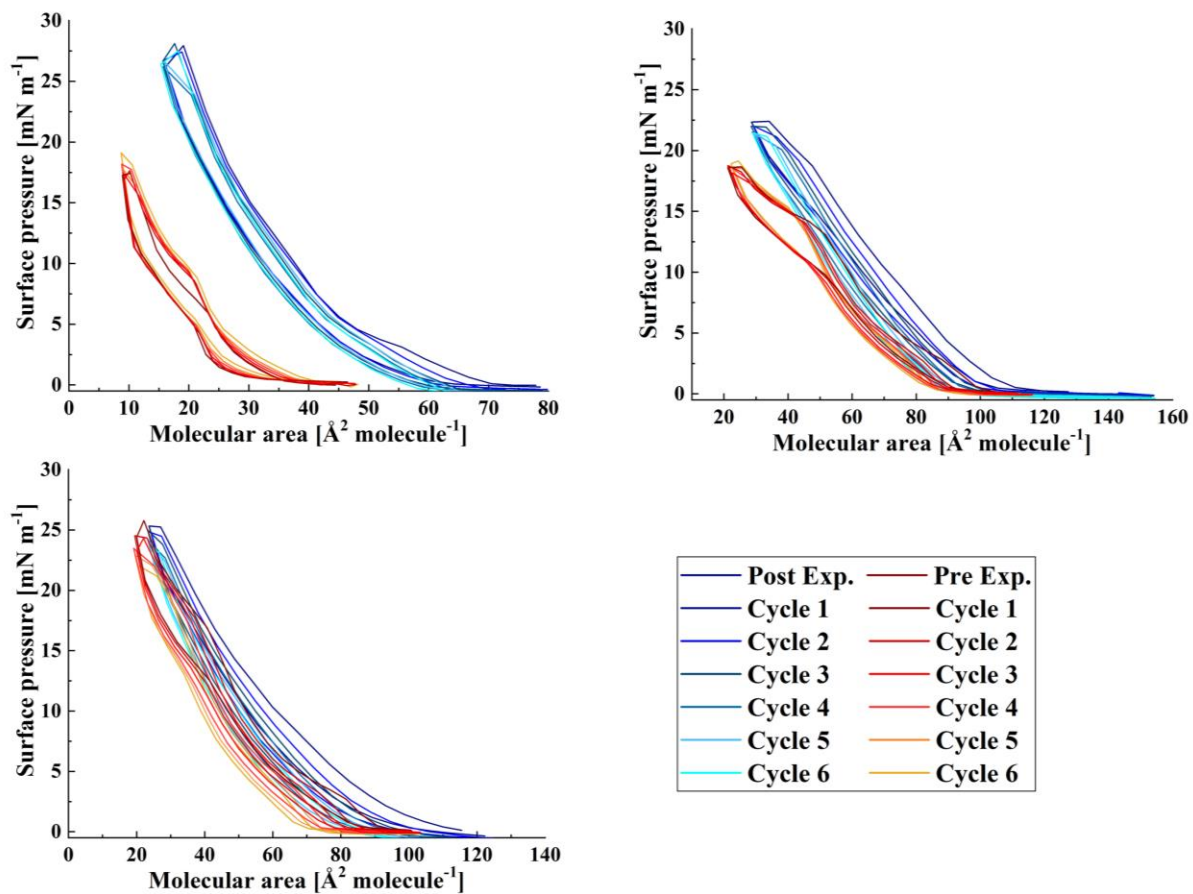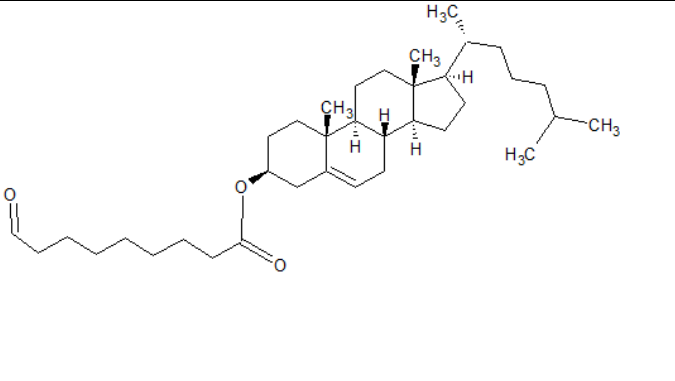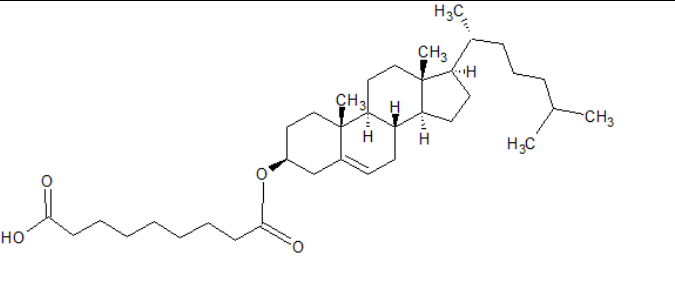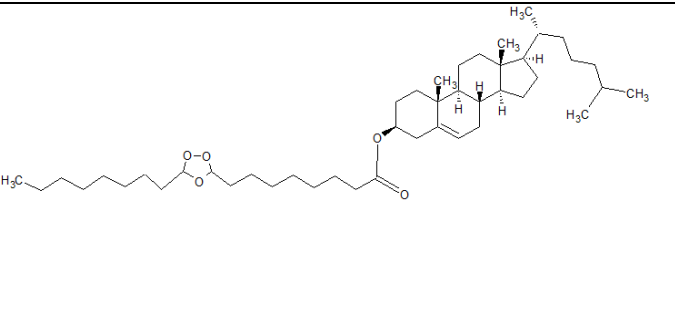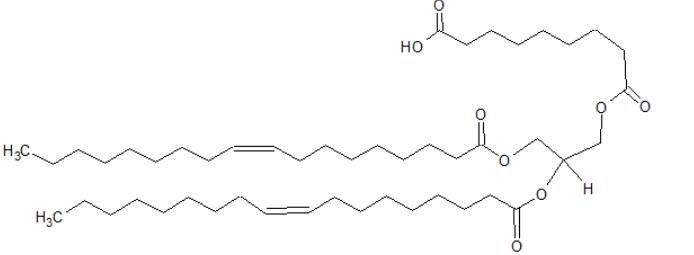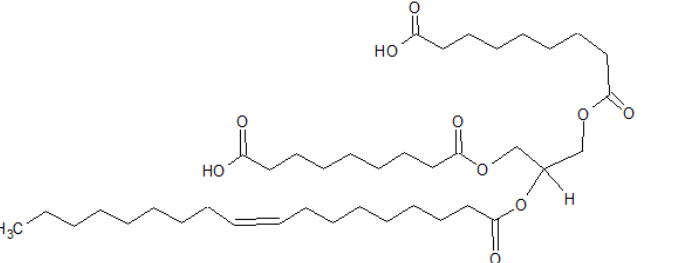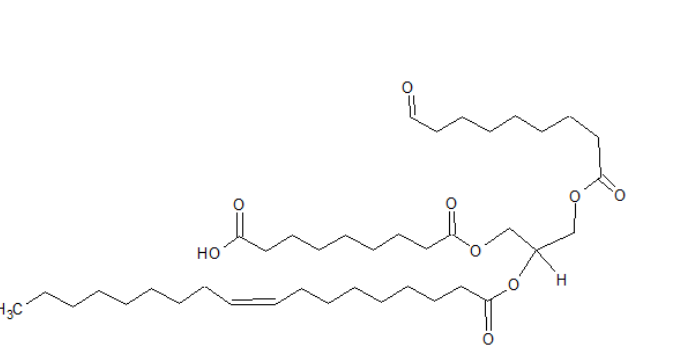
Figure A4. Compression-expansion cycles of CO:PC 90:10 (binary mixture, top, left), CO:GT:PC 40:40:20 (ternary mixture, top, right) and CO:GT:FFA:PC 40:25:15:20 (quaternary mixture, bottom) before ozone exposure (red color family) and after ozone exposure (blue color family) on PBS at 22 °C.
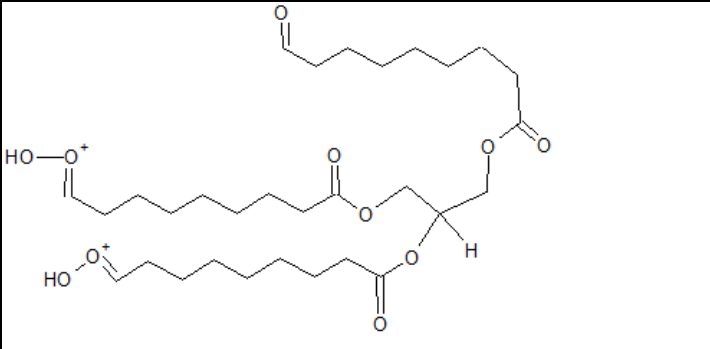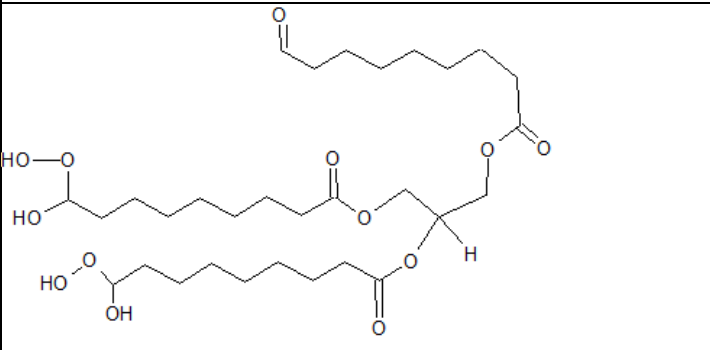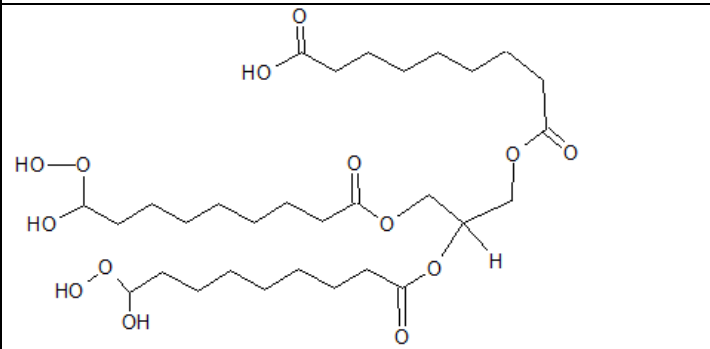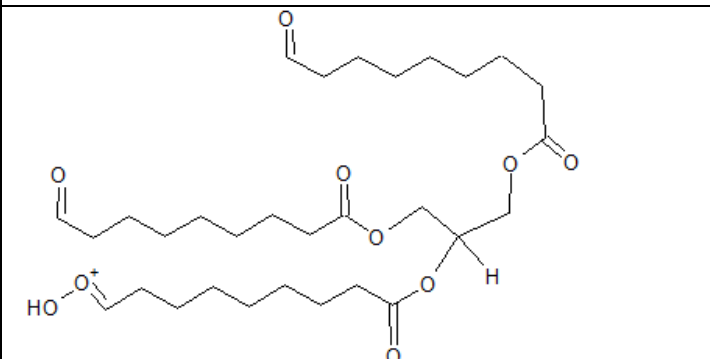
Table A1. ESI-MS data for oxidized cholesteryl oleate.

Structure	Theoretical m/z	Observed m/z	Mass Error (ppm)	Signal Intensity	Mode
	541.4615	541.4614	-0.0907	1.13E+05	Positive
	557.4564	557.4566	0.3606	8.94E+04	Positive
	699.5922	699.5957	5.0825	2.72E+06	Positive

Table A2. ESI-MS data for oxidized glyceryl trioleate.

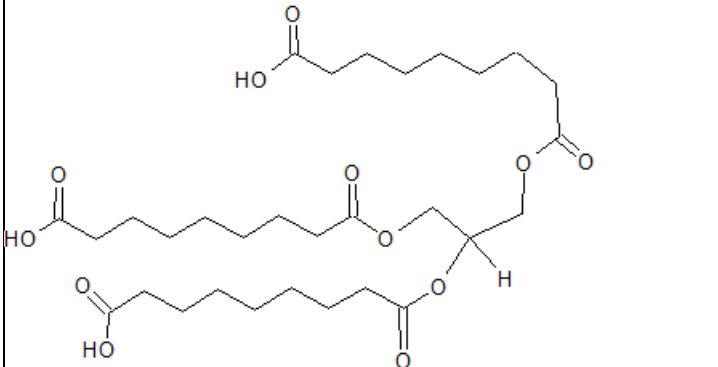| Structure	Theoretical m/z	Observed m/z	Mass Error (ppm)	Signal Intensity	Mode
	789.6249	789.6239	-1.3773	7.74E+03	Negative
	695.4739	695.4738	-0.1847	4.93E+03	Negative
	679.4790	679.4793	0.4644	1.18E+04	Negative

Structure	Theoretical m/z	Observed m/z	Mass Error (ppm)	Signal Intensity	Mode
	585.3280	585.3281	0.2577	1.28E+06	Negative
	621.3491	621.3412	-12.6749	1.44E+05	Negative
	637.3440	637.3483	6.6855	4.91E+03	Negative
	569.3331	569.3333	0.3751	1.37E+06	Negative
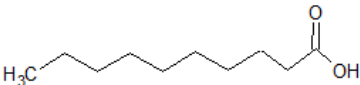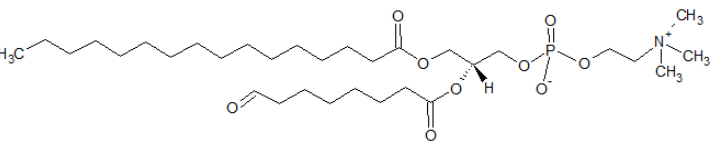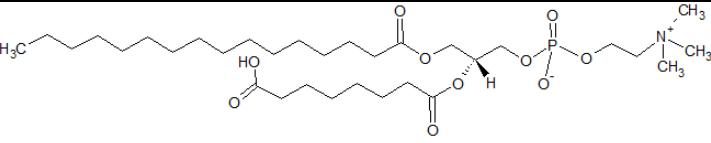
Structure	Theoretical m/z	Observed m/z	Mass Error (ppm)	Signal Intensity	Mode
	601.3229	601.3231	0.4067	1.38E+05	Negative

Table A3. ESI-MS data for oxidized egg PC.

Structure	Theoretical m/z	Observed m/z	Mass Error (ppm)	Signal Intensity	Mode
	171.1390	171.1393	1.5435	1.06E+06	Negative
	635.4167	635.4115	-8.2534	4.09E+03	Negative
	651.4116	651.4111	-0.8842	5.67E+03	Negative